UNIVERSITY OF NOVA GORICA
GRADUATE SCHOOL
STUDY PROGRAM: ENVIROMENTAL SCIENCES

# LIDAR SENSING OF AEROSOLS AND DETERMINATION OF THEIR TRAJECTORIES

Master thesis

**Maja Čolović-Daul**

Supervisor: prof.dr. Danilo Zavrtanik
Co-Supervisor: doc.dr. Klemen Bergant

Nova Gorica, 2007

## ACKNOWLEDGMENTS

I wish to express my sincere gratitude to Prof. Danilo Zavrtanik and Doc. Klemen Bergant, who guided this work and helped whenever I was in need. Their advice and patience is appreciated.
I am deeply indebted to Dr. Matej Horvat for his invaluable advice on data analysis software. Thanks to Doc. Darko Veberič, and Asst.Prof. Andrej Filipčič who greatly enriched my knowledge with exceptional insights into lidar work. Also, I want to thank to Dr. Biagio Forte for helping me with matlab work and cluster analysis.
Thanks to members of the commision: Prof. Jože Rakovec, Prof. William Eichinger and Asst.Prof. Marko Zavrtanik for their review and evaluation of the master thesis.
During the work on my thesis I had a pleasure to meet a lot of great scientists who became my friends. Azamela, Samo, Sophie, Petra, Mustafa, and all the rest, thank you for making my staying at University of Nova Gorica more enjoyable.
I would like to express my deepest gratitude for the constant support, understanding and love that I received from my mum, brother and twin sister.
My final, and most heartfelt, acknowledgment must go to my husband Haris, to whom I dedicate this thesis.

# POVZETEK

V delu je predstavljen študij troposferskih aerosolov nad jugozahodno Slovenijo. Rezultati temelje na devetih meritvah porazdelitve aerosolov, izvedene z UV LIDARskim sistemom ($\lambda =$ 355nm) na Otlici nad Ajdovščino med januarjem 2005 in septembrom 2006, ter na modeliranju gibanja zračnih mas s pomočjo modela HYSPLIT. Gibanje zračnih mas smo izračunali za šest različnih višin (1.5 km, 3 km, 4 km, 5.5 km, 7 km in 9 km) za 48-urne časovne intervale. Da bi lahko določili tipične smeri prihoda zračnih mas nad Slovenijo, smo njihove trajektorije porazdelili v skupine s sorodnimi poteki s pomočjo metode "K-means". Na ta način smo dobili štiri tipične razrede: severni (N), severozahodni-zahodni (NW-W), jugozahodni-zahodni (SW-W) in osrednji (C) razred. Razred C zajema zračne mase s kratkimi trajektorijami, za katere smeri prihoda nismo mogli eksaktno definirati. Analiza relativnih pogostosti trajektorij po razredih je pokazala, da večina zračnih mas nad Slovenijo pripada razredoma SW-W (47% do 30%, odvisno od višine) in C (35% do 25%). Razredoma N in NW-W pripada manjši delež trajektorij (vsakemu okoli 20%), ki se z višino skoraj ne spreminja. Izračun optičnih lastnosti atmosfere iz LIDARskih meritev povratnega sipanja temelji na Fernaldovi metodi. Ta privzema, da je mogoče razlikovati med sipanjem na molekulah atmosferskih plinov in sipanjem na aerosolih. Rezultati študija so vertikalne porazdelitve koeficientov za absorbcijo in za povratno sipanje na aerosolih ($\alpha_a$ in $\beta_a$), optična debelina atmosfere ($\tau$), in LIDARsko razmerje ($R$). Največje vrednosti sipalnih in absorpcijskih koeficientov, $\beta_a = (3.0 \pm 0.4)\, 10^{-6}\mathrm{m}^{-1}\,\mathrm{sr}^{-1}$, $\alpha_a = (3.0 \pm 0.3) 10^{-5}\mathrm{m}^{-1}$, smo izmerili v primeru zračnih mas iz razreda SW-W. LIDARsko razmerje je bilo 35 in optična debelina $\tau$ do višine 15 km je bila okoli 0.8. Analiza gibanja zračnih mas je kazala na možnost prisotnosti saharskega peska. Za zračne mase iz severozahoda (razred NW) smo izmerili $\beta_a = (1.0 \pm 0.3)\, 10^{-6}\mathrm{m}^{-1}\,\mathrm{sr}^{-1}$, $\alpha_a = (1.0 \pm 0.3)\, 10^{-5}\mathrm{m}^{-1}$, LIDARsko razmerje $R = 15$ in optično debelino $\tau$ do višine 15 km okoli 0.6. Analiza gibanja zračnih mas je v tem primeru kazala na možnost prisotnosti aerosolov morskega tipa. Za zračne mase, ki prihajajo s severa (razred N) zaenkrat še nimamo meritev, za zračne mase, ki so razvrščene v razred C pa prevladujočega tipa aerosolov ni bilo mogoče določiti. Iz študije lahko zaključimo, da z obstoječim LIDARskim sistemom lahko zaznamo tako aerosole morskega kot peščenega tipa, in da med njimi lahko razlikujemo. V primerjavi z aerosoli peščenega tipa so imeli aerosoli morskega tipa približno trikrat nižje vrednosti koeficientov $\alpha_a$, $\beta_a$ in za četrtino nižje vrednosti optične debeline.

# ABSTRACT

The LIDAR case studies are presented in conjunction with the air mass back-trajectory analysis to better characterize the vertical structure of the LIDAR sensed tropospheric aerosols. In this analysis, the UV light of 355 nm is used. Air trajectories for the period of January 2005 - September 2006 are computed using the HYSPLIT model. In order to determine typical airflow directions of air arriving to Slovenia, grouping of trajectories with similar history paths was performed using the K-means method. Air trajectories are determined for 6 different heights (1.5 km, 3 km, 4 km, 5.5 km, 7 km and 9 km) for 48 hour long time intervals. Clustering of air trajectories resulted in recognition of four typical classes: Northern class (N), Northwest-Western class (NW-W), Southwest-Western class (SW-W) and Central class (C). The class C gathers the short trajectories arriving from different directions. Analysis of the relative frequencies of overall trajectories assigned to different classes showed that most of the air trajectories represent the SW-W (from 47% to 30% for different altitudes) and C (35% to 25%) classes. Classes N and NW-W are characterized by lower relative frequencies that are similar for all heights (for both classes of about 20%). Estimation of atmospheric optical properties in the UV, related to aerosols, were performed using the Fernald method for analysis of LIDAR data obtained at Otlica observatory. The findings are presented in terms of the vertical profiles of the aerosol extinction and back-scattering coefficients, $\alpha_a$ and $\beta_a$, respectively, optical depth, $\tau$, and LIDAR ratio. The highest aerosol back-scattering and extinction coefficient values, $\beta_a = (3.0 \pm 0.4)\,10^{-6}\mathrm{m}^{-1}\,\mathrm{sr}^{-1}$ and $\alpha_a = (3.0 \pm 0.3)10^{-5}\mathrm{m}^{-1}$, were measured in the case when air masses were arriving from SW-W direction. The LIDAR ratio was estimated to be 35 and up to a height of 15 km the cumulative value of an optical depth was of about $\tau = 0.8$. LIDAR analysis and air mass history indicated that in this cases Saharan dust was present in the atmosphere. For the air arriving from Northwestern direction, back-scattering and extinction coefficients had values of $\beta_a = (1.0 \pm 0.3)\,10^{-6}\mathrm{m}^{-1}\,\mathrm{sr}^{-1}$ and $\alpha_a = (1.0 \pm 0.3)\,10^{-5}\mathrm{m}^{-1}$. The cumulative value of an optical depth that in these cases reached a value of about 0.6 up to 15 km and estimated LIDAR ratio was 15. LIDAR analysis and air mass history indicated presence of maritime aerosols in atmosphere. The presented LIDAR data did not contain any representative of the class N. When the air was brought by slow and weak winds characteristic for class C, a prevailing type of aerosols was not possible to specify. With present LIDAR system Saharan dust and maritime aerosols can be identified. When the Saharan dust was present in atmosphere, $\alpha_a$ and $\beta_a$ had approximately three times higher values, as well as of about one quarter higher values of $\tau$, than in the case of maritime aerosols.

# Contents

# List of Figures

# List of Tables

# 1 Introduction

The temperature, humidity and wind soundings are crucial in atmospheric research. **LI**ght **D**etection **A**nd **R**anging (**LIDAR**) and **RA**dio **D**etection **A**nd **R**anging (**RADAR**) are the backbone of the fields dealing with the retrieval of vertical profiles of different atmospheric components and estimation of ground precipitation.

The LIDAR principle dates back to pre-laser times. Attempts to measure air density profiles using the scattering intensity from searchlight beams were made in 1930. In 1938, pulses of light were used to measure cloud base heights [1]. The term LIDAR was used for the first time in the year 1953 without specifying the meaning of its abbreviation [2]. The acronym is used when a generation of light pulses by electric sparks and flash-lamps allows for the replacement of the bistatic configuration by monostatic setup [1].

Modern LIDAR technology developed rapidly with introduction of the laser in 1960. Ever since that time, the development of LIDAR has been strongly connected with the progress in optical and electronics technology [3]. The LIDAR makes it possible to observe the atmosphere without interfering with the processes occurring in the air. In addition, good temporal and spatial resolution makes LIDAR highly suitable for atmospheric research [1]. LIDAR is particularly useful for retrieval of highly variable atmospheric parameters that are dependent on the air structure. The discovery of the ozone hole and global warming, as well as other climate change phenomena caused by greenhouse gases and increased concentration of aerosols in the atmosphere, moved LIDAR research of the atmosphere in a new direction [1, 3, 4]. To strengthen research capabilities, LIDAR stations from several European countries were organized in a LIDAR network called EARLINET [5, 6].

Aerosols influence the energy balance of the Earth's surface, the water cycle and atmospheric chemistry [2]. Together with greenhouse gases they play a crucial role in climate change [7]. Aerosol particles act as absorbers and scatterers of shortwave solar radiation and long wave terrestrial radiation. At the same time, they act as condensation nuclei that cause the formation of clouds and precipitation, influencing surface radiation balance [8]. By increasing the albedo of the Earth's surface for solar radiation, aerosols have a cooling effect on the atmosphere. On the other hand, absorbing long wave terrestrial radiation, the aerosols contribute to the warming of the atmosphere. Study of the vertical distribution and properties of aerosols is an important issue due to their complex role in the radiation balance of the Earth's surface and consequently climate variability [7].

Retrieval of aerosol attendance is turning out to be one of the most interesting LIDAR applications. Raman or elastic Mie and/or Rayleigh LIDAR [9–14] are usually used. With LIDAR, aerosol absorption and back-scattering coefficients are retrieved, as well as aerosol type and size distribution.

While the presence of aerosols in the atmosphere depends on air mass history, the properties of the aerosols depend on their origin. Hence, the retrieval of particle paths can give addi-

tional insight into aerosol characteristics and types [15–18]. In many cases it is possible to attribute the observed aerosols to their origins. Moreover, since aerosols cause the formation of rain, determination of precipitation chemistry patterns and deposition are commonly studied [19–21].
Slovenia is located at the crossroad of the Mediterranean, continental and Alpine climate regions. Exchanges of maritime and continental as well as polar and tropical air masses, are common. Moreover, tropical winds from the Sahara desert bring dust particles with them. This results in deposition of dust aerosols as well as cloud and rain formation over Slovenia. The LIDAR system at Otlica was built to study the tropospheric aerosol paths and light attenuation profiles [22]. To understand aerosols more qualitatively, the air mass origins and path history are studied.
Motivated by the significant aerosol influence on atmospheric optical properties and air quality this thesis has the following goals:

- to establish LIDAR measurements of optical properties of the atmosphere in relation to the vertical distribution of aerosols,
- to investigate the potential relationship between aerosol origin and its influence on the optical properties of the atmosphere,
- to use LIDAR for monitoring of air pollution over the region of Trnovski gozd and to investigate the potential of LIDAR at Otlica to track the transport of aerosols on a large scale.

This thesis is organized in the following way:

- Chapter 2 describes the atmospheric layers, the interactions between light and air constituents, as well as typical air masses that reach Europe region.
- Chapter 3 gives a description of LIDAR hardware and data acquisition software. Also described are methods used to analyze atmospheric optical properties as well as methods used to determine classes of typical air masses.
- Chapter 4 presents results of a trajectory analysis, and a LIDAR case study evaluating the influence of aerosols on optical properties of the atmosphere based on the particle origin.
- Conclusions are outlined in Chapter 5.
- Appendix and references are presented at the end of the thesis.

# 2 Atmosphere and aerosols

Aerosols are tiny liquid and solid particles suspended in the air. They occur both naturally and as an result of human activities. Being a part of the atmosphere, they influence its optical properties via aerosol-light interactions. Quantitative description of the aerosol presence can be obtained using the LIDAR systems. Since properties of detected aerosols depend on the origins of air masses, determination of air mass history can provide information about aerosol types. The basic information on the atmosphere and interaction processes between radiation and air constituents, as well as typical air masses that reach Europe are presented in following chapter.

## 2.1 Structure of the atmosphere

The major constituents of the atmosphere are nitrogen (78%), oxygen (20%), argon (0.9%) and different trace gases. Particles that are products of human activity (e.g. industry) or nature (e.g. volcano) are also present. Aerosols and molecules are spread according to the structure of the atmosphere and weather conditions.
Because of the gravity, the atmospheric density and pressure are highest near the Earth's surface and decrease exponentially with altitude. Hence, the upper boundary of the atmosphere cannot be precisely determined. About 80% of the total air mass is concentrated up to 11 km, and 99% of total mass is distributed up to 30 km [24].

Based upon the hydrostatic stability, which depends on distribution of temperature with height, the Earth's atmosphere is divided in layers. Different atmospheric layers are presented in Figure 2.1. In the lowest layer, called the troposphere and extends up to about 15 km. The temperature here decreases with height, creating conditions for hydrostatic instability. This is the main reason for vertical movement of air and the weather changes in the troposphere. The lower part of the troposphere, up to about 1.5 km, is highly influenced by the Earth's topography. The tropopause is a boundary layer between the troposphere and the stratosphere, where an abrupt change (decrease) in temperature lapse rate usually occurs.
The stratosphere follows the troposphere and extends up to 50 kilometers. Compared to the troposphere, this part of the atmosphere is drier and less dense. The temperature increases gradually to $-3$ degrees Celsius due to the absorption of ultraviolet radiation. Because of this, the main characteristic of stratosphere is dynamic stability. Phase changes of water are not present and the stratosphere does not contain clouds as does the troposphere. Ozonosphere spreads almost through the entire stratosphere. Most of the ozone is concentrated at about 20 km to 25 km. Ozone absorbs and scatters the solar ultraviolet radiation. The stratopause is a section where a maximum in the stratospheric temperature occurs. It is the level of the atmosphere which is the boundary between stratosphere and mesosphere.
The mesosphere is above the stratopause and extends to 85 kilometers. The temperature

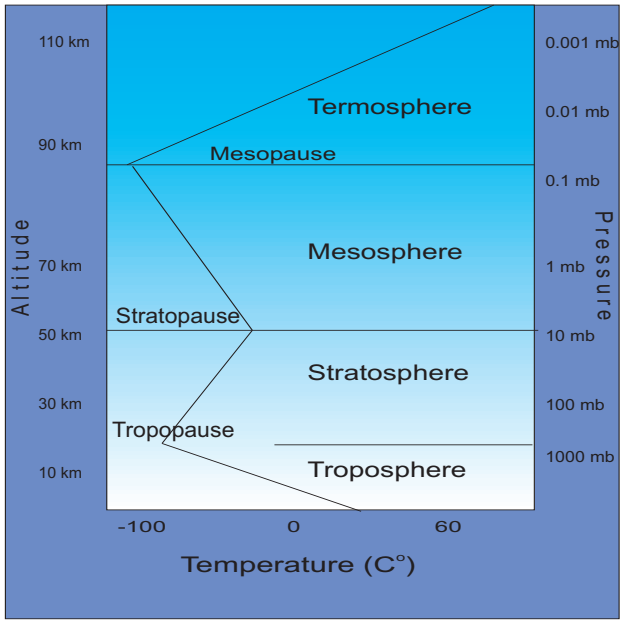


**Figure 2.1:** Schematic view of the Earth's atmosphere.

decreases to −93 degrees Celsius with increase in altitude. The mesopause is the level that separates the mesosphere and termosphere. It is characterized by a pronounced minimum in the temperature profile.
The thermosphere starts just above the mesopause and extends to 600 kilometers. In the termosphere, the ions absorb sunlight causing the temperature to increase with altitude.
While passing the atmospheric layers radiation becomes attenuated. To understand the processes that cause this attenuation, interactions between radiation and atmospheric particles need to be studied.

## 2.2 Propagation of radiation through the atmosphere

Visibility degradation results from radiation scattering and absorption by atmospheric particles and gases. Figure 2.2 illustrates absorption and scattering processes. Scattering is a process in which a photon is absorbed by a particle and re-radiated after a very short time [25]. Particles can scatter light elastically and inelastically.
In elastic scattering [1] the particles diffuse a portion of the incident radiation in all directions [26]. The wavelength of the radiation after elastic scattering does not change. There are three different types of elastic scattering in atmosphere: Rayleigh scattering, Mie scattering and non-selective scattering. Non-selective scattering occurs in the troposhere, where the radius of the particles is much larger than the incident radiation wavelength. An example of non-selective scattering is the scattering of sunlight by atmospheric constituents such as large aerosols, cloud droplets or ice crystals. Rayleigh and Mie scattering are used to explain processes such as blue sky, haze, white clouds [27].
Photons can be scattered equally in all directions (isotropic scattering). In most instances

[1] Elastic scattering occurs through three processes: (1) diffraction, (2) refraction and (3) phase shift.

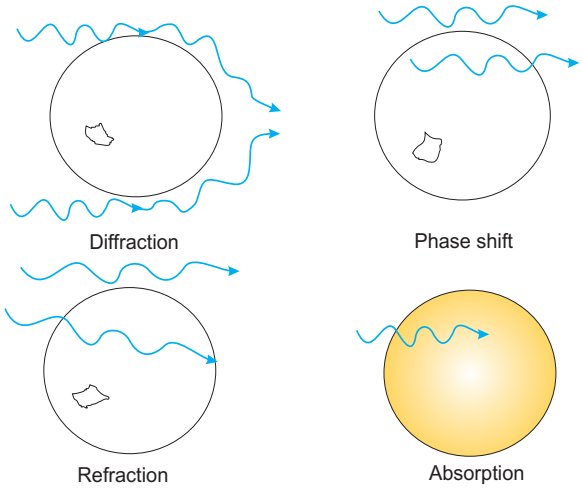


**Figure 2.2:** Physical processes between light and particles: diffraction, phase shift, refraction and absorption [26].

photons are scattered by aerosols in a forward direction [1]. For large particles nearly 100% of the incident photons end up being scattered in the forward direction due to light diffraction [2] [1]. If the particles are small in comparison to the wavelength of a photon (such as the air molecules) the amount of light scattered in the forward and backward directions is nearly the same. As the particle increases in size, more light tends to scatter in the forward direction. Figure 2.3 shows the distribution of scattered light for different particle sizes compared to the wavelength of the light [25].

Rayleigh scattering occurs when the particles are smaller in size than the wavelength of the light interacting with them. This kind of scattering is wavelength dependent. As the wavelength decreases, the fraction of scattered light increases. The intensity $I$ of the light scattered by a single small particle is given by

$$I = I_0 \frac{1 + cos^2\theta}{2r^2} \left[\frac{2\pi}{\lambda}\right]^2 \left[\frac{n^2 - 1}{n^2 + 2}\right]^2 \left[\frac{d}{2}\right]^6 . \tag{2.1}$$

where $\lambda$ is the wavelength and $I_0$ is the intensity of the beam light. The $r$ is the distance to the particle, $\theta$ is the scattering angle, $n$ is the refractive index of the particle and $d$ is the diameter of the particle. The angular distribution of Rayleigh scattering, governed by the $(1 + cos^2\theta)$ term, is symmetric in the plane normal to the incident direction of the light. Due to this, the forward scattering equals the backward scattering. Integration over the sphere surrounding the particle gives the Rayleigh scattering cross section $\sigma_R$:

$$\sigma_R = \frac{2\,\pi^5}{3} \frac{d^6}{\lambda^4} \left[\frac{n^2 - 1}{n^2 + 2}\right]^2 \tag{2.2}$$

The scattering cross section, through which sunlight is scattered, by molecules of the atmosphere's constituent gases, varies inversely as the fourth power of the wavelength. Blue light belonging to the near end of the short wavelength range of the visible spectrum is scattered

[2] Diffraction is the slight bending of light as it passes around the edge of an object.

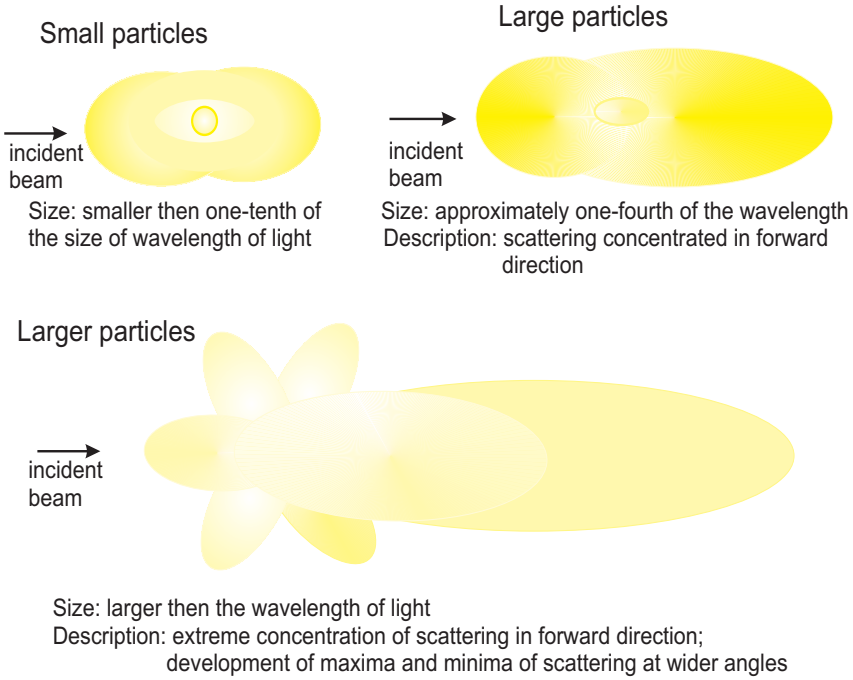


**Figure 2.3:** Scattering of light as a function of particle size. The isotropic scattering by small particles and forward scattering by large particles is illustrated [25].

much more strongly than the long wavelength of red light. This results in the blue color of the sky. The Rayleigh law also predicts the variation of the intensity of scattered light with direction. One of the results is that there is complete symmetry in the patterns of forward and backward scattering from single particles [28].

As the characteristic size of the particles approaches the size of the wavelength of the incident light, the Rayleigh scattering changes to Mie scattering. Fog, haze, and aerosol particles are the major contributors to this process in the region of near infrared, visible, and UV wavelength. Mie scattering is visualized as an interaction between waves that wrap themselves around and through the particle. Light scattering is caused by all atmospheric particles. Photons scatter most effectively when the diameter of the particle is of the same size as the wavelength.

The simplest way to describe Mie scattering is when the scattering volume under consideration is assumed to be filled uniformly by particles of the same size and composition [25]. Each of these particles has the same index of refraction and thus the same scattering properties. Similar to molecular scattering, integrating the scattered light emitted over all directions, we obtain the total particle scattering coefficient, is written as [4]:

$$\beta_p = N_p \, \sigma_p \tag{2.3}$$

where $N_p$ is the particle number density and $\sigma_p$ is the single particle cross section.

Additional dimensionless parameters are defined to better describe Mie scattering theory. The first is the scattering efficiency $Q_{sc}$, defined as the ratio of particle scattering cross section $\sigma_p$ to the geometric cross-sectional area of the scattering particle [4]:

$$Q_{sc} = \frac{\sigma_p}{\pi\, 4\, d^2} \tag{2.4}$$

where the $d$ is the particle diameter.
The second parameter is the size parameter $\phi$, defined as:

$$\phi = \frac{2\,\pi\, d}{\lambda} \tag{2.5}$$

where $\lambda$ is the light wavelength [4]. As follows from equation 2.3, the total particle scattering coefficient is written as:

$$\beta_p = N_p\, \pi\, d^2\, Q_{sc} \tag{2.6}$$

Particle scattering is separated into three specific types depending on the size parameter. The first type, where $\phi << 1$, characterizes scattering by small particles, such as those in a clear atmosphere. This type of scattering is similar to Rayleigh scattering. The region where $\phi > 40$ characterizes scattering by large particles. These particles are like those formed in heavy fog and clouds. For these values of the scattering does not depend on the wavelength of the incoming light. The intermediate type ($1 < \phi < 25$) characterizes scattering by by particles of sizes that are commonly found in the lower parts of the atmosphere [4]. Figure

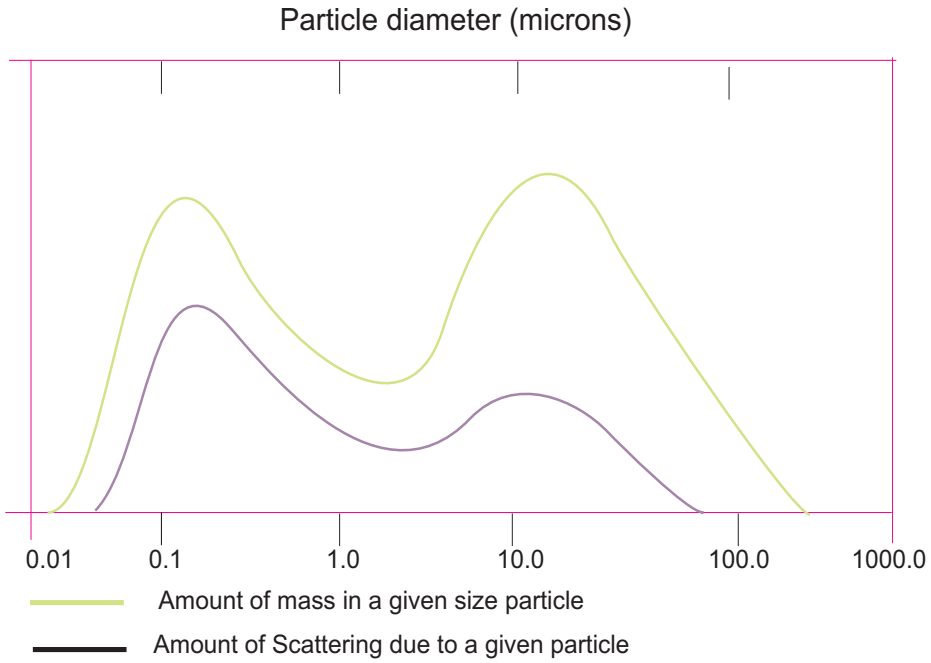


**Figure 2.4:** Mass particle size distribution compared to the relative amount of light scattered, depending on the size of particles [28].

2.4 shows the relative amount of scattering compared to the size of particles. The green line represents typical mass size distribution of the particles. The violet line shows amount of scattering due to size of a given particle. Particles less than 2.5 microns are referred to as "fine particles" and particles larger than 2.5 microns are called "coarse particles" [4]. From a figure, the total mass of the smaller particles is less than the total mass of larger particles. Nevertheless, the amount of scattering is larger for particles of smaller sizes since fine particles are more efficient at scattering light.

## 2.3 LIDAR sensing of aerosols

The LIDAR, with its high spatial and temporal resolutions, is used to remotely probe the atmosphere. It observes the attenuation of radiation appearing due to interaction of light with gas molecules and aerosols suspended in the air.
A typical mono-static LIDAR has a laser and a receiver at the same place as shown in Figure 2.5. A pulsed laser is used as a source of light directed at a certain elevation angle towards the atmosphere. A small fraction of light is scattered back in the direction of the LIDAR system. The back-scattered light is collected by a reflective or refractive receiving optics and transferred to a photo-detector. The photo-detector operates in the proportional regime,

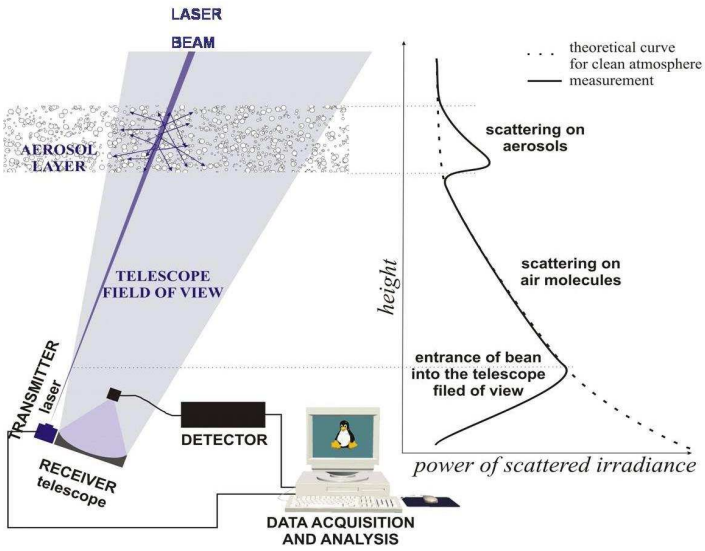


**Figure 2.5:** The major parts of LIDAR detection system. Note the characteristic signal response representing scattering from air constituents [29].

so that the resulting magnitude of electrical signals corresponds to the number of photon received. A digitizer transforms analog signals from the photo-detector into digital ones, which are more suitable for data storage and computer-based analysis. A typical analog signal is shown also in Figure 2.5. Note the pronounced peak in the distribution caused by scattering from aerosols.

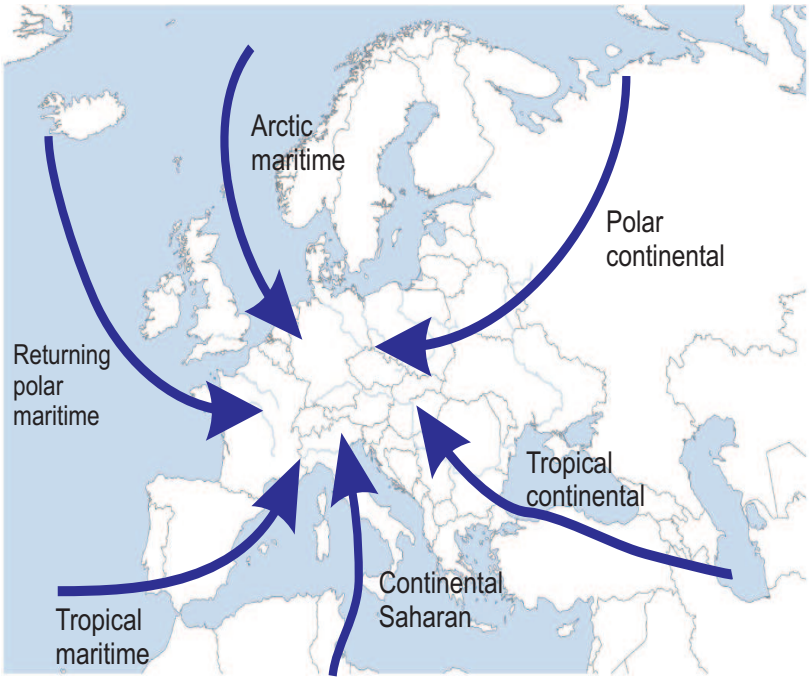


**Figure 2.6:** Sources of air masses that reach the middle Europe [30].

The range of the scattering volume producing the signal can be determined from the time interval between transmission and detection time. The magnitude of the received signal is governed by the back-scattering properties of the atmosphere and by the two-way atmospheric attenuation. Back-scattering in turn depends upon the wavelength of the laser energy used. It also depends on the number, size, shape and refractive properties of the particles or droplets intercepting the incident energy. The electrical signal from the photo-detector thus contains information on the presence, location, and relative concentration of atmospheric scatterers and absorbers, which can be extracted by computer-based analysis of the data.

## 2.4 Aerosol transport modeling

In principle, the LIDAR measurements are used to determine vertical distributions of aerosols, their types, sizes and concentrations. This kind of information can be used as a new input in air history modeling.

Air masses form and pass over different geographic regions collecting particles emitted from the ground (anthropogenic and natural). Thus, the properties of air masses strongly depend on their history. Some of the particles are deposited close to their sources, while others are spread by air flow all around the globe. The range of transport depends on weather conditions and typical atmospheric circulation patterns. Hence, it is important to know how the aerosols affect the atmospheric optical properties with regards to their origin. This information can be obtained from the LIDA and used as input to different aerosol transport models to enhance their predictions.

On the other hand, history of air masses can be used to in conjunction with LIDAR measurement to better characterize vertical structure and temporal evolution of aerosol layers.

Typical air masses that reach Europe develop over Northern and North-Western part of the Atlantic Ocean, Russia, Siberia, Asia minor, the Mediterranean sea, and the Sahara desert. As shown in Figure 2.6, air masses are divided according to temperature (polar and tropical) and humidity (maritime and continental) [30]. A way to distinguish between different directions of airflow is to analyze air trajectories by using different computational models. Air trajectories are defined as the paths of infinitesimally small particles of air [31]. Forward trajectories describe where particles will go, backward trajectories where that are coming from. For many years, trajectories have frequently been used for interpretation of individual flow situations. However, statistical methods to cluster large sets of trajectories have been developed recently [32]. To indicate typical air flows, trajectories are usually grouped into classes representing trajectories with similar properties. Clusters would indicate groups of trajectories of simmilar histories, providing information about air mass origins, directions of flow and types of aerosol that they carry.

# 3 Experimental setup and analysis methods

The University of Nova Gorica has established a LIDAR facility, located at Otlica near Ajdovščina, where optical remote sensing of tropospheric aerosols is carried out. The software for hardware utilization of the LIDAR system at Otlica was developed in 2003 and 2004. The research work in this thesis included LIDAR set up and testing, as well as the development of the software for data analysis.
Detection of aerosols is performed under different meteorological conditions. The aerosol paths governed by the air mass history were inferred by means of numerical modeling. The following chapter presents a description of the LIDAR system, providing information about hardware and software details. The method used to analyze LIDAR data, as well as models and methods applied in order to determine air paths and typical air flows, are also described.

## 3.1 LIDAR at Otlica observatory

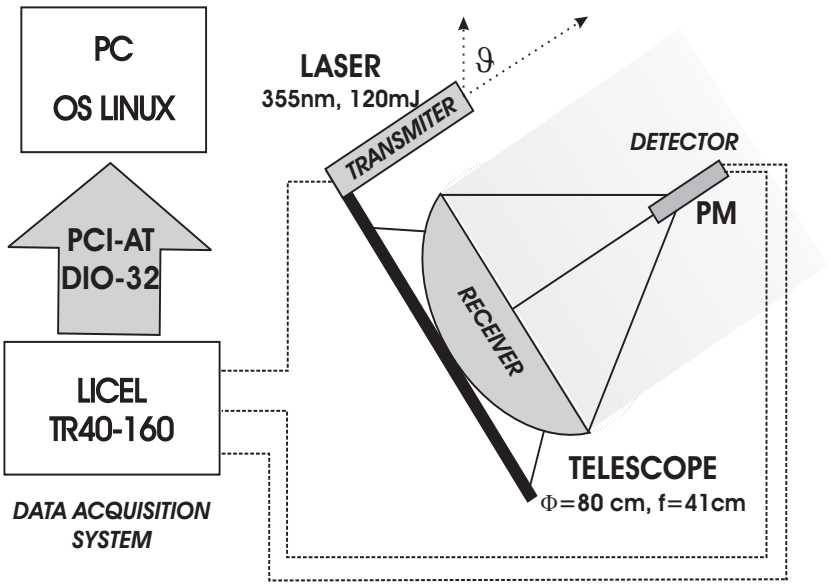


**Figure 3.1:** Schematic view of LIDAR system build at Otlica, Slovenia. It is composed of a laser, receiving mirror, light detector, data acquisition system and computer.

Otlica is located in Slovenian upland, positioned at around 1000 m above sea level. Below

Otlica, the Vipava valley is situated at 100 m above the sea level. Otlica belongs to the region of Trnovski gozd. This region represents the first topographic barrier reached by air masses approaching from Southwest. These masses usually bring warm and humid air. Due to this, an extensive dry and wet deposition of aerosols is commonly present.
The goal of LIDAR measurements was to provide information about air pollution across the areas of Trnovski gozd, Vipava valley, Kras and the Slovenian coastal area. With the present LIDAR setup, Otlica observatory provides information about aerosols vertically up to an altitude of about 40 kilometers. Meteorological models are used simultaneously for the estimation of the aerosol transport history.
Future LIDAR measurements, together with meteorological models, will provide information on the level of the pollution of the air masses reaching Slovenia, and on their origin.

### 3.1.1 System and equipment

**Figure 3.2:** LIDAR system: LIDAR sliding on rails from inside the shelter (left); vertical and horizontal LIDAR positions (right top and bottom).

The LIDAR is setup according to the scheme in Figure 3.1. The system is mounted on a metal frame, which is installed on rails for easier storage and outdoor operation (Figure 3.2). It contains one transmitter and three detector modules, of which only one is being used in the current setup. The transmitter is a laser that emits pulses of UV light in the atmosphere. The back-scattered light is collected by the LIDAR's receiver. The receiver is a parabolic mirror that focuses the collected light into a photo-sensitive detector. Detection and transformation of the received light into a measurable electrical signal is achieved using a photomultiplier. Digitization of the signal is performed by an analog/digital converter that is connected to the computer responsible for data acquisition and analysis.
Up to now, only vertical measurements at $90^o$ degrees elevation have been possible. A mechanism for changing the tilt angle is in preparation and measurements at different elevations will be made in the future. However, due to the topology of the surrounding terrain, horizontal

scans of the sky at different azimuths will not be possible.

### Laser

The Nd:YAG Quantel Brilliant B pulsed laser [33] is used as an emitter (Figure 3.3).

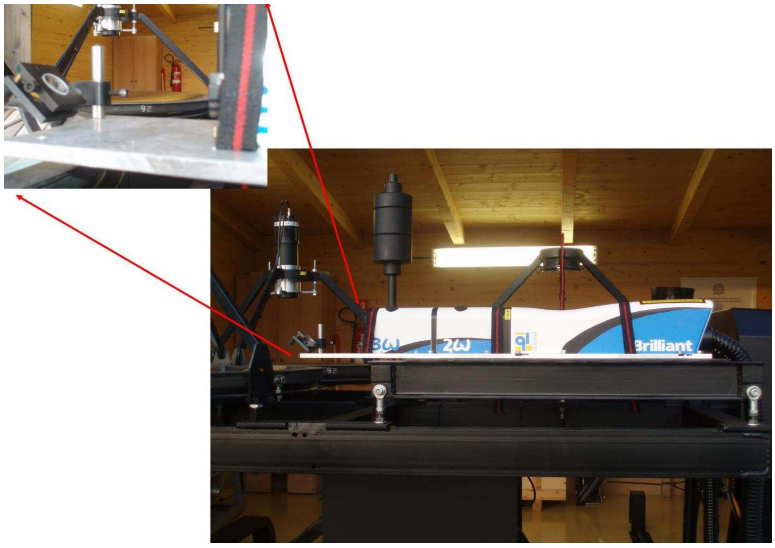


**Figure 3.3:** The Nd:YAG Quantel Brilliant B pulsed laser. Light from the laser is directed $90^o$ with respect to the laser orientation via a small mirror.

**Figure 3.4:** Receiver and detector of the LIDAR system at Otlica: the parabolic mirror and photomultiplier. The PMT is placed on the focal point of the mirror.

**Nd:YAG** is an acronym for **N**eo**d**ymium-doped **Y**ttrium **A**luminum **G**arnet, a compound that is used as the light emitting material in the solid state lasers. To obtain the desired

**Table 3.1:** Main characteristics of Hamamatsu PMT R7400U-06 detector.

| **PMT Characteristics** | **R7400U-06** |
|---|---|
| Effective photo cathode diameter (mm) | $12.8 \pm 0.5$ |
| Spectral response range (nm) | $160 - 650$ |
| Rise time (ns) | 0.78 |
| Transit time (ns) | 5.4 |
| Gain | $7 \cdot 10^5$ |
| Anode to cathode supply voltage (V dc) | 800 |

frequency, the laser light was frequency tripled to a wavelength of 355 nm. Maximum energy per pulse is 120 mJ with a pulse duration of 5 ns. The divergence of the emitted light beam is 0.55 mrad and the laser is parallel to the plane of the mirror. The emitted beam is reflected at a $90^o$ angle with respect to laser orientation by a small adjustable mirror (Figure 3.3).

### Receiver

Back-scattered light is collected by a parabolic mirror mounted on the metal frame. The mirror has a diameter of 80 cm and a focal distance of 41 cm. The mirror is coated with a thin aluminum layer to increase reflectivity. Figure 3.4. shows the mirror. At the moment, alignment of the laser beam and telescopes field of view, is performed manually using the oscilloscope and steering the mirror by hand. Since, this can introduce uncertainties in measurements it is planned to upgrade the system with a steering motor that would be operated remotely from computer. By steering the mirror for some deegrees in vertical and horizontal direction three dimensional picture about the alingement of laser beam and receivers field of view can be obtained. Determining the vertical and horizontal positions of mirror of the maximum signal obtained, optimum position of directing mirror giving the best alingement can be determined.

### Detector and filters

A **P**hoto**M**ultiplier **T**ube(**PMT**) a Hamamatsu photomultiplier R7400U-06 [34] is used as a detector. It is placed at the focal point of the receiving mirror (Figure 3.4). Main characteristics of this detector are listed in Table 3.1. PMTs have a high gain making them suitable detectors for LIDAR systems.

To avoid large portion of UV light from a Sun, which acts as a background in our measurement, tThe optical filters are placed in front of the PMT. The filter used in our case is the Schott Glass UG-1 filter. It transmits laser light in the UV range band from 300 nm to 400 nm and has its maximal transmittance at 355nm (Figure 3.5). These kind of filters are not suitable for measurements during the day due to the wide spectral transmittance range and strong background.

Daytime measurements would become are possible by using interference filters, which transmit only a very narrow wavelet band, selected to correspond the wavelength of the transmitted laser beam. The interference filters, in general, transmit the light more efficiently when the incidence angle of the light is normal to the plane of the filter. At the system on Otlica, the

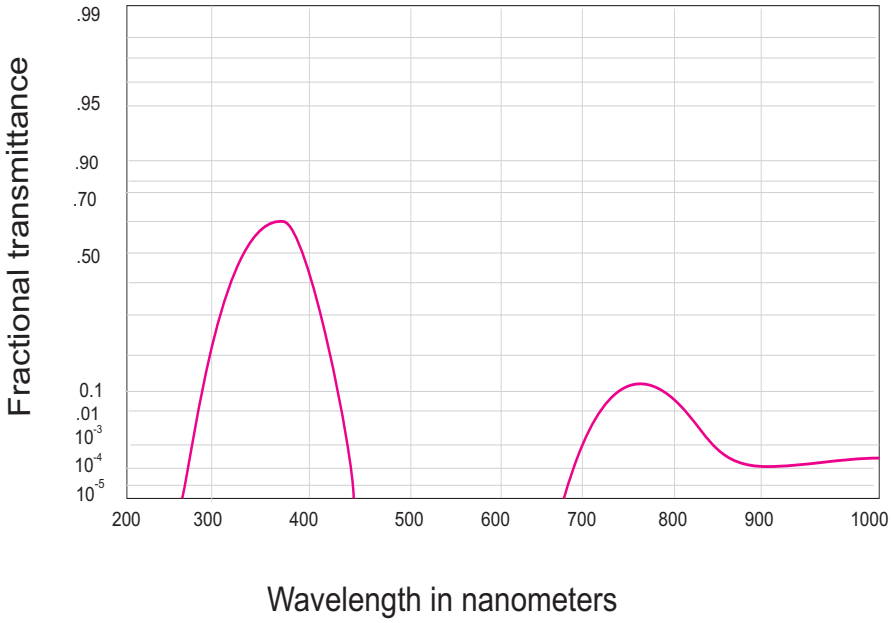


**Figure 3.5:** Transmisivity of the Schott Glass UG-1 filter has a maximum at 355 nm [35].

ratio of focal length and mirror diameter so called speed of mirror or f-number, is only 0.5. The majority of incidence angles due to this small ratio are not normal to the filter plane. Hence, usage of interference filters with present setup is not possible and measurements are performed only at night.
To be able to use interference filters within Otlica system, PMT has to be relocated from the focal point of the mirror. Besides, additional refracting mirrors or lenses need to be used in order to direct and colimate the light to the PMT. Future LIDAR upgrades would need to consider a design of a small optical aperture containing refractive mirrors and PMT, that would be placed in the focal point of the receiving mirror.

### Digitization

The signal from the PMT is transferred to a digitizer which is presented in Figure 3.6. For analog detection the signal is amplified and digitized by a 12bit 40MHz analog to digital converter with 16k trace length (current mode). It converts the average current from the PMT to a digital form suitable for recording. The resulting analog signal from the anode is the digital current portion of the pulses. This current is the sum of all pulses regardless of their source (e.g. cathode, dynode chain). Analog detection is appropriate in low range, since the signal is very strong in these ranges [36]. At the same time a fast 250MHz discriminator detects single photon events above a selected threshold voltage (photon counting mode). Using a combination of analog and photon counting detection the LICEL transient recorder is especially suited to record high dynamic range signals in LIDAR applications. Photon detection is not used in this analysis. The measurement in the tropospheric distances was achieved through analog detection. The range of the the instrument is determined by the number of digitizer channels (16.384) and the time difference between two neighboring measurements ($\tau_0 = 1/\nu = 25\,\mathrm{ns}$). The spatial resolution of $r_0 = c\,\tau_0/2 = 3.75\,\mathrm{m}$ gives a maximum reachable range of 60 km.

**Figure 3.6:** Signal digitizer LICEL TR40-160.

Data transfer as well as the input range and discrimination settings are performed via the standard PC parallel port [1].

### 3.1.2 LIDAR influence on health and environment

Safety concerns must be taken into account when using strong lasers and light transport components, as laser light can cause harmful biological effects. The basic and most important

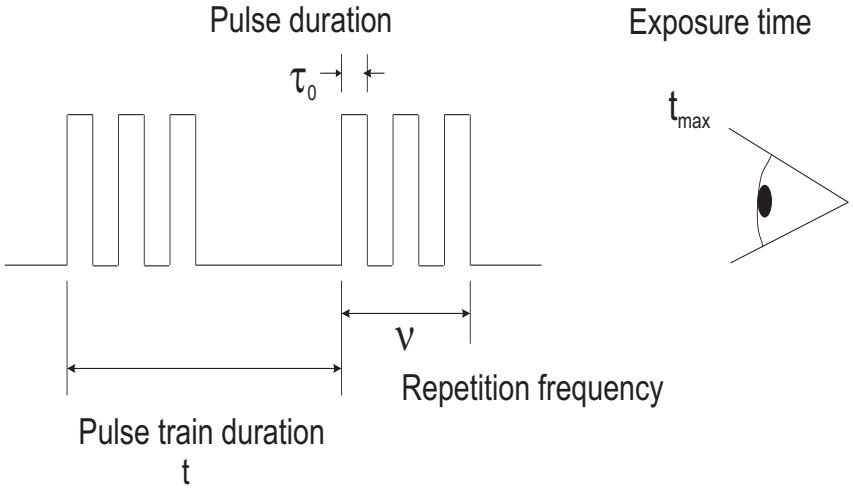


**Figure 3.7:** Schematic view of laser pulses indicating repetition frequency ($\nu$), duration of single pulse ($\tau_0$), total duration of a train of pulse ($t$) and total exposure time ($t_{max}$) [37].

variable that should be considered is the **M**aximum **P**ermissible **E**xposure (**MPE**). The MPE is the amount of radiation to which a person may be exposed without hazardous effects or adverse biological changes in the eyes or skin.
For lasers that transmit light in UV spectrum, MPE can be calculated as:

$$\mathrm{MPE} = 0.56 \cdot \tau_0^{1/4} \tag{3.1}$$

[1] IEEE1284 standard.

where $\tau_0$ is the duration of each pulse [39]. For the laser at Otlica, pulse duration is 5 ns and MPE $= 4.71\,\mathrm{mJcm}^{-2}$ [38].

Other important information that should be considered while evaluating the impact of lasers, is the **N**ominal **H**azard **Z**one (**NHZ**). The NHZ is the distance from the source of laser light at which radiation is below the MPE. Besides the wavelength of transmitted light, it is also necessary to consider the time of exposure, divergence of the laser beam and the beam path. In the case of the laser used at Otlica, diameter of the laser beam, $d$, can be presented in the form $d = \sqrt{a^2 + (r - r_0)^2 \cdot \epsilon^2}$, where $a$ is the beam diameter at the source of the beam, $\epsilon$ is the beam divergence and $r_0$ represents distance from the source where the diameter of the laser beam is minimal. With $d$, pulse energy $Q$ and the condition of $r_0 << r$ energy density for each pulse [39] is calculated as In our case, for $a = 9\,\mathrm{mm}$ at the beam source ($r = 0$) and a maximal pulse energy of $Q = 120\,\mathrm{mJ}$, energy density in the beam radius is $\mathrm{H}_{direct} = 186.63\,\mathrm{mJcm}^{-2}$. So the value at the source is higher than the MPE. The beam

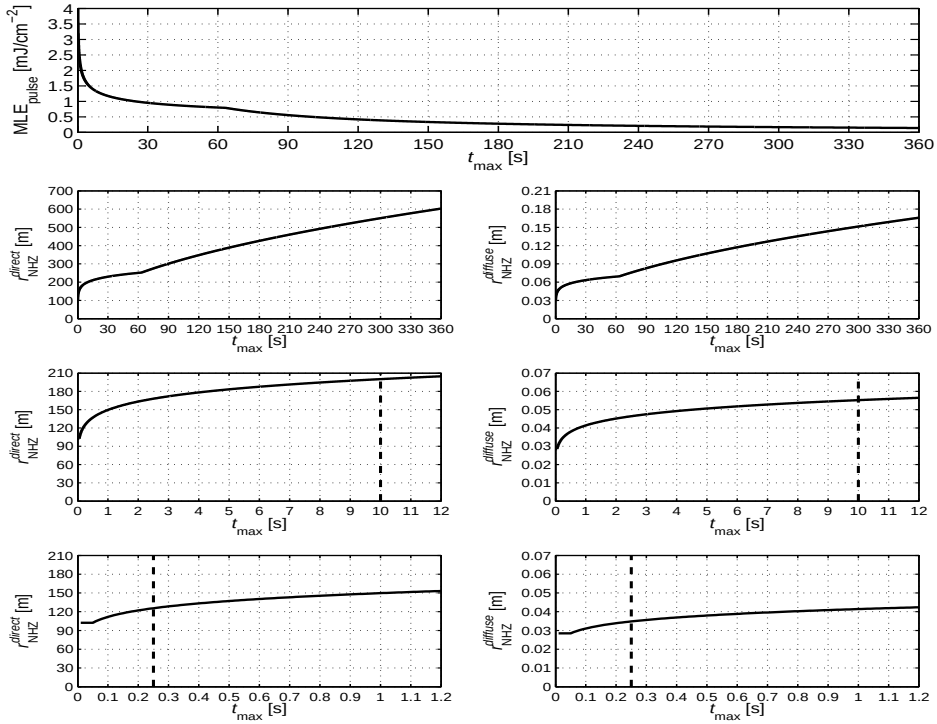


**Figure 3.8:** Maximum Permissible Exposure (MPE) and Nominal Hazard Zone (NHZ) with respect to the time of exposure. The LIDAR measurements are usually taken in a range of minutes (from 5 to 30).

radius becomes larger as laser light propagates and energy density is decreased. The distance where the beam diameter gets so large that $\mathrm{H}_{direct} < \mathrm{MPE}$, is calculated as:

$$\mathrm{H}_{direct} = \frac{Q}{\frac{\pi}{4}\left(a^2 + r^2\,\epsilon^2\right)} \tag{3.2}$$

$$\mathrm{r}_{\mathrm{NHZ}}^{\mathrm{direct}} = \frac{1}{\epsilon}\sqrt{\frac{4\,Q}{\pi\,\mathrm{MPE}} - a^2} \tag{3.3}$$

In our case $r_{NHZ}^{direct} = 102.25\,\text{m}$. At that distance the beam radius has a value $d_r = 57\,\text{mm}$ which is the width of impact region for each pulse.
All calculations are done for a single pulse of laser light. For pulsed lasers, due to a high peak intensity, the MPE is more complicated than for equivalent continuous sources. To determine the correct MPE for a given train of pulses, some rules should be obeyed [37]:

1. Value of $\text{MPE}_{\text{pulse}}$ is limited with MPE value for each pulse as given in Equation (3.1). Since the laser at Otlica has $\nu = 20\,\text{Hz}$ with laser pulse duration of 5 ns, the MPE has a value of $4.71\,\text{mJcm}^{-2}$.

2. Value of $\text{MPE}_{\text{pulse}}$ is limited with MPE for all exposure times between $t$ and $t_{max}$, divided by the number of pulses $n$ during that time period (average power limit):

$$\text{MPE}_{\text{pulse}} = \frac{\text{MPE}}{n} = \frac{\text{MPE}}{t_{max}\,\nu} \tag{3.4}$$

   where $\nu$ is laser frequency (Figure 3.7).

3. The $\text{MPE}_{\text{pulse}}$ is limited to the MPE for a single pulse multiplied by $n^{-1/4}$, where $n$ is the number of pulses that occur during the period of exposure $t_{max}$ (repetitive pulse limit):

$$\text{MPE}_{\text{pulse}} = \frac{\text{MPE}}{n^{-1/4}} = \frac{\text{MPE}}{t_{max}^{-1/4}\,\nu^{-1/4}}. \tag{3.5}$$

   A safe MPE value for an exposure time of 0.25 s, in the case of the laser at Otlica is $6.9 \cdot 10^{-3}\text{Jcm}^{-2}$ [37].

Limiting values for eye safety of UV lasers, as noted in ANSI standard [40] are:

- for the time of exposure from $10^{-9}\,\text{s}$ to $10\,\text{s}$: $\text{MPE} = 0.56\,\text{Wcm}^{-2}\,\tau_0^{1/4}$.
- for the time of exposure from $10\,\text{s}$ to $3 \cdot 10^4\,\text{s}$: $\text{MPE} = 10^{-3}\text{Wcm}^{-2}$.

For skin and eye safety, standard [40] gives additional limitations:

- for the time of exposure from $10\,\text{s}$ to $10^3\,\text{s}$: $1.7 \cdot 10^{-2}\,\text{Jcm}^{-2}$.
- for the time of exposure from $10^3$ to $3 \cdot 10^4\,\text{s}$: $10^{-3}\,\text{Wcm}^{-2}$

Distributions of MPE and NHZ values depending on the time of exposure are presented in Figure 3.8. With decrease of MPE intensity, time of exposure prolongs. Low radiation power provides longer exposure time, without suffering any damage. With a larger distance from the laser, NHZ is larger and exposure time is longer.

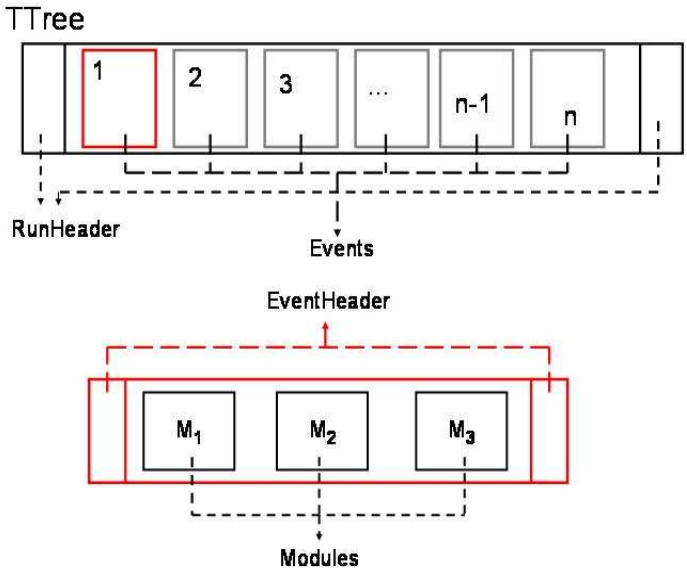


**Figure 3.9:** Schematic representation of the data storage in ROOT objects (classes), branches and events, as well as module (receiver).

### 3.1.3 LIDAR data structure

Software for the data analysis is written in C++ computer language [41]. ROOT [42] is an object oriented graphic framework suitable for large sets of data and was used in this analysis. The structure of the software for data collection is ROOT class based with separate classes having different roles.
Collected data is stored in root binary files. The main ROOT class is the TObject class, mother of all ROOT objects and binary files. The TObject class provides default behavior and protocol for all objects in the ROOT system. This class stores information for object I/O, error handling, sorting, inspection, printing, drawing, etc. Every object which inherits members of TObject is stored in the ROOT collection classes.
The class TRunHeader contains basic information about the LIDAR data, e.g. acquisition starting time, the total number of events, number of operational digitizer modules, the PMT voltages, the laser power, as well as some remarks and comments.
Another important class is the TLEvent object. It is used as data storage for the signal provided by all operating LICEL transient recorders. TLEvent has its own acquisition time and is distinct for different initial settings, like zenith and azimuth orientations. Here the number of laser shots is stored.
The sum of the 20 laser shots constitute an event. Since one measured event does not contain enough statistics, they are summed and averaged into runs. Different cases that will be shown, are representing different day measurements. There are multiple runs taken on every day of measurement, but one representative run is analyzed for each day.
During the acquisition runs, the temporal sequence of LIDAR events is stored in a file following the TTree structure (Figure 3.9). In ROOT, TTree structure is made of a series of TBranchs (in this case assigned to TLEvent objects) that are read independently of each other.

## 3.2 LIDAR equation

The LIDAR detected signal is described by the LIDAR equation. The equation connects the intensity of back-scattered light with atmospheric absorption and scattering parameters:

$$P(r) = P_0\, k\, \frac{c\tau_0}{2}\, \beta(r)\, \frac{A}{r^2}\, T^2(r) \tag{3.6}$$

The $P(r)$ is the signal of the received back-scattered light at time $t$ from distance $r$, $P_0$ is transmitted laser power at time $t_0$, $k$ is system efficiency, $c$ is the speed of light, $\tau_0$ is the laser pulse width and $A$ is the effective receiving area of the detector [43]. The quadratic decrease of the signal intensity with distance $r$ is present due to the fact that the receiver mirror area makes up a part of a sphere's surface with radius $r$ [1]. The solid angle $A/r^2$ gives the perception angle of the LIDAR for light scattered at distance $r$. These parameters are indicated in the LIDAR equation illustration given in Figure 3.10. The term $\beta(r)$ given

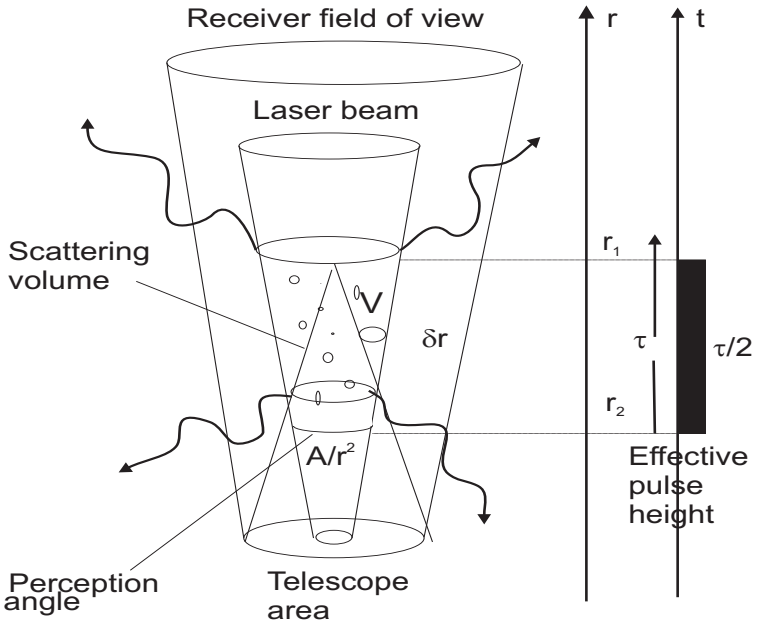


**Figure 3.10:** Illustration of the LIDAR equation: laser light that travels in time and space (t, r) is scattered within a volume viewed by acceptance angle of the mirror [1].

in units of $\mathrm{m}^{-1}\mathrm{sr}^{-1}$, represents a volume back-scattering coefficient. It stands for the ability of the atmosphere to scatter light back into the direction from which it came.
The term $T(r)$ refers to the transmission ability of the atmosphere for photons traveling from the ground to a given distance $r$ [1]. In the LIDAR equation, $T(r)$ appears squared, since the photons have first to travel to and then return from the distance $r$. Usually this attenuation term is described as a negative exponential, by the so called "Bouguer-Lambert law"[25]:

$$T(r) = e^{-\tau(r)} = e^{-\int_0^r \alpha(r)\, dr} \tag{3.7}$$

where $\tau(r)$ is the optical depth, and $\alpha(r)$ is the linear attenuation coefficient. The Bouguer-Lambert law is essentially valid when all multiple scattered energy is permanently removed from the outgoing LIDAR beam. This is the case for fairly transparent atmospheres.
When the geometrical decrease of the signal is compensated, the LIDAR equation is presented in terms of the so called range corrected or range normalized signal [25]:

$$P_{cor}(r) = P(r)\, r^2 = C\, \beta(r)\, e^{-2\int_0^r \alpha(r)\, dr} \tag{3.8}$$

where $C$ is a constant that gathers all constant values ($P_0$, $k$, $c$, $A$ and $\tau_0$). The range corrected signal is a function of two unknowns $\beta(r)$ and $\alpha(r)$. Hence, the LIDAR equation can not be solved without introducing an additional relation between $\alpha$ and $\beta$.

## 3.3 Fernald method

Besides light extinction and scattering of molecules, light is absorbed and scattered on various types of aerosols. In the case of a high aerosol concentration, the molecular component of the scattering can be ignored [3], however, this is not the case for the Otlica LIDAR. Due to the sensing of the atmosphere using the light of $355\,nm$, the scattering of light on molecules has to be considered [36, 44]. The procedure to solve the LIDAR equation in such a case was proposed by Fernald [44] and exploits a relation between the extinction and the back-scattering coefficients in a two component atmospheric model. This approach was used through the present analysis.
Usual relation between extinction and back-scattering coefficients, in a two component atmospheric model, is:

$$\begin{aligned} \alpha &= \alpha_m + \alpha_a \\ \beta &= \beta_m + \beta_a = P_m(180^o)\, \alpha_m + P_a(180^o)\, \alpha_a \end{aligned} \tag{3.9}$$

where $\alpha_m$ and $\alpha_a$ are molecular and aerosol extinction coefficients, $\beta_m$ and $\beta_a$ are molecular and aerosol back-scattering coefficients. $P_a$ is the aerosol phase function. For the molecular part we assume the usual Rayleigh phase function $P_m(180^o) = 3/8\pi\,\mathrm{sr}^{-1}$. In Fernald's approach, the basic assumption is that molecular extinction and back-scattering coefficients of the atmosphere ($\alpha_m$ and $\beta_m$) are reasonably well known [45]. Furthermore, we can define phase function $F$ as $F = P_m(180^o)/P_a(180^o)$. From the light scattering theory, $\alpha_a$ and $\beta_a$ are related by the expression $R = \alpha_a/\beta_a$, so that $F = RP_m(180^o)$ [44]. Depending on the aerosol type, $R$ is assumed to be in the range $10 < R < 100$ [46] and $P_a = 1/R$. A atmosphere containing particles of smaller sizes is better described by $R$ values closer to the lower limit, while an atmosphere containing the larger particles is better described by $R$ values higher than 40 [47].
This variation can be explained by analyzing the scattering direction as a function of particle size (Section 2.2). Scattering of light of small diameter aerosols is almost isotropic, similar to the pure molecular scattering [1]. This results in the LIDAR ratio being more similar to the molecular ratio i.e $\beta_m/\alpha_m = 8\pi/3\,\mathrm{sr}^{-1}$. However, in the case of the higher aerosol diameter, forward peaked scattering is present. Thus, the amount of light directed backwards

is relatively low and the LIDAR ratio value is relatively high.
After introducing the range corrected function $S(r) = \ln[P(r)r^2/P_0\, r_0^2]$, the LIDAR equation can be written as:

$$S(r) = \ln\,[\frac{\beta(r)}{\beta(r_0)}] - 2\,\tau(r) = \ln\,[\frac{\beta_m(r) + \beta_a(r)}{\beta_m(r_0) + \beta_a(r_0)}] - 2\int_{r_0}^{r}(\alpha_m(\tilde{r}) + \alpha_a(\tilde{r}))\,d\tilde{r} \tag{3.10}$$

where $r_0$ first measured altitude and $\tilde{r}$ is an arbitrary height. Differential of the above equation is:

$$S'\,(r) = \frac{[\beta_m(r) + \beta_a(r)]^{'}}{\beta_m(r) + \beta_a(r)} - 2\,[\alpha_m(r) + \alpha_a(r)] \tag{3.11}$$

Let us multiply the first part of above equation with one, i.e $1 = F/F = \frac{P_m/P_a}{P_m/P_a}$ and add to the second part a zero in the form of $0 = F\alpha_m - F\alpha_m$. Then the equation has a following shape:

$$S'\,(r) = \frac{[P_m\,\alpha_m(r) + P_a\,\alpha_a(r)]^{'}}{P_m\,\alpha_m(r) + P_a\,\alpha_a(r)}\frac{P_a}{P_a} - 2\,[\alpha_m(r) + \alpha_a(r) + F\,\alpha_m(r) - F\,\alpha_m(r)] \tag{3.12}$$

Rearranging the above equation gives the form:

$$S'\,(r) - 2\,[F-1]\,\alpha_m\,(r) = \frac{[F\,\alpha_m\,(r) + \alpha_a\,(r)]^{'}}{F\,\alpha_m\,(r) + \alpha_a\,(r)} - 2\,[F\,\alpha_m\,(r) + \alpha_a\,(r)] \tag{3.13}$$

Let us reshape the last equation dividing it with $F\alpha_m + \alpha_a$. Then the equation reads as:

$$\frac{S'\,(r) - 2\,[F-1]\,\alpha_m\,(r)}{F\,\alpha_m(r) + \alpha_a(r)} = \frac{[F\,\alpha_m\,(r) + \alpha_a\,(r)]^{'}}{[F\,\alpha_m\,(r) + \alpha_a\,(r)]^2} - 2 \tag{3.14}$$

This type of differential equation is solved using substitution. In this case, the substitution is $u(r) = (F\,\alpha_m(r) + \alpha_a(r))^{-1}$. To simplify the equation even more, let us introduce one more substitution $S_n^{'}(r) = S'\,(r) - 2\,[F-1]\,\alpha_m\,(r)$. Now, the equation has the shape:

$$S_n^{'}(r)\,u(r) = u^{'}(r) - 2 \tag{3.15}$$

The solution of the equation (3.15) is:

$$u(r) = e^{-S_n^{'}(r)}(N - 2e^{\int_{r_0}^{r} e^{S_n^{'}(\tilde{r})}d\tilde{r}}) \tag{3.16}$$

where $N$ is a differential constant. Using the boundary condition $u(r_0) = u_0$, constant $N$ is retrieved:

$$N = \frac{e^{S_n'(r_0)}}{u_0} \tag{3.17}$$

Returning back all substitutions included earlier, the solution is:

$$F\alpha_m + \alpha_a = \frac{e^{S(r)-2[F-1]\int_{r_1}^{r}\alpha_m(\tilde{r})d\tilde{r}}}{(F\,\alpha_m + \alpha_a)_f^{-1}\, e^{S_f-2[F-1]\int_{r_1}^{r_f}\alpha_m(\tilde{r})d\tilde{r}} + 2\int_r^{r_f} e^{S(\tilde{r})-2[F-1]\int_{r_1}^{r'}\alpha_m(\hat{r})d\hat{r}}d\tilde{r}} \tag{3.18}$$

where $S_f$ represents the value of $S$ at far end, $r_1$ is an arbitrary reference distance between $r_0$ and $r_f$, and $\alpha_m$ and $\alpha_a$ are taken for the $r_0$. The above equation can be simplified multiplying the numerator and denominator by $e^{2[F-1]\int_{r_1}^{r_f}\alpha_m(r_1)dr_1}$. The final solution is:

$$\alpha_a(r) = \frac{e^{S(r)+2[F-1]\int_{r}^{r_f}\alpha_m(\tilde{r})d\tilde{r}}}{[F\alpha_m(r_0) + \alpha_a(r_0)]_f^{-1}\, e^{S_f} + 2\int_r^{r_f} e^{S(\tilde{r})+2[F-1]\int_{\tilde{r}}^{r_f}\alpha_m(\hat{r})d\hat{r}}d\tilde{r}} - F\alpha_m(r). \tag{3.19}$$

This solution with the back-scattering coefficient calibrated using the final range $r_f$ (they are calculated backward, from final range) is highly stable. As $r$ decreases from the end of the exploring range, $\alpha(r)$ becomes the ratio of two numbers progressively larger. Here it is assumed that $S(r)$ generally decreases with increasing range $r$. This occurs in most practical applications due to the extinction term in the LIDAR equation [48]. It should be noted again that the Fernald method relies on the accuracy of several external parameters, which are based on method independent knowledge about the molecular part of light extinction in the atmosphere. These are:
(a) scattering profiles $\alpha_m(r)$ and $\beta_m(r)$,
(b) total extinction at the far end of the profile, $\alpha_m(r_f)$,
(c) proper approximation of the LIDAR ratio $R$.
From these, according to the theory of Mie scattering, the LIDAR ratio is most difficult to obtain [22].

### 3.3.1 Method assumptions

In the Fernald method, absorption and back-scattering coefficients consist of aerosol and molecular parts. The molecular extinction, $\alpha_m$, and back-scattering $\beta_m$ coefficients, as well as the molecular density profile in the atmosphere, are reasonably well known. In this work, the atmosphere profile is derived from the 1976 US Standard Atmosphere [50] model and, in order get best possible accuracy of the aerosol and molecular extinction and back-scattering coefficients, the model data are complemented with radiosonde measurements of atmospheric characteristics for altitudes up to 32 km. The radiosonde data are taken from the Integrated Global Radiosonde Archive [51] and are available at the information service web site. Since there are no radiosonde measurements for the exact location of Otlica LIDAR observatory,

the data used is for the nearest place where daily measurements are made (Udine, Italy, 40 km away). A more detailed description of the molecular profile calculation is given in Appendix A.
The Fernald inversion method introduces the following assumptions:

1. values for LIDAR ratio $R = \alpha_a/\beta_a$ are taken to be between 10 and 100, depending on the weather conditions and type of aerosol assumed to be present;
2. the height dependence of the aerosol back-scattering phase function is unknown and will be assumed to be constant with the height $P_a = 1/R$;
3. standard molecular extinction profiles are used complemented with additional radiosonde data;
4. aerosol attenuation coefficient at far height is assumed to be zero;

### 3.3.2 Statistical error calculation

Detection of back-scattered signal using the PMT represents the source of measurement error [22]. Photon detection is a statistical process that undergoes the Poisson distribution [23]. For the Poisson distribution, relative error of the signal is:

$$\frac{\sigma\left(P(r)\right)}{P(r)} = \frac{1}{\sqrt{N_\gamma}} \tag{3.20}$$

where $N_\gamma$ is the number of photons, which is proportional to the power of the back-scattered signal by:

$$N_\gamma = K^{-2}\, P(r) \tag{3.21}$$

due to the PMT amplification. The error of the measured signal is then:

$$\sigma\left(P(r)\right) = K\sqrt{P(r)} \tag{3.22}$$

for signal detected at a different measured range $r$. The coefficient $K$ needs to be determined from a fit.

For the sake of convenience, the equation (3.22) can be rewritten in a logarithmic form, so that a linear dependence between $\log(P)$ and $\log[\sigma(P)]$ can be clearly seen:

$$\log\left[\sigma\left(P(r)\right)\right] = \log\left[K\right] + k\log\left[P(r)\right] \tag{3.23}$$

In these coordinates the offset of the linear relation is related to $K$, while the slope is related to the power $k$ relating the error to the signal. Ideally, we would expect $k = 0.5$ if the process were indeed Poissonian. To smooth the overall fluctuation when estimating the signal error, we normalize the signal $P(r)$ to the signal power at lowest height, $p = P(r)/P_0$ is performed. The error for each event point (corresponding to back-scattering from different altitudes) is calculated as:

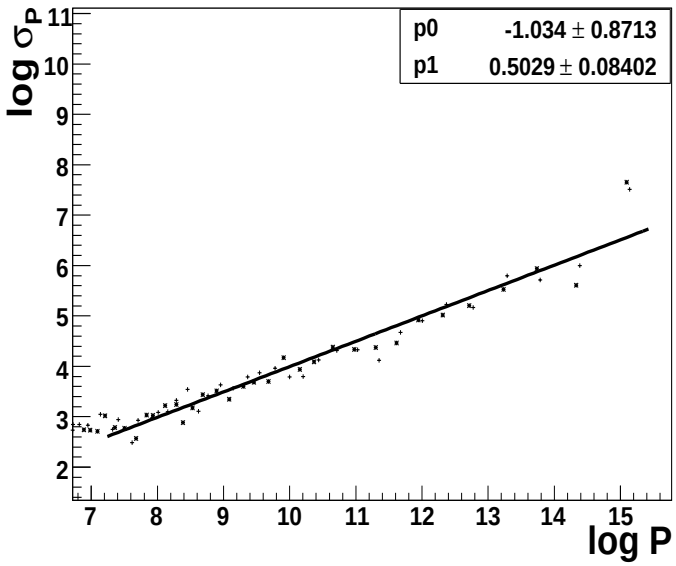


**Figure 3.11:** Dependence of logarithm of the signal error, $\sigma\left(P(r)\right)$ on the logarithm of the signal. The linear least square fit provides coefficients $K$ and $k$, with obtained fit equation: $\log\left[\sigma\left(P\right)\right] = 0.5\log[P] - \log[1.03]$. Two different markers denote the data from two different events.

$$\sigma\left[p(r)\right]^2 = \bar{p^2} - \bar{p}^2 \tag{3.24}$$

where:

$$\overline{p}^2 = \left(\frac{1}{N_{ev}} \sum_{1}^{N_{ev}} p\right)^2 \tag{3.25}$$

and

$$\overline{p^2} = \frac{1}{N_{ev}} \sum_{1}^{N_{ev}} p^2. \tag{3.26}$$

with $N_{ev}$ as a number of events.

The linear fit of data is used to determine coefficients $k$ and $K$. Statistical error with respect to the signal is presented in Figure 3.11. Separate points for each event (the two events are noted by different markers) correspond to the back-scattered signal from different altitudes. The linear least square fit is performed to data and attempts to find a function which closely approximates the data ("a best fit"). Since there is no error for $\sigma[p(r)]$ it is calculated as linear regression: $\chi = \sum_{i=1}^{N} \left(\sigma[p(r)_{exp}] - \sigma[p(r)_{fit}]\right)^2$, i.e as a sum of squared difference between the all obtained values (in total $N$), and values calculated from a fit using

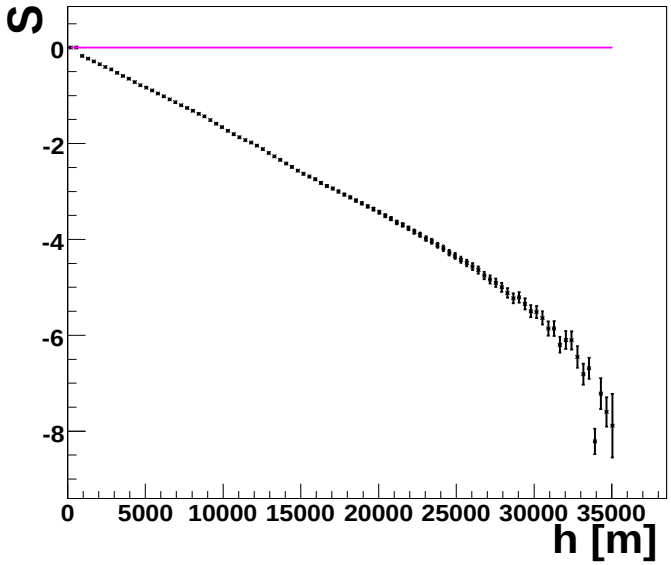


**Figure 3.12:** The S-function dependence on height (given in meters) - an example of clear day signal taken with Otlica LIDAR on the $1^{st}$ of September 2006. The error values is low and to be better visible is increased by rescaling with a factor of 10. A typical increase of absolute error with the height can be seen.

the obtained coefficients. The linear least square fit of the data, reveals that within errors of 10% $k = 0.5$ and that the process can be accurately described by Poisson statistics. Since the logarithms of $\sigma\left[P(r)\right]$ and $P(r)$ are given in base 2 in the figure, the proportionality constant $K$ is equal to , $K = 2^{-1.03} = 0.49$. Thus, the error in the signal can be estimated by:

$$\sigma\left(P(r)\right) = 0.49\sqrt{P(r)}. \tag{3.27}$$

The error of the $S$ function is calculated as the derivative of the equation $S = \ln P(r)\, r^2$ with respect to $P(r)$. It has the form:

$$\sigma\left(S(r)\right) = \frac{\sigma\left(P(r)\right)}{P(r)}. \tag{3.28}$$

The $S$ function of a typical signal measured during the clear sky day is given in Figure 3.12. The error for $\alpha_a$ is calculated as an derivative of equation (3.19) with respect to the $S(r)$ i.e the statistical uncertainties have been calculated from the law of error propagation. Errors for $\alpha_a$ are decreasing with height, since the calculation of $\alpha_a$ and $\beta_a$ is performed backward. Optical depth integration is performed from the ground. Its error increases with height. It should be noted that the statistical error are just part of errors that accounts in the presented measurements. Namely, the systematic error present due to the alignment performed by hand and different assumptions given in Fernald method, build a part of the total error.

## 3.4 DREAM model

The **D**ust **RE**gional **A**tmospheric **M**odel (**DREAM**) [53] is a model designed to simulate and/or predict the atmospheric cycle of mineral dust aerosol. The vertical profiles of desert dust concentration above the Otlica region predicted by this model are used. From this additional information about the type of aerosols detected by the LIDAR system is available. DREAM model solves the Euler-type partial differential non-linear equation for dust mass continuity. The concentration equation simulates all major processes of the atmospheric dust cycle. During the model integration, calculation of the surface dust injection fluxes is made over the model cells declared as deserts [53]. Once injected into the air, dust aerosol is driven by the atmospheric model variables: by turbulence in the early stage of the process when dust is lifted from the ground to the upper levels; by winds in the later phases of the process when dust travels away from the sources; and finally, by thermodynamic processes and rainfall of the atmospheric model and land cover features which provide wet and dry deposition of dust over the Earth surface [53]. One of the key components of the dust model is the treatment of the source terms in the dust concentration continuity equation. Failure to adequately simulate and predict the production phase of the dust cycle leads to incorrect representation of all other dust processes in the model. Therefore, special attention is paid to properly parametrize the dust production phase. Wind erosion of the soil in the DREAM parametrization scheme is controlled mainly by the type of soil, type of vegetation cover, soil moisture content, and surface atmospheric turbulence. The major input data used to distinguish the dust producing soils from the others is a global data set on land cover. Other data used in dust production calculations is a global soil texture data set from which particle size parameters are evaluated. The DREAM model has delivered operational dust forecasts over the Mediterranean region and over East Asia in the last few years.

## 3.5 Analysis of air trajectories

While the presence of aerosols in the atmosphere depends on air mass history, the properties of the aerosols depend on their origin. Hence, it is important to obtain information about air trajectories describing the flow of air arriving to some regions.

### 3.5.1 Air trajectory models

Trajectory models are used to study dynamic processes in the atmosphere. They describe the paths of air parcels during a given time period. The air motions are described with two different perspectives: Eulerian and Lagrangian [54, 55]. The Eulerian perspective considers air flows through points fixed in space while the Lagrangian perspective focuses on individual air parcels as they move through time and space. Lagrangian based particle trajectory models are useful for studying the transport of atmospheric constituents such as aerosols [31, 56].
Trajectory modeling is based on differential equations of motion. Assuming a specific infinitesimally small air parcel, its trajectory is defined by the following differential trajectory equation [31]:

$$\frac{dX}{dt} = \dot{X}[X(t)] \tag{3.29}$$

where $t$ is the time, $X$ is the position vector and $\dot{X}$ the wind velocity vector. If the initial position $X_0$ at time $t_0$ of the parcel are known, the path is completely determined by:

$$X(t) = X(X_0,\, t) \tag{3.30}$$

The inverse transformation:

$$X_0(t = t_0) = \chi(X,\, t) \tag{3.31}$$

gives the initial coordinates of the parcel. At time $t$ the air parcel is at position $X$. Thus, air parcels may be followed either forward (forward trajectories) or backward (back trajectories) in time. The spatial coordinates $X_0$ at time $t_0$ provide an information for identifying each air parcel for all times. These initial coordinates are called "material" or "Lagrangian coordinates" [31].
The solution of the above equation is only obtained analytically for simple flow fields [57]. Expansion of $X(t)$ in a Taylor series around $t = t_0$ and evaluation at $t_1 = t_0 + \triangle t$, gives:

$$X(t_1) = X(t_0) + (\triangle t)\frac{dX}{dt}\Big|_{t_0} + \frac{1}{2}(\triangle t)^2\,\frac{d^2X}{dt^2}\Big|_{t_0} + ... \tag{3.32}$$

The first approximation is then:

$$X(t_1) = X(t_0) + (\triangle t)\dot{X}(t_0) \tag{3.33}$$

This is a "zero acceleration solution" . This solution is computationally useful since it involves no iteration. It is accurate to the first order. Differences between the real and the numerical solution occur from the omission of higher order terms. If trajectories are calculated using very short integration time steps, equation (3.33) can be of sufficient accuracy [57].

### 3.5.2 HYSPLIT model

The trajectory model used in this work is a commonly used model called **HY**brid **S**ingle-**P**article **L**agrangian **I**ntegrated **T**rajectory (**HYSPLIT**) [58] developed by the NOAA Air Resources Laboratory. The HYSPLIT model is the version of a complete system for computing simple air parcel trajectories to complex dispersion and deposition simulations. This model features include advection algorithms, stability and dispersion equations, a graphical user interface, and the option to include modules for chemical transformations. Without the additional dispersion modules, HYSPLIT computes the advection of a single pollutant particle or simply its trajectory [58].
The dispersion of particles is calculated by assuming either puff or particle dispersion. In the puff model, puffs expand until they exceed the size of the meteorological grid cell[2], either

[2]Meteorological grid models use mathematical formulations that simulate atmospheric processes such as the change of winds and temperature in time. These meteorological parameters are calculated at distinct spatially equidistant points over an area of interest which is called a grid [59].

horizontally or vertically. Then it splits into several new puffs, each with its share of the pollutant mass.
In the particle model, a fixed number of initial particles are advected about the model domain by the mean wind field and a turbulent component. The model's default configuration assumes a puff distribution in the horizontal direction and particle dispersion in the vertical direction. In this way, the greater accuracy of the vertical dispersion parametrization of the particle model is combined with the advantage of having an ever expanding number of particles representing the pollutant distribution. The model can be run interactively on the Web page of the NOAA Air Resource Laboratory through the READY system or the executable code and meteorological data can be downloaded to a Windows operated PC. The trajectories for purpose of this thesis study were calculated by HYSPLIT using the **G**lobal **D**ata **A**ssimilation **S**et, **GDAS**, with 1x1 degree of horizontal resolution, and one hourly time resolution. The trajectories, presented in analysis, are calculated for the three days backward and plotted with the labeling option of six hours.

## 3.6 Cluster analysis

To group the transport paths of the similar history and origin, **C**luster **A**nalysis (**CA**) [64] is performed. Inside the selected cluster, trajectories are more similar to each other than they are to trajectories in other clusters in terms of their arrival directions.
The goals of clustering are to have group members differ as little as possible and each group as distinct as possible from other groups. The measure of dissimilarity in the case of air trajectories is distance.

### 3.6.1 Distance between trajectories

Central to the clustering and trajectory dissimilarities is the idea of distance. Trajectories grouped in clusters can be treated as number of points, separated for the same observation period by small distances relative to the distance between the clusters. Distances between points determining different trajectories are calculated by using the Euclidean distance. This measure of dissimilarity is extended to more than two variables (dimensions) without difficulty. Other distance measures (metrics) may also be calculated.
The most intuitive and commonly used distance measure in cluster analysis is the Euclidean distance in the $M$-dimensional space of the data vectors. The distance between two trajectories $X_i$ and $X_j$ is

$$d_{i,j} = \|X_i - X_j\| = \left[\sum_{m=1}^{M}(x_{i,m} - x_{j,m})^2\right]^{1/2} \tag{3.34}$$

where identifiers $i$ and $j$ represent different trajectories. The $M$ is the number of points per trajectory determined by the length of trajectory and time resolution. Euclidean distances are calculated between coordinates of trajectory points for the same time period. They are then summed up in order to obtain an estimate of the distance between trajectories in a Euclidean sense.
Since the data taken from the NOAA site [58] is given in geodetic (spherical) coordinates,

Euclidean distances are calculated after a transformation of the coordinates to Cartesian ones. Using the trigonometrical transformation, Cartesian coordinates $x, y$ and $z$ are:

$$\begin{aligned} x &= r\ \sin\theta\ \cos\vartheta \\ y &= r\ \sin\theta\ \sin\vartheta \\ z &= r\ \cos\theta \end{aligned} \tag{3.35}$$

where the $r$ is the distance from the origin of the system, $\theta$ zenith angle and $\vartheta$ is azimuth angle.
With this simple transformation, the origin of the system is in the center of the Earth. Further transformations are necessary to obtain a system with the origin at the observation point i.e. Otlica. Translation and rotation of the present system is needed to obtain a new local reference system. The new coordinates are:

$$[X, Y, Z]_{loc} = A^{-1}\left[(x, y, z)_t^{\mathrm{CE}} - (x, y, z)_{op}^{\mathrm{CE}}\right] \tag{3.36}$$

where $(x, y, z)_t^{\mathrm{CE}}$ are generic point coordinates of trajectory and $(x, y, z)_{op}^{\mathrm{CE}}$ observation point coordinates. These coordinates have a system with the origin in the center of the Earth (CE). $A$ is a rotation matrix of shape:

$$A = \begin{pmatrix} -\sin\Phi_g\ \cos\vartheta_g & -\sin\vartheta_g & \cos\Phi_g\ \cos\vartheta_g \\ -\sin\Phi_g\ \sin\vartheta_g & \cos\vartheta_g & \cos\Phi_g\ \sin\vartheta_g \\ \cos\Phi_g & 0 & \sin\Phi_g \end{pmatrix} \tag{3.37}$$

where $\Phi_g$ and $\vartheta_g$ are Otlica's geodetic coordinates (latitude and longitude).

### 3.6.2 K - means clustering method

In this work the cluster analysis is used to splitt the air trajectories into a number of distinct groups. These groups would contain trajectory members with similar histories in terms of their direction of approach and speed of passage over different regions. On this way typical directions of air masses reching Slovenia region are determined. There are many clustering methods that can be used in this purpose. The criteria used differ and different classifications are obtained for the same data [65]. Thus, although cluster analysis may provide an objective method for the clustering, subjectivity in the choice of method is present. Clustering methods are divided into two basic types: hierarchical and partitional. Many subtypes and different algorithms exist within each of the clustering approaches [64].
Hierarchical clustering proceeds successively by either merging smaller clusters into larger ones or by splitting larger clusters. The end result of the algorithm is a tree of clusters, called a dendrogram, showing how the clusters are related. By cutting the dendrogram at a desired level a clustering of the data items into disjoint groups is obtained [66].
Partitional clustering attempts to directly decompose the data into a set of disjoint clusters. The criterion function that the clustering algorithm tries to minimize may emphasize the local structure of the data. Typically, the global criteria involve minimizing the distances in the data within each cluster, while maximizing the distances of different clusters [64].

While many different clustering algorithms exist, there is much variation in the computational requirements for interpretation of the data. Clustering the trajectories, calculated with the HYSPLIT model of the NOAA Research Laboratory, in this thesis is done using partitional clustering method called the K - means method [64]. This model is chosen since non-hierarchical clustering methods are very well designed for large amount of data. It also has a relatively small requirement for computational storage.
Data used for input are air trajectories that are at least 48 hours long. Each hour is considered as a one trajectory point. The points are given in Cartesian coordinates and the 48 of them build one trajectory.
The K-means method aims to minimize a distance function, in this case a squared error function:

$$J = \sum_{j=1}^{M} \sum_{i=1}^{N} \|X_i^{(j)} - K_j\|^2 \tag{3.38}$$

where $\|X_i^{(j)} - K_j\|^2$ is the Euclidean distance between point of trajectory $X_i^{(j)}$ and cluster centroid $K_j$. The centroid of a cluster is a point whose parameter values are the mean of the parameter values of all the points in the clusters. The $M$ is number of data points and $N$ number of trajectories.
The clustering algorithm is composed of the following steps:

1. First, the number of clusters, $K$, into which data would be optimally assigned is suggested. Usually, clustering is performed for different numbers of clusters and after appropriate validation the optimal cluster number is chosen.

2. Next, the Euclidean distance between the trajectories and clusters is determined.

3. Finally, minimization of total inter-cluster variance between trajectories and centroids is performed. Each trajectory is assigned to the cluster that is closest in terms of Euclidean distances.

However, the K - means algorithm does not necessarily find the most optimal configuration corresponding to the global objective function minimum [67]. The result of the clustering algorithm (that in many cases can be arbitrary itself) can be interpreted in different ways. Another potential problem is that the selection of the optimal number of clusters may be critical: different kinds of clusters may emerge when $K$ is changed [62].

### 3.6.3 Clustering validation

The prediction of the optimal number of clusters is a critical problem in classification problems [63]. Different cluster validity induces have been suggested to address this problem [63]. A cluster validity value indicates the quality of a resulting clustering process. Two validation methods are applied: the Silhouette method [64] and **R**oot **M**ean **S**quare **D**eviation (**RMSD**) [21].

**Silhouette method**

The silhouette method is in principle a method that represents how well are trajectories grouped around centroids. The entire clustering is evaluated after averaging all silhouette values for each cluster, or each clustering case (if the different number of clusters is considered) [32]. The low silhouette value indicates that the trajectories are not well assigned to the certain cluster [32]. Calculation of silhouette values is given in the following steps [64]:

- It is assumed that trajectory $i$ belongs to some cluster $A$. The distance between $i$-th trajectory and other trajectories belonging to cluster $A$ is calculated as:

$$d(i,j) = \sqrt{\sum_{m=1}^{48} [x_{i,m} - x_{j,m}]^2 + [y_{i,m} - y_{j,m}]^2 + [z_{i,m} - z_{j,m}]^2} \tag{3.39}$$

  All distances between corresponding trajectory points are summed up. Average distance between $i$-th trajectory and all other trajectories in cluster $A$ is given by:

$$a(i) = \sum_{j=1}^{N_A - 1} \frac{d(i,j)}{N_A} \tag{3.40}$$

  where $N_A$ represents different trajectories in cluster $A$ but not $i$.

- Consider new cluster $C$ which is different from $A$ containing another set of trajectories. The distance between trajectory $i$ belonging to cluster $A$ and trajectories belonging to cluster $C$ is given by:

$$d(i,C) = \frac{1}{N_C} \sum_{j=1}^{N_C} \sqrt{\sum_{m=1}^{48} [x_{i,m}^A - x_{j,m}^C]^2 + [y_{i,m}^A - y_{j,m}^C]^2 + [z_{i,m}^A - z_{j,m}^C]^2} \tag{3.41}$$

  where $A$ and $C$ are representing different clusters and $N_C$ is the number of trajectories in cluster $C$. The smallest distance is :

$$b\,(i) = \min_{C \neq A} \{d\,(i,C)\} \tag{3.42}$$

  The cluster $B$ for which this minimum is attained is called the *neighbor* of trajectory $i$. It is "the second best choice" for trajectory $i$: if cluster $A$ is discarded, cluster $B$ is the closest to $i$.

- The silhouette number $s\,(i)$, is obtained by combining $a\,(i)$ and $b\,(i)$:

$$s(i) = \frac{b\,(i) - a\,(i)}{max\{a\,(i),\, b\,(i)\}} \tag{3.43}$$

When $s(i) \approx 1$ ($a(i) \ll b(i)$) then the $i$-th trajectory is closest to cluster $A$. For $s(i) \approx -1$ ($a(i) \gg b(i)$) the distance to cluster $A$ is larger than to cluster $B$ and the $i$-th trajectory should be assigned to the $B$ cluster. At $s(i) \approx 0$ ($a(i) = b(i)$), the distances between the trajectory and clusters $A$ and $B$ are equal. The trajectory $i$ can be assigned to both clusters, i.e. it is a non-unique solution. Hence this case is not conclusive. For each trajectory $i$ the value $s(i)$ is defined and then these numbers are combined into a plot.

- Average silhouette value for all clusters ($N$) considered is:

$$\overline{s}(k) = \frac{1}{N} \sum_{i=1}^{N} \left(1 - \frac{a\,(i)}{b\,(i)}\right) \tag{3.44}$$

With the silhouette method, distances from trajectory $i$ to all the trajectories that belong to different clusters are compared. In this way the validation of the cluster to which $i$ is assigned is performed. The silhouette method correlates all considered clusters.

**RMSD method**

Additional verification of the chosen cluster number is done by using the RMSD method. Contrary to the silhouette method, the RMSD method focuses on distances within one cluster only. This gives an estimate of how well trajectories are assigned within one particular cluster. Assume that cluster $A$ has $N$ trajectories. Then the mean cluster trajectory is represented with matrix $\Gamma_A$ (3 coordinates and 48 points):

$$\Gamma_A = \begin{pmatrix} \overline{x}_1^A & \overline{y}_1^A & \overline{z}_1^A \\ \overline{x}_2^A & \overline{y}_2^A & \overline{z}_2^A \\ . & . & . \\ . & . & . \\ . & . & . \\ \overline{x}_{48}^A & \overline{y}_{48}^A & \overline{z}_{48}^A \end{pmatrix}$$

where

$$\begin{aligned} \overline{x}_i^A &= \frac{1}{N_a} \sum_{j=1}^{N_a} x_{i,\,j}^A \\ \overline{y}_i^A &= \frac{1}{N_a} \sum_{j=1}^{N_a} y_{i,\,j}^A \\ \overline{z}_i^A &= \frac{1}{N_a} \sum_{j=1}^{N_a} z_{i,\,j}^A \end{aligned} \tag{3.45}$$

are coordinates of the mean trajectory calculated between all trajectories in cluster $A$. The sum of all the squared distances of trajectories from mean cluster trajectory is:

$$\sigma_A = \frac{1}{N_A}\sqrt{\sum_{j=1}^{N_A}\sum_{i=1}^{48}[\,x_{i,j}^A - \overline{x}_i^A\,]^2 + [\,y_{i,j}^A - \overline{y}_i^A\,]^2 + [\,z_{i,j}^A - \overline{z}_i^A\,]^2}. \tag{3.46}$$

The total RMSD value for all clustering groups is:

$$\sigma = \sqrt{\sum_{A=1}^{K}\sigma_A^2}. \tag{3.47}$$

The relative percentage change of RMSD due to reduced number of clusters calculated from the highest number assumed to the smallest possible is:

$$\epsilon = \frac{\sigma_q - \sigma_{q+1}}{q+1}\,100\% \tag{3.48}$$

The lower $\epsilon$ value represents the set of clusters that is most suitable for grouping of trajectories. Lower values of $\epsilon$ indicate smaller distances within each cluster. The symbol $q$ denotes different groups of clusters.

## 3.7 The sea level pressure and geopotential height

The two day average **S**ea **L**evel **P**ressure **SLP** and **G**eo**p**otential **h**eight at 500 hPa pressure, **GPH500**, are used in analysis to describe the synoptic situation [3] before the day on which LIDAR measurements are performed. Reanalysis of SLP and GPH500 from a common project of the US National Centers for Environmental Prediction (NCEP) and the National Center for Atmospheric Research (NCAR) [60] were used as observed predictor values. Horizontal resolution of gridded SLP reanalysis is $2.5^o$x$2.5^o$ and $GPH$ is $5.5^o$x$5.5^o$. [4].
The observed and modeled SLP and GPH500 were interpolated in a common grid of $2.5^o$x$2.5^o$ by a simple bi-linear interpolation method [61]. Modeled SLP and GPH500 values were obtained from the results of simulations obtained inside the **G**eneral **C**circulation **M**odel **GCM** project.

[3] A surface weather observation, made at periodic times (usually at three-hourly and six-hourly), of sky cover, state of the sky, cloud height, atmospheric pressure reduced to sea level, temperature, dewpoint, wind speed and direction, amount of precipitation, hydrometeors, etc.

[4] Given from: http://dss.ucar.edu/datasets/ds335.0/docs/.

# 4 Results and discussion

LIDAR measurements can in principle provide us with data on the aerosol concentration, types and sizes in the atmosphere. The combined information can further be used to enhance and improve the accuracy of the air mass models, especially if LIDAR observatories are interconnected into a network covering a large geographic area, as for instance EARLINET. However, the LIDAR at Otlica is a simple one and can not yet provide all these kinds of information. Here, the analysis of single day measurements represented by different LIDAR cases, provides information about aerosol presence in the atmosphere, and extinction and back-scattering of laser light occurring due to interaction by molecules and aerosols, but cannot provide information about the size of the particles, their concentration in the atmosphere and type. The extinction to back-scattering ratio used for study of each case, can indicate the type of detected aerosols. Since, at all altitudes constant value of this LIDAR ratio is used, information about aerosol type present is not very precise. At this stage of the experimental setup we can however use the air mass models, their predictions of the air mass history and typical directions of air flow reaching Slovenia, to estimate the atmospheric properties (i.e. type, vertical distribution of aerosols) above the Otlica observatory at a given time. For a number of such specific situations, LIDAR measurements were made and are presented as case studies later in this chapter.
In order to obtain information about typical directions of airflow reaching Slovenia at different altitudes, clustering of air trajectories is deployed. In this way all air trajectories of similar history are assigned to different groups. Since clustering routine assumes the number of clusters, validation of the optimal number of clusters need to be considered.

## 4.1 Selection of the optimal number of clusters

Evaluation of cluster analysis results, done using silhouette and RMSD methods, led to an identification of the optimal number of classes. Clusters represent distinct groups (classes) with trajectory members that have similar histories in terms of their direction of approach and speed of passage over different surfaces.
Silhouette values determine how well clusters are distinct from each other. They also evaluate how well trajectories are assigned to separate groups. Higher silhouette values indicate that clustering is better and that the clusters are distinctive enough. A percentage change in in RMSD values between two neighboring cases signifies the optimum number of clusters to be retained in analysis. It shows how well the trajectories are assigned inside each cluster. A low RMSD value indicates that there are small distances between trajectories inside each cluster. Analysis of silhouette and RMSD values provides information about an optimal number of classes when their member trajectories are distinctive enough and that trajectories are grouped in the best way with the respect to their direction of approach.

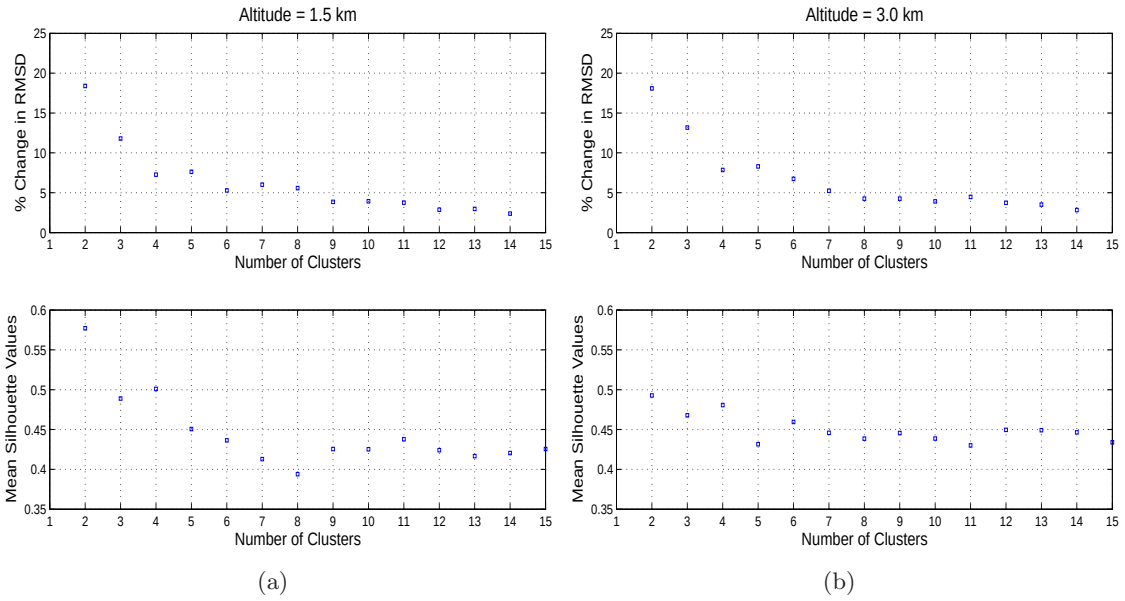


(a) (b)

**Figure 4.1:** Silhouette and RMSD plots for the selection of different backward-trajectory clusters for heights: (a) 1500 m and (b) 3000 m.

The K - means clustering method is applied to the air trajectories determined by HYSPLIT model. The trajectories are taken over 48-hour period. Grouping is performed for different number of clusters (from 2 to 16). Calculated silhouette and RMSD values at different heights are presented in Figures 4.1 and 4.2. The optimal number of clusters is determined by: highest silhouette value, low RMSD value and highest RMSD difference between neighboring clustering cases. The highest silhouette value has a first grouping into two clusters. However, this case is not taken as the optimal number. It is highly improbable that sets of trajectories coming from different directions can be assigned well to just two groups. The data contains longer (fast winds) and shorter (slow winds) trajectories. The probable scenario is then that the clustering algorithm recognizes one class containing longer trajectories, and another one containing the bulk of the short trajectories. This would produce classes gathering trajectories that arrive from different directions without providing information about typical directions of the air arriving in Slovenia. If we do not consider grouping into 2 clusters then the grouping into four clusters has the highest silhouette. This is also true for silhouette values at every height. The value indicates that the grouping is performed well.

From Figures 4.1 and 4.2 sudden breaks between RMSD values are evident at various stages of the clustering process. These are interpreted as the merging of clusters of trajectories which are significantly different in terms of the wind direction and speed which they represent. A large percentage change in RMSD when reducing the number of clusters from four to three is visible. This trend is the same at all heights. The case of four clusters has smaller RMSD value.

The local maximums and minimums among the silhouette and RMSD values in other cases are present. They are characteristics of each separate height. Hence they do not indicate some general tendencies, which is the reason that they were not chosen. Clustering into four groups fulfills all requirements for a good clustering. Four clusters are therefore retained to

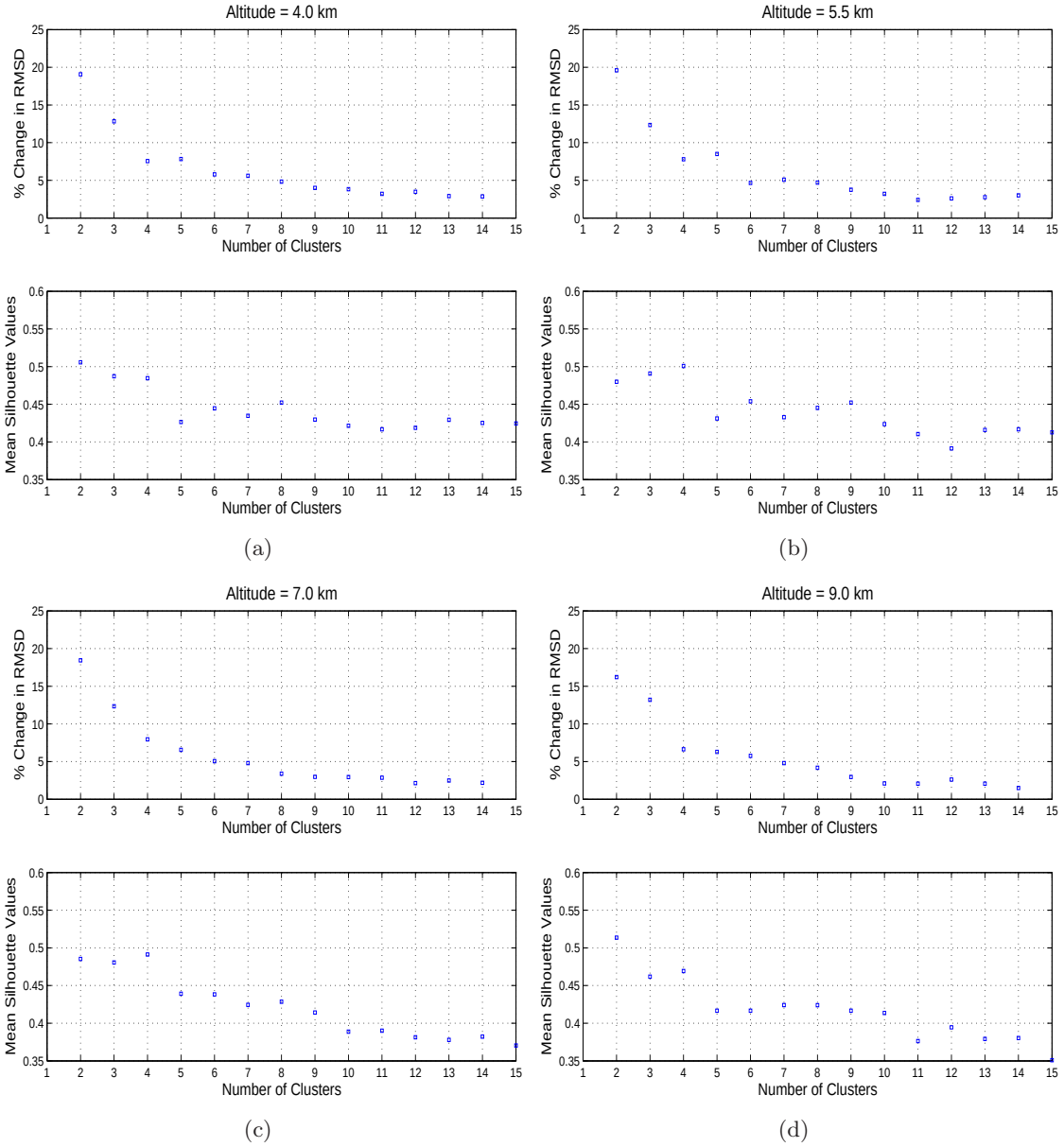


**Figure 4.2:** Silhouette and RMSD plots for the selection of different backward-trajectory clusters for heights: (a) 4000 m, (b) 5500 m, (c) 7000 m and (d) 9000 m.

best describe significantly different directions of air flow.

## 4.2 Cluster analysis of back-trajectories

Once optimum number of clusters is identified, the success of the algorithm is confirmed by plotting the separate trajectory clusters (Figures 4.3 and 4.4). Trajectories shown in different colors refer to the different seasons during the year. Black, green, red and magenta trajectories represent Winter, Spring, Summer and Autumn days respectively.

The classes determined are the following:

- **C**entral **c**lass gathering trajectories from different directions (**C**): Arrival of slow and stable air masses from various directions are typical for this class. The main characteristics of member trajectories are small distances per time unit and big dispersion in relation to different direction of arrival [30]. Due to these properties, it is difficult to define general characteristics for this class.

- **S**outh**w**est-**W**est class (**SW-W**): Arrival of slow tropic masses from south-west and west is typical for this class. These include continental tropical air masses (cT) that mostly come to Slovenia from the South-West direction and maritime tropical air masses (mT) that come from the West [30]. The origin of cT air masses during Winter is North Africa. These air masses begin very dry, but while traveling across the Mediterranean Sea they receive additional water vapor. Lower layers of cT air trajectories cool above cold continents and become very stable. During the summer cT air masses bring clear and warm weather with a big difference between night and day time temperatures. Maritime tropical masses develop over the North Atlantic Ocean. In the Winter these air masses are warm and humid and their passing over a cold continent usually results in formation of fog and light rain. During the Summer mT air masses bring sultry and warm weather. Because of their lability, convective clouds with storms are common. During Winter and Summer, tropical air masses are characterized by low visibility [30]. Typical representatives of this class are the cT air masses that bring Sahara desert dust into the region of Slovenia.

- **N**orth**w**est-**W**est class (**NW-W**): Fast, polar maritime air masses (mP) that develop over the Northern and Northwestern part of the Atlantic Ocean characterize this class. Due to the rapid movement these air masses retain most of the characteristics obtained at their source. In Winter, air masses formed above the ocean are relatively warm and labile. When such air masses arrive over a cold continent they cool, which leads to the formation of fog and precipitation. During the Summer, mP air masses are relatively cold and they warm over the continent. Because of the large humidity content, these air masses cause appearance of convective clouds and storms [30].

- **N**orthern class (**N**): Fast polar-continental air masses (cP) developing above the North-region of Europe are characteristic for this class. Since they form above cold land these masses are very dry and stable. If they are passing over warm land they warm up and become more labile. Nevertheless, North air masses in general do not bring clouds, since they are not humid. In both, Summer and Winter, cP air masses are relatively cold and dry [30].

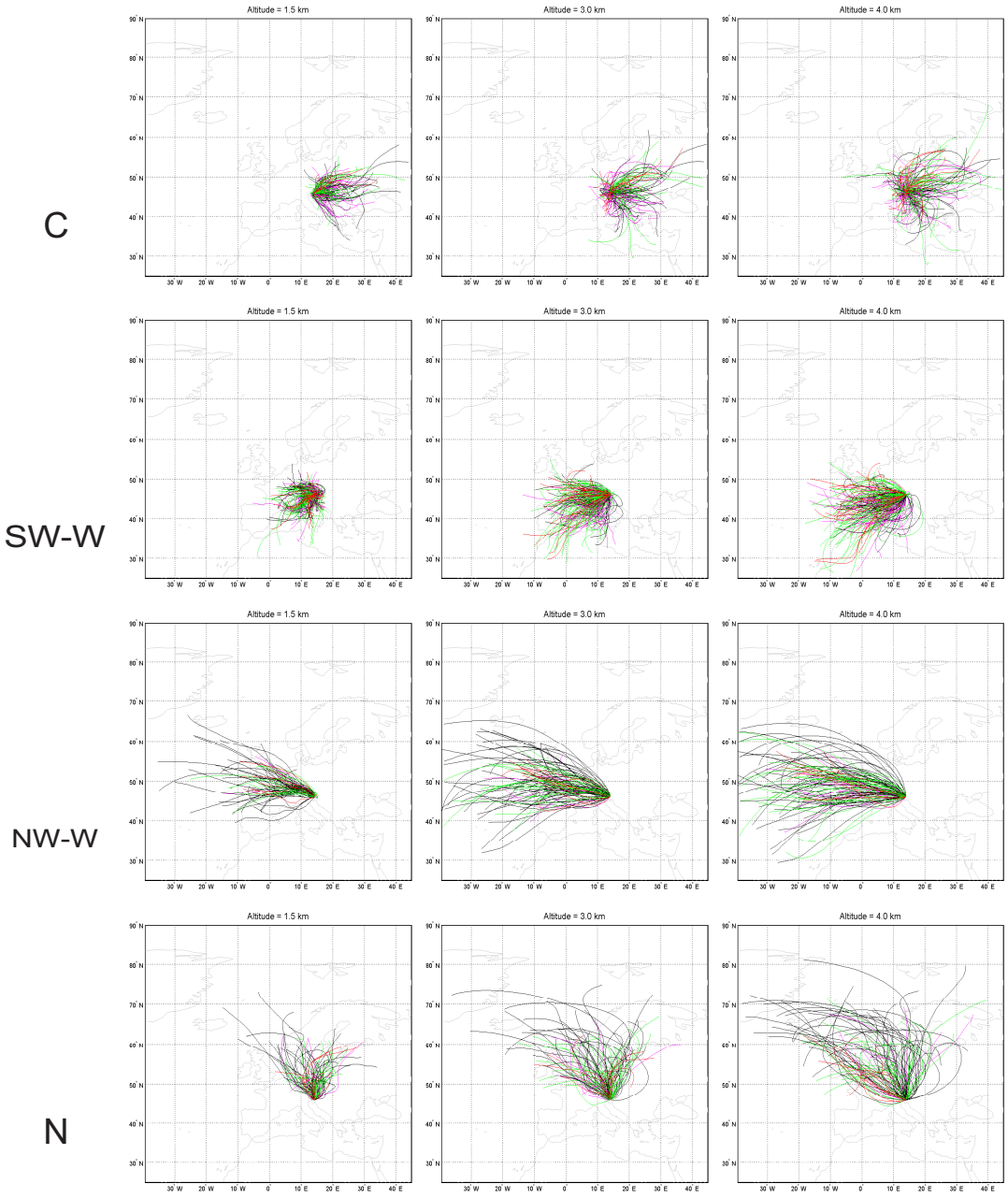


**Figure 4.3:** Results of cluster analysis for 48 hour trajectories that describe the arrival of air above Otlica region for January 2005- September 2006: rows present 4 different classes (C, SW-W, NW-W and N) and columns three heights 1.5 km, 3 km and 4 km, refer to the annual seasons: spring, summer, autumn and winter.

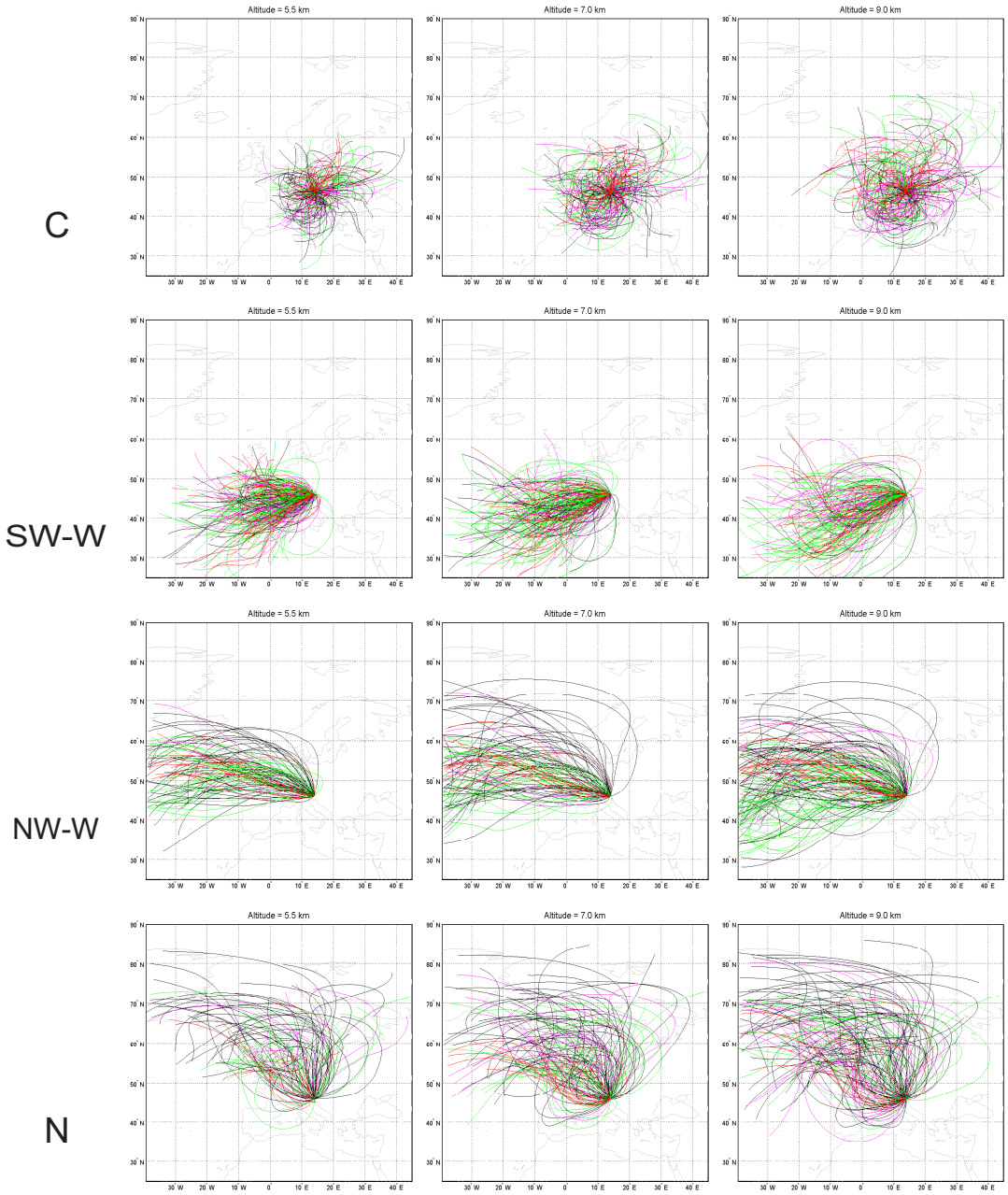


**Figure 4.4:** Results of cluster analysis for 48 hour trajectories that describe the arrival of air above Otlica region for January 2005- September 2006: rows present 4 different classes (C, SW-W, NW-W and N) and columns three heights 5.5 km, 7 km and 9 km refer to the annual seasons: spring, summer, autumn and winter.

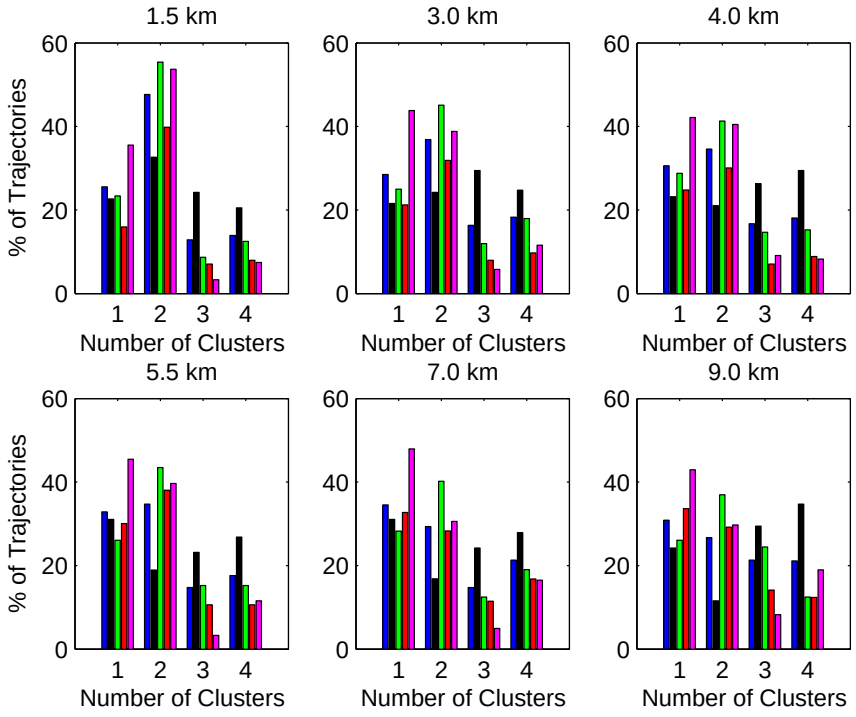


**Figure 4.5:** Relative frequency of trajectories assigned to different clusters with respect to total number of trajectories (blue bar), and of season trajectories at particular heights with respect to the total number of season trajectories: spring, summer, autumn and winter.

All classes are composed from trajectories belonging to different seasons. Statistical analysis of class members is performed calculating relative frequencies of trajectories (Figure 4.5). Relative frequency is determined as the ratio of trajectories assigned to different clusters relative to the total number of trajectories and is presented by the blue bar. Relative frequencies of seasonal trajectories are calculated as ratios of seasonal trajectories assigned to different clusters relative to the total number of seasonal trajectories. They are given in different colors, green for spring, red for summer, magenta for autumn and black for winter (Figure 4.5). Numerical values of relative frequencies are given in Table 4.1. The relative frequency values are spread between 20% and 40%, except at the lowest height. As a criteria for the "majority of the trajectories" threshold of 33% is used. Analysis of the relative frequencies showed that most of the air trajectories are assigned to the SW-W (47% at 1.5 $km$, 37% at 3 $km$, 35% at 4 $km$ and 5.5 $km$, 30% at 7 $km$ and 27% at 9 $km$) and C (25% at 1.5 $km$, 29% at 3 $km$, 30% at 4 $km$, 33% at 5.5 $km$, 35% at 7 $km$ and 31% at 9 $km$) classes. It is noticable that total relative frequencies for the SW-W class are decreasing with height, while with the C class they increase. This is probably governed by the topography. Alternately, it could be that this occurs due to a clustering procedure. At higher altitudes SW-W trajectories are significantly longer and the procedure "decides" to assign all of the shorter trajectories to the C class. The algorithm simply finds more similarities between trajectories belonging to the C class and short SW-W trajectories, than short and long trajectories of SW-W class. Classes N and NW-W are characterized by a lower value of relative frequencies that are similar for every height ($\approx 20\%$).

**Table 4.1:** Relative frequency of trajectories assigned to different clusters with respect to total number of trajectories (all) and of season trajectories at particular heights with respect to the total number of season trajectories. Relative frequencies are expressed in [%].

| | height = 1.5 km | | | | | height = 3.0 km | | | | |
|---|---|---|---|---|---|---|---|---|---|---|
| | all | wint | spr | summ | aut | all | wint | spr | summ | aut |
| C | **25** | 23 | 24 | 16 | 37 | **29** | 21 | 25 | 21 | 44 |
| SW-W | **47** | 32 | 55 | 40 | 54 | **37** | 24 | 45 | 32 | 39 |
| NW-W | **13** | 24 | 9 | 7 | 3 | **16** | 30 | 12 | 8 | 5 |
| N | **15** | 20 | 12 | 7 | 7 | **18** | 25 | 18 | 10 | 11 |
| | height = 4 km | | | | | height = 5.5 km | | | | |
| | all | wint | spr | summ | aut | all | wint | spr | summ | aut |
| C | **30** | 23 | 29 | 25 | 42 | **33** | 31 | 26 | 30 | 46 |
| SW-W | **35** | 21 | 41 | 30 | 40 | **35** | 19 | 43 | 38 | 40 |
| NW-W | **16** | 26 | 15 | 7 | 9 | **15** | 23 | 15 | 11 | 4 |
| N | **19** | 30 | 15 | 9 | 8 | **17** | 27 | 15 | 11 | 12 |
| | height = 7 km | | | | | height = 9.0 km | | | | |
| | all | wint | spr | summ | aut | all | wint | spr | summ | aut |
| C | **35** | 31 | 28 | 33 | 48 | **31** | 24 | 26 | 34 | 43 |
| SW-W | **30** | 17 | 40 | 28 | 31 | **27** | 11 | 37 | 29 | 30 |
| NW-W | **14** | 24 | 13 | 11 | 5 | **21** | 30 | 24 | 14 | 8 |
| N | **21** | 28 | 19 | 17 | 17 | **21** | 35 | 13 | 12 | 19 |

Relative trajectory frequencies for all four classes are similar when considering different heights of air arrival, with an exception of 1.5 km altitude. Seasonal relative frequencies show that the majority of spring trajectories are representatives of the SW-W class (an average of 45% at all heights). Also, summer is characterized by trajectories that describe the arrival of air mainly from Southwest-West direction ($\approx$ 40%). Very slow trajectories belonging to class C are also common for summer ($\approx$ 30%). Most of the trajectories denoted by the arrival of Autumn air above the region of Slovenia are assigned to the SW-W class ($\approx$ 40%) and C class ($\approx$ 45%). Winter is generally characterized by lower relative frequencies indicating a lower number of trajectories. They are equally frequent in every class (from $\approx$ 20% to $\approx$ 30%).

## 4.3 LIDAR aerosol sensing in different synoptic situations

This section presents LIDAR measurements. Single day LIDAR measurement, represented by one run, is analyzed using the Fernald method. Obtained LIDAR signals have different lengths depending on the weather conditions and atmospheric properties. In the cases of clear atmosphere and almost no aerosol presence, the measured range reaches up to 35 km, as shown in Figure 3.11. As our goal was to detect the tropospheric aerosols, all measurements are presented only up to 15 km.

Amount of back-scattered light $P$ from different altitudes, given in meters, and the $S$ function are shown for every measured case. Until reaching the height of about 1 km above the ground, where the laser beam enters the receiver's field of view, the measured signal is not

representative. Total, molecular and aerosol back-scattering and extinction coefficients ($\beta$, $\alpha$, $\beta_m$, $\alpha_m$, $\beta_a$ and $\alpha_a$, respectively) at different heights, are deployed. The extinction coefficients are given in units $m^{-1}$ and back-scattering coefficients in $m^{-1}\,sr^{-1}$. The optical depth ($\tau$) is retrieved via Bouguer-Lambert law (see Equation (3.7)) and it gives measure of atmospheric opaqueness to incident radiation. It is calculated using the total extinction coefficient i.e $\alpha = \alpha_a + \alpha_m$.
The extinction to back-scattering ratio $R = \alpha_a/\beta_a$ was estimated for every single LIDAR case and treated as a constant with height. The LIDAR ratio value for which aerosol extinction and back-scattering coefficients were tending to zero at stratospheric height (around 15 km above the ground) are used. Values of LIDAR ratio up to 30 are characteristic in the presence of smaller particles in the atmosphere. In this case, some maritime type aerosols are usually present in the air [69]. In the case of continental aerosol presence, the LIDAR ratio has values higher than 40 [69]. For the desert dust aerosols the LIDAR ratio has values from 40 to 50. All determined coefficients depend on wavelength, and in this study they refer to the UV light of 355 nm.
Molecular extinction and back-scattering coefficients are determined using the radiosonde data [51] and US Standard Atmosphere 1976 [50]. The radiosonde data are taken from the closest place where this kind of data taking is applied, called Udine. Since Udine is placed at 100 m sea level, the reference height for molecular coefficients calculation is taken to be 900 m above the sea level and it corresponds to the Otlica location.
The 72 hour long history of air masses represented by backward trajectories, was used to determine types of detected aerosols. The trajectories are calculated starting from 0 : 00 UTC, which is approximately the time of LIDAR measurement, and go 72 hours back with a step of 6 hours. The maps of SLP and GPH500 are presented. The typical height of 500 hPa layer is around 5.5 km. Maps of SLP and GPH500 are used to describe a synoptic situation two days before the day on which the measurement was made.
The DREAM model predicts concentration of desert dust aerosols above the Otlica and it is calculated from the sea level. The HYSPLIT model also starts computation from the sea level. Therefore, for example, 1 km on the plots of LIDAR cases is equivalent to about 2 km on plots of DREAM model and HYSPLIT model results and radiosonde data.
As all measurements are taken during the night, the measurement dates refer to the day starting at midnight.

### 4.3.1 Case 1: June 24, 2005.

Figure 4.6 shows the air trajectories that describe air arriving above the Trnovski gozd region at 0:00 UTC on the $24^{th}$ of June, 2005. Short trajectory at an altitude 1.5 km is characterized with slow and weak air flow that passes above the Mediterranean region very close to the Slovenian coast. This air trajectory is representative of the C class. At other altitudes, air trajectories are coming from the Northwestern part of the North Atlantic ocean and are representatives of NW-W class.
Weather conditions for days before taking a measurement indicate a presence of a high SLP field above middle Europe. Northwestern winds brought humid air to the Slovenia region. During the $23^{rd}$ of June the sky was clear in the morning, but during the day was becoming cloudy [68].
Maps of SLP and GPH500 are shown in Figure 4.7.a and 4.7.b. Constant high SLP field can be seen across the region of Slovenia and surrounding countries. The constant SPL indicated

the slow winds, justifying the model obtained short air trajectoty at 1.5 km. A strong SLP gradient is evident at the latitudes between $50^oN$ and $60^oN$ indicating an arrival of air masses

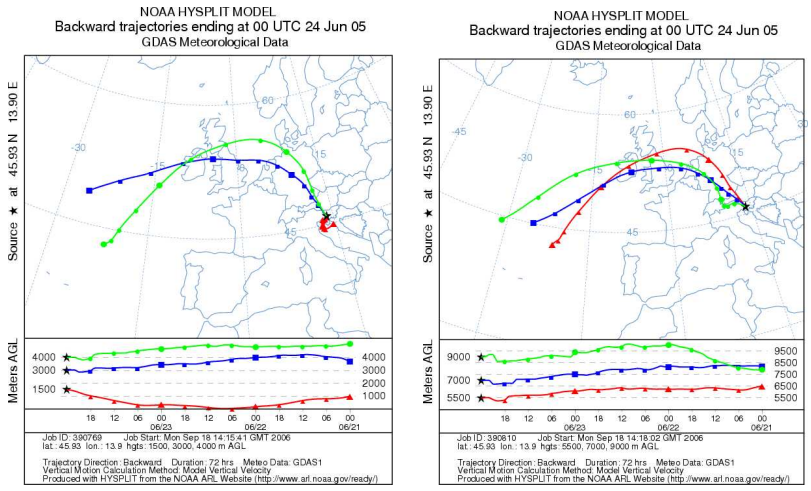


(a) (b)

**Figure 4.6:** Backward trajectories denoting the arrival of air at the Otlica on the June $24^{th}$, 2005 at heights: (a) 1500 m, 3000 m and 4000 m and (b) 5500 m, 7000 m and 9000 m.

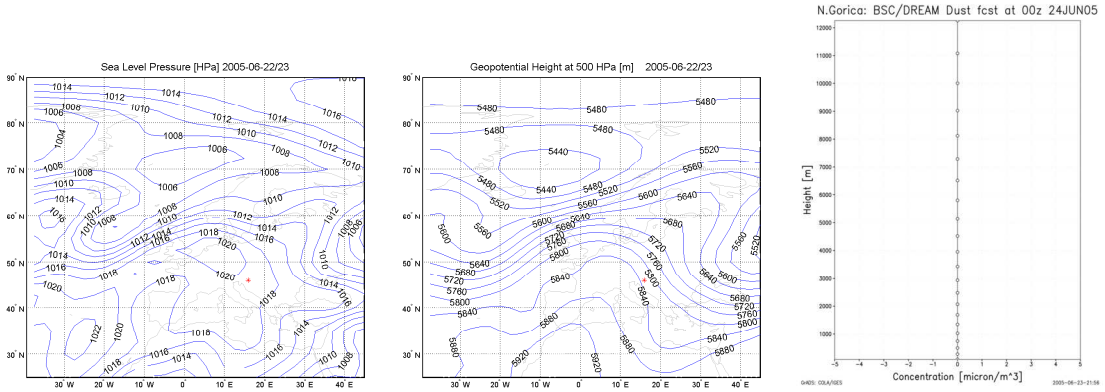


(a) (b) (c)

**Figure 4.7:** Average synoptic pattern of sea-level pressure (a) and 500 hPa geopotential height (b) for $22^{th}$ and $23^{rd}$ of June 2005, together with Saharan dust concentration above Otlica (c) predicted by the DREAM model for $24^{th}$ of June 2005.

from the Northwestern part of the North Atlantic Ocean. A similar direction of air flow that arrives above Otlica at heights around 5.5 km above sea level can also be seen from the GPH500 pattern.

Presence of dust particles from the Saharan desert is not expected in the case of NW-W air masses. Also, to that the DREAM model did not predict the presence of Saharan dust above Otlica for the time of this day measurement (Figure 4.7.c).

The LIDAR run from the $24^{th}$ June 2005 contains 120 events. Vertical profiles obtained from LIDAR measurements by the Fernald method are presented in Figure 4.10. Both signal $P$

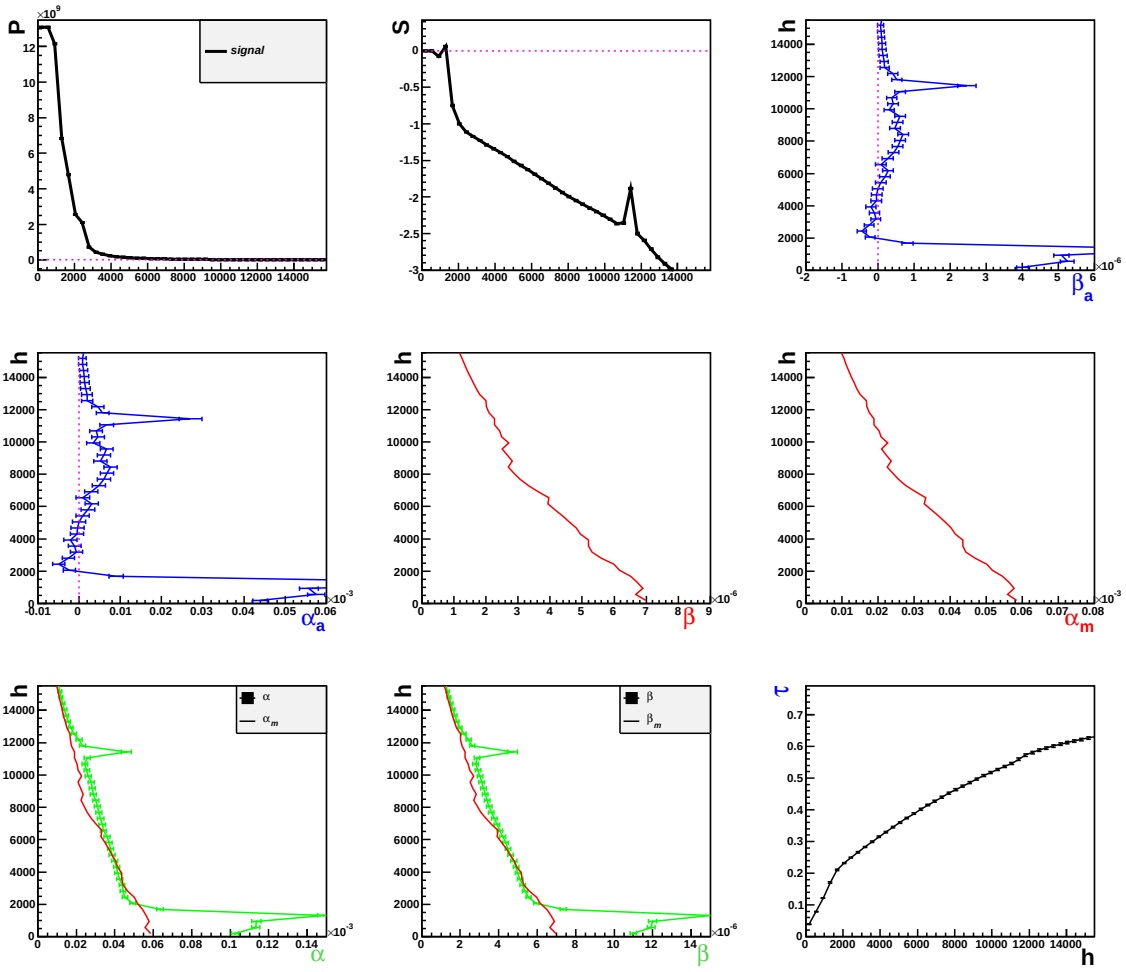


**Figure 4.8:** Vertical profiles of the original LIDAR signal ($P$), $S$-function and different atmospheric optical properties $\beta_a$, $\alpha_a$, $\alpha_m$, $\beta_m$, $\alpha$, $\beta$ and $\tau$ based on Run 14, taken on June $24^{th}$ 2005.

and $S$ function indicate the presence of low cloud at around 1 km above the ground (approximately 2 km above sea level), and a high cirrus cloud at about 11 km. The lower cloud is probably a result of humid air brought from the Mediterranean region in the lowest layer of the atmosphere (see the 1.5 km trajectory in Figure 4.6).

Due to the strong scattering of the laser beam in the lower cloud, the detected back-scattered light causes a saturation of PMT and proper readout of the signal was not possible up to about 3 km. Because of saturation, undershooting occurs, i.e. the signal has values below zero (due to saturation a read out is not possible for some time period, the drop of voltage occurs on the PMT and the electronic circuits are reacting in such a way that the signal becomes negative [49]) and consequently coefficient values are negative. The extinction to back-scattering ratio used is 15. Using this ratio, aerosol extinction and back-scattering coefficient at altitudes of stratosphere approach zero, which is supposed to be the case. For radiation wavelength of 355 nm ratio, $R$, that has values between 15 and 30 indicates a presence of maritime aerosols [69]. Since the air mass present above Otlica represents maritime air mass, it is probable that

a small amount of aerosols detected by the LIDAR are of maritime origin. Molecular profiles of extinction and scattering coefficients (latter mentioned just as molecular profiles) show an exponential decrease and are calculated using US Standard Atmosphere 1976 and radiosonde data taken from the NOAA site [2].
Peaks, transparently visible in aerosol extinction and scattering profiles, correspond to stronger scattering of laser light from clouds. Integration of the attenuation, $\alpha$, results in a vertical optical depth, $\tau$. Absolute error of $\tau$ increases with height. Up to a height of 15 km the cumulative value of an optical depth reaches about $0.6 \pm 0.1$. This value expresses the factor by which light is attenuated up to this altitude, which is equal to $e^{-0.6}$.

### 4.3.2 Case 2: June 25, 2005.

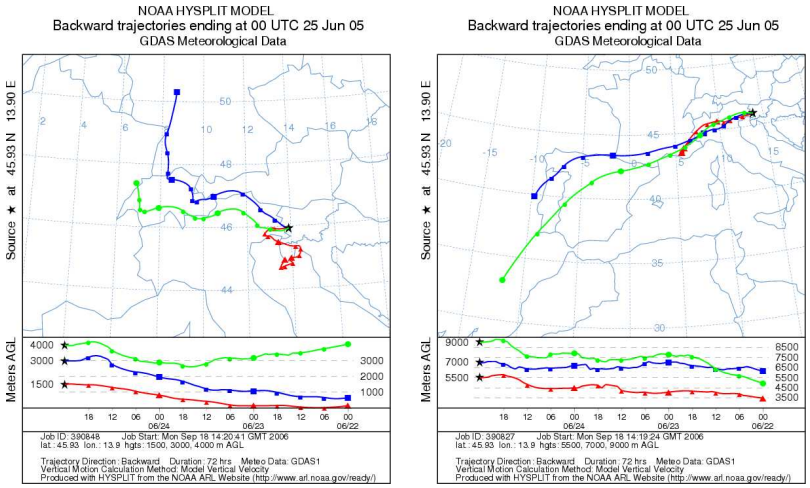


(a) (b)

**Figure 4.9:** Backward trajectories denoting the arrival of air at the Otlica on the $25^{th}$ of June 2005 at heights: (a) 1500 m, 3000 m and 4000 m and (b) 5500 m, 7000 m and 9000 m.

Trajectories shown in Figure 4.9 represent the movement of air that reaches the Trnovski gozd region at 0:00 UTC on the $25^{th}$ of June, 2005. As in the previous case, the trajectory at a height of 1.5 km passes over the Northern Mediterranean region close to the Slovenian coast and is characterized by a very slow and weak air flow. Trajectories arriving at altitudes of 3 km and 4 km pass over Germany and Switzerland. These air trajectories are very short, indicating weak winds and stable weather, making them representatives of class C. Air denoted by the trajectories at 5.5 km, 7 km and 9 km, arrives to the Otlica region passing over the Southwestern and Western part of North Atlantic Ocean. Trajectory at 5.5 km is assigned to the class C. Although the trajectory at 7 km is similar to the trajectory at 9 km, clustering procedure assigned it to class C, while trajectory at 9 km is assigned to class SW-W.
On the $25^{th}$ of June a high SLP field was present above the middle and western part of Europe. During the day the sky was partially clear [68].
The average SLP field for two days is presented in Figure 4.10.a. A constant and high SLP field can be seen above Slovenia, justifying the slow and weak air flow at lower altitudes (below 4 km). The GPH500 map is given in Figure 4.10.b. A high density of isolines (between

[2]Data taken from the radiosonde measurements at Udine [51] and USA standard atmosphere 1976 [50].

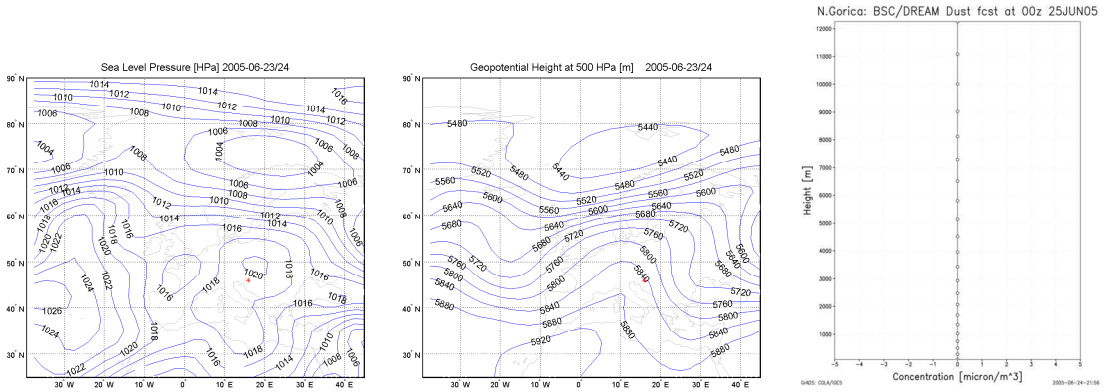


**Figure 4.10:** Average synoptic pattern of sea-level pressure (a) and 500 hPa geopotential height (b) for $23^{rd}$ and $24^{th}$ of June 2005, together with Saharan dust concentration above Otlica (c) predicted by DREAM model for $25^{th}$ of June 2005.

$40^oN$ and $60^oN$) indicate a strong horizontal pressure gradient that results in strong winds blowing from Southwestern-Western regions. This gradient governs the arrival of air from this direction to the region of Slovenia in the upper troposphere.

The highest altitude trajectory is representatives of the SW-W class, but does not pass over Northern Africa region in this time period (72 hours). No presence of Saharan dust aerosols was estimated by the DREAM model for 0:00 UTC on the $25^{th}$ of June (Figure 4.10.c).

The LIDAR data run taken on June $25^{th}$ consists of 120 events (Figure 4.11). The lower cloud detected by the LIDAR is probably a result of the arrival of humid air from the Adriatic region, indicated by the trajectory at 1.5 km above the sea level. The cloud is clearly visible from the signal $P$ and $S$ function. The negative coefficient values are caused by an undershooting effect. There is one other cloud present at 11 km above the ground.

The aerosol extinction to back-scattering ratio used in this case analysis is 15. This value is characteristic of maritime aerosols. The aerosol extinction and back-scattering coefficients differ from zero. At the cloud altitudes aerosol coefficients are significantly higher due to the increased absorption and scattering of laser light and negative above the clouds due to the undershooting effect. In this 72 hour period the air trajectories, except the highest altitude trajectory, passed over the continental regions. The air, denoted by these air trajectories assigned to the class C, arrives from different directions and a prevailing type of aerosol is not possible to determine, even-though the LIDAR ratio value indicates the presence of maritime aerosols. Determination of aerosol types, only based on the LIDAR ratio value is not precise. Using simple LIDAR systems without additional information (e.g. Sun Photometer), introduces assumptions that are included in the data analysis. At altitude of 9 km above the sea level air passes over the Southwestern part of the North Atlantic Ocean making it possible that the aerosols are of maritime or desert aerosols. However, from LIDAR ratio and DREAM predictions presence of Saharan dust should not be expected. Based on the properties of the class to which majority of the trajectories are assigned and LIDAR ratio used, it is not conclusive which type of aerosols is present overall. The molecular and total aerosol extinction and back-scattering profiles are not matching. Values of this difference could also be influenced by the approximate calculation of molecular coefficients. Due to all

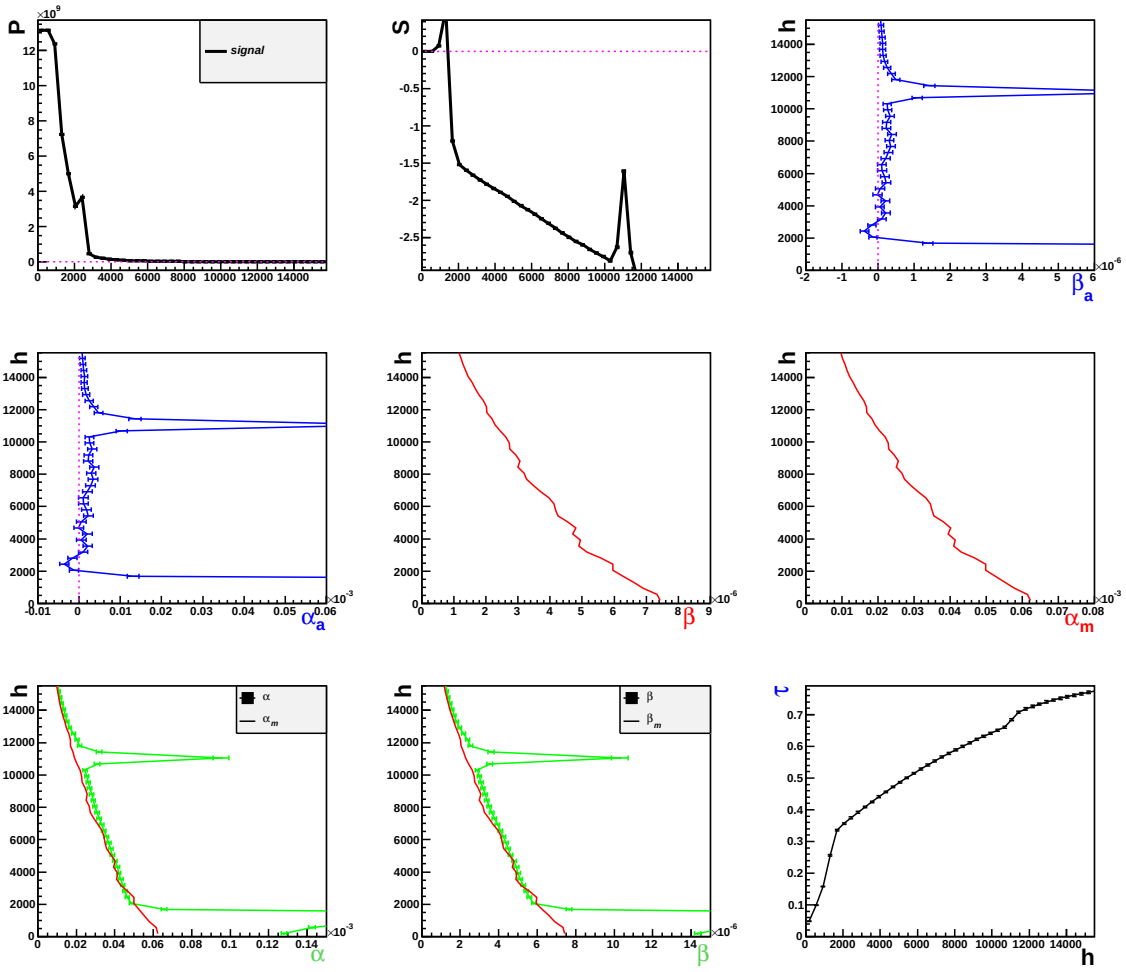


**Figure 4.11:** Vertical profiles of original LIDAR signal ($P$), $S$-function and different atmospheric optical properties $\beta_a$, $\alpha_a$, $\alpha_m$, $\beta_m$, $\alpha$, $\beta$ and $\tau$ based on Run 15, taken on June $25^{th}$ 2005).

of above mentioned reasons, there is no transparent proof about the type of aerosols present. The optical depth plot exhibits higher values than in the previous case. Values are higher due to the back-scattering and extinction from maritime aerosols caused mostly by cloud presence. Up to a height of 15 km above the ground, the cumulative value of an optical depth reaches approximately $0.8 \pm 0.2$. This means that the laser beam, up to this height, is attenuated by a factor of $e^{-0.8}$. Although aerososl coefficients are noth so high, higher value of $\tau$ is present due to the clouds.

### 4.3.3 Case 3: June 17, 2006

The trajectories that describe the movement and arrival of air above the Trnovski gozd region at 0:00 UTC on June $17^{th}$ 2006 are shown in Figure 4.12. Except for the lowest trajectory which is short and passes over the North Mediterranean region, the trajectories at 3 km and 4 km indicate the arrival of the continental tropical air mass. The higher three trajectories

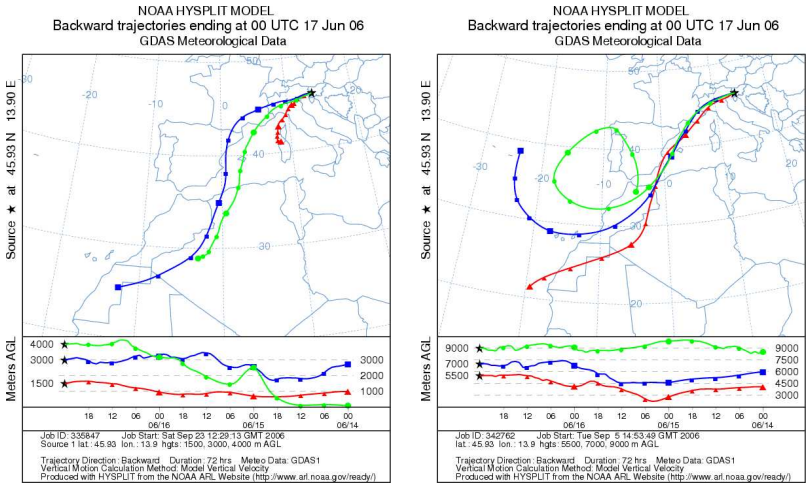


(a) (b)

**Figure 4.12:** Backward trajectories denoting the arrival of air at the Otlica on the June $17^{th}$ 2006, at heights: (a) 1500 m, 3000 m and 4000 m and (b) 5500 m, 7000 m and 9000 m.

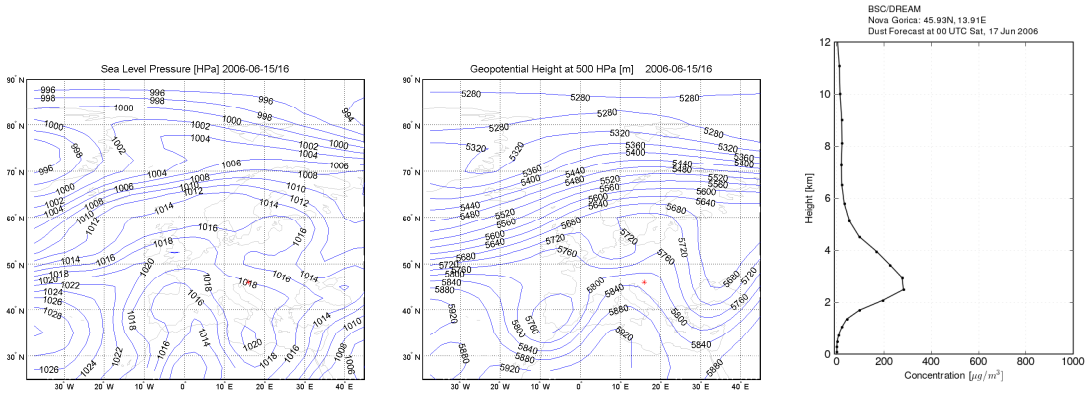


(a) (b) (c)

**Figure 4.13:** Average synoptic pattern of sea-level pressure (a) and 500 hPa geopotential height (b) for $15^{th}$ and $16^{th}$ of June 2006, together with Saharan dust concentration above Otlica (c) predicted by DREAM model for June $17^{th}$, 2006.

(Figure 4.12.b) pass above the southwestern part of the North Atlantic Ocean. The trajectory at 1.5 km belongs to the C class and all other trajectories are representatives of the SW-W class.

Over the larger part of Europe, on the $16^{th}$ and $17^{th}$ of June, a constant air pressure field was present. At higher altitudes we had an inflow of warm and more humid air [68].

A map of the SLP is shown in Figure 4.13.a. A low SLP field at the Northwestern part of the North Atlantic Ocean, above Greenland, and a high SLP fields at the Southwestern part of the North Atlantic Ocean above Cape Verde and the Canary Islands, and also at the South of Italy, are present. In the region of North Africa (Algeria and Libya) low SLP field is also visible. The air stream from the South, along the isobar line present between field South

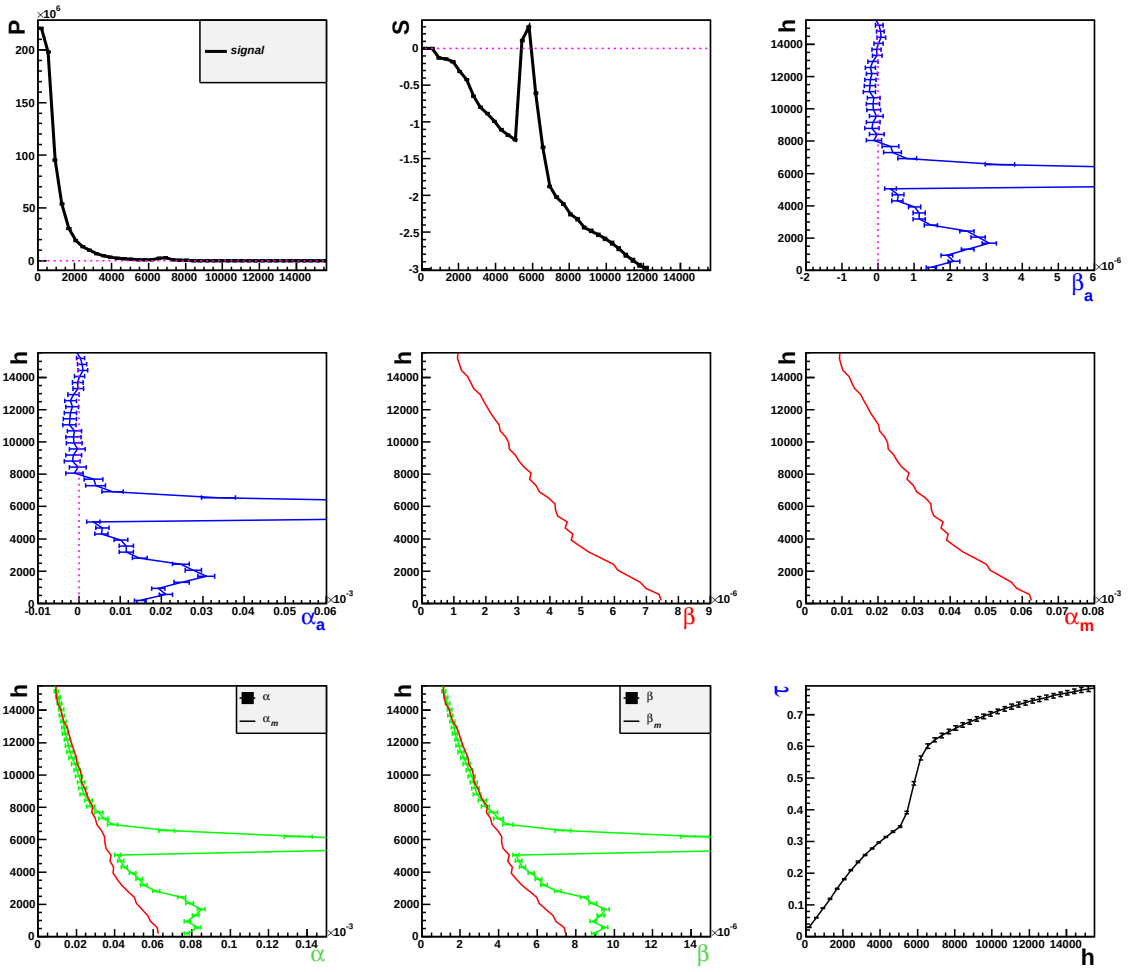


**Figure 4.14:** Vertical profiles of original LIDAR signal ($P$), $S$-function and different atmospheric optical properties $\beta_a$, $\alpha_a$, $\alpha_m$, $\beta_m$, $\alpha$, $\beta$ and $\tau$ based on Run 113, taken on June $17^{th}$, 2006.

of Italy and one above Algeria, reaches Slovenia. The GPH500 map is presented in Figure 4.13.b. A strong GPH500 gradient field is present at the North ($45^o$N-$80^o$N). The main air stream spreads from the Northwest to the Northeast. The stream important for the airflow to Slovenia, moves from north of the North Atlantic towards Northern Africa and then turns passing the Mediterranean region, approaching Slovenia from the southwest direction.
The DREAM model predicted an episode of Saharan dust above Slovenia on the $17^{th}$ of June, 2006. The profile estimated by this model for 0:00 UTC is shown in Figure 4.13.c. From the distribution we can see an estimated presence of Saharan dust aerosols between 1.5 and 6 km above sea level with a maximum concentration at about 3 km (2 km above the ground).
The LIDAR run contained 150 events. From the signal and $S$ function given in Figure 4.14, a pronounced peak at 9 km above the ground indicating the cloud is visible. Cloud formation is probably caused by the combination of warm and humid air brought from Southwest and available condensation nuclei (i.e Saharan dust). Aerosol coefficients differ from zero in the region up to about 4 km with the peak around 2 km above the ground, when the values in

the region of the cloud are not considered. These aerosols are possibly brought with the air arriving at lower altitudes from the Sahara desert (Figure 4.12). Digression in this range is in good correspondence with the DREAM model predictions indicating the presence of desert dust aerosols.

The LIDAR extinction to back-scattering ratio used in this case is 35. This is close to the value of 40, usually considered to account in the case of desert dust aerosols [69]. Above the cloud aerosol coefficients are equal to zero indicating absence of aerosols. Due to the LIDAR ratio used as well as the air mass history and DREAM model predictions we can state presence of Saharan dust at lower altitudes. Optical depth values show higher opaqueness of the atmosphere then in previous cases. Up to approximately 8 km above the ground, the optical depth reaches a cumulative value of about $0.8 \pm 0.2$. While a stronger opacity of atmosphere is present due to the desert dust aerosols, it is mostly due to the large scattering and absorption from the cloud.

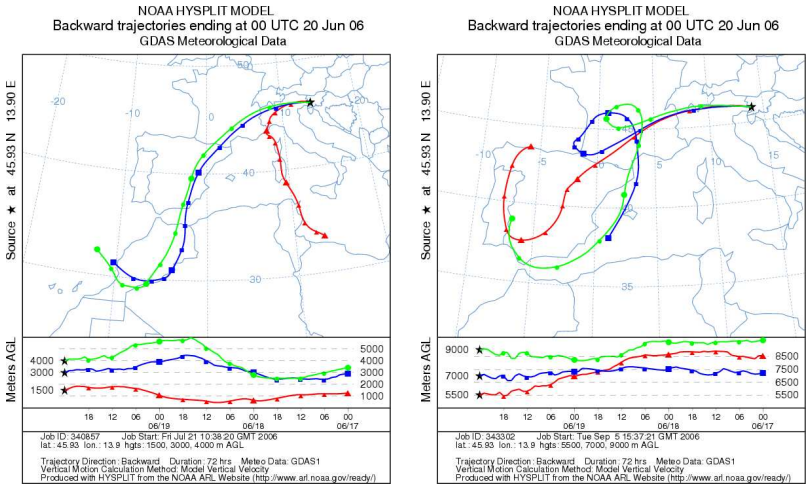


(a) (b)

**Figure 4.15:** Backward trajectories denoting the arrival of air at the Otlica on the $20^{th}$ of June 2006 at heights: (a) 1500 m, 3000 m and 4000 m and (b) 5500 m, 7000 m and 9000 m.

### 4.3.4 Case 4: June 20, 2006

Trajectories shown in Figure 4.15 denote the air arriving above the Trnovski gozd region at 0:00 UTC on the June $20^{th}$ 2006. Trajectory at 1.5 km passes above the Mediterranean sea reaching Slovenia. The trajectories at 3 km and 4 km represent the continental tropical air mass that passes North of Africa and Southwest of Europe. The higher three trajectories (5.5 km, 7 km and 9 km) circle over Spain and partially over the Mediterranean. All trajectories are assigned to class SW-W.

Weather on this day was predominantly clear with occasional summer storms occurring in Northern parts of Slovenia [68].

A two day averaged SLP map is given in Figure 4.16.a. Above Slovenia is visible constant high SLP field. At the Southwest region of the North Atlantic, West of Spain and up to Cape Verde, a high SLP field is present. A low SLP field above the Northwestern part of North Atlantic Ocean is also visible. The strong SLP gradient field between last two mentioned

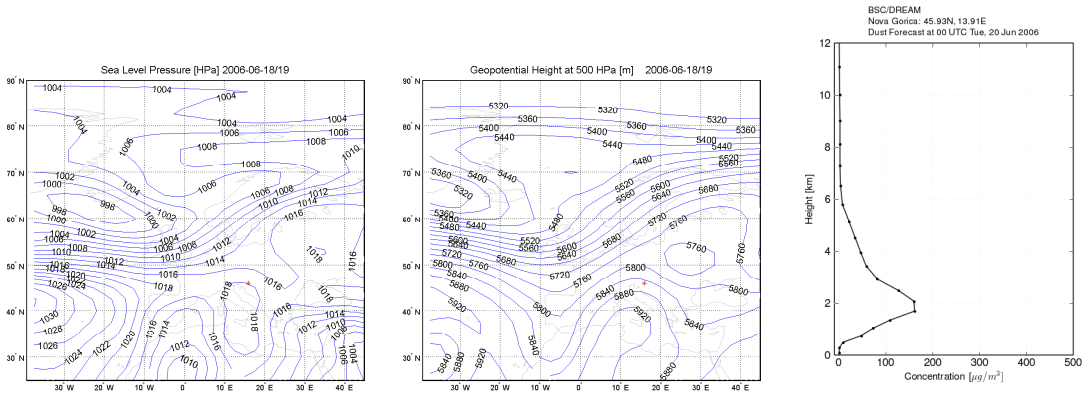


**Figure 4.16:** Average synoptic pattern of sea-level pressure (a) and 500 hPa geopotential height (b) for $18^{th}$ and $19^{th}$ of June 2006, together with Saharan dust concentration above Otlica (c) predicted by DREAM model for $20^{th}$ of June 2006.

SLP fields, indicates the flow of air along isobars from Northwest to Northeast. Part of the air above Iceland changes the flow direction to the Southwest. This air flow does not reach the Slovenia region. A weak gradient field is present in Northwestern Africa and the Western Mediterranean. From the Southwest (above Lybia) air arrives to the region of Slovenia, carried by weak winds. The GPH500 map is given in Figure 4.16.b. A strong GPH500 gradient field in the Northwestern region of the North Atlantic (Iceland Basin, North of the United Kingdom and up to Scandinavia) is visible. Most of the isolines indicate flow of air from the Northwest to the Northeast. This group of isolines spreads over Cape Finister and Spain. The air flow corresponding to the GPH500 field in this region, represented by isolines, arrives to Slovenia.

The DREAM model predicted the presence of Saharan dust aerosols above Slovenia at 0:00 UTC on the $20^{th}$ of June, 2006 (Figure 4.16.c). The desert dust concentrations are lower than in estimations done for the previous case. The model predicts Saharan dust presence up to 6 km above the sea level, with a peak in concentration at 2 km.

This day measurement is represented by LIDAR run containing 150 events. Peaks around 6.5 km above the ground are visible from the $S$ function (Figure 4.17). Extinction and scattering aerosol coefficient profiles exhibit a clear digression from zero up to 12 km above the ground. The extinction to back-scattering ratio used is 35. Up to 6 km above the sea level the DREAM model predicted the presence of Saharan dust aerosols. Relying on the extinction to back-scattering ratio value that is close to the one characteristic for desert aerosols, air mass history, and prediction of DREAM model, up to 5 km above the ground we can assume presence of Saharan dust aerosols in the atmosphere above Oltica. Above 5 km coefficient values still digress from zero having a highest values around 7 km above the ground. Although the DREAM model do not predict desert aerosols at altitudes higher then 6 km above the sea level, i.e 5 km above the ground, based on the LIDAR ratio and air history we can assume Saharan dust presence even at higher altitudes. Since air trajectories for heights above 6 km from sea level, shown in Figure 4.15, are passing partially over the Mediterranean Sea they make it possible that the air also contains some maritime aerosols at these altitudes. Optical depth values are lower than in the previous case where it was also assumed that there was

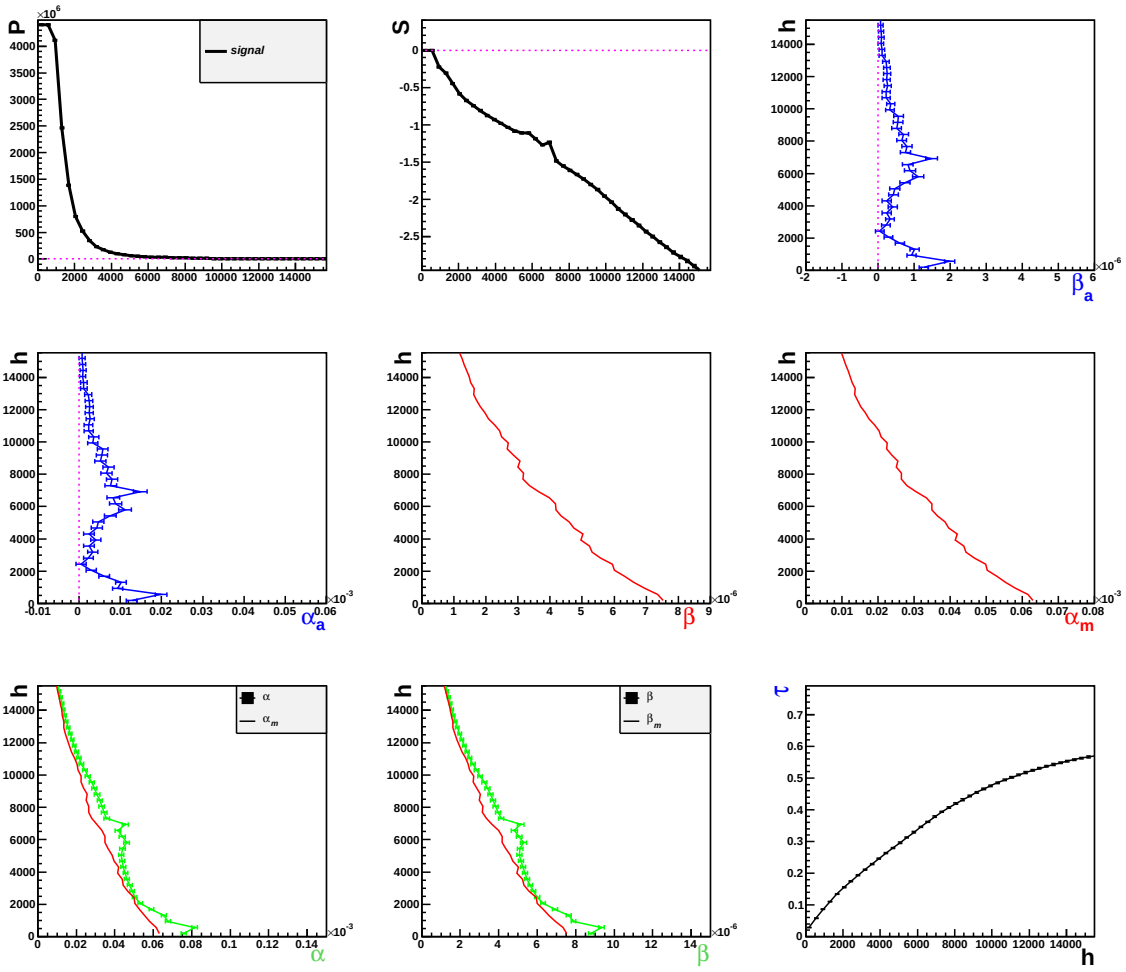


**Figure 4.17:** Vertical profiles of original LIDAR signal ($P$), $S$-function and different atmospheric optical properties $\beta_a$, $\alpha_a$, $\alpha_m$, $\beta_m$, $\alpha$, $\beta$ and $\tau$ based on Run 121, taken on June $20^{th}$, 2006.

desert dust presence. The main reason for lower $\tau$ values is the cloudless atmosphere. Up to a height of of 15 km the cumulative value of optical depth reaches about $0.6 \pm 0.1$ and due to this the beam is attenuated to a factor of $e^{-0.6}$.

### 4.3.5 Case 5: June 27, 2006

Air trajectories associated with the passage of air arriving above Trnovski gozd region at 0:00 UTC on June $27^{th}$ 2006 are presented in Figure 4.18. The lowest air trajectory (1.5 km) passes above the Mediterranean Sea. Winds blowing from this direction are slow and weak. This trajectory belongs to class C. Air trajectory at 3 km above sea level passes above part of Northern Africa. It is assigned to the SW-W class. Winds blowing from this direction bring the continental tropical air mass. The other air trajectories pass over the North Atlantic Ocean from the West and are assigned to the class SW-W.
During this day, Southwest winds brought warm air into a constant pressure region above

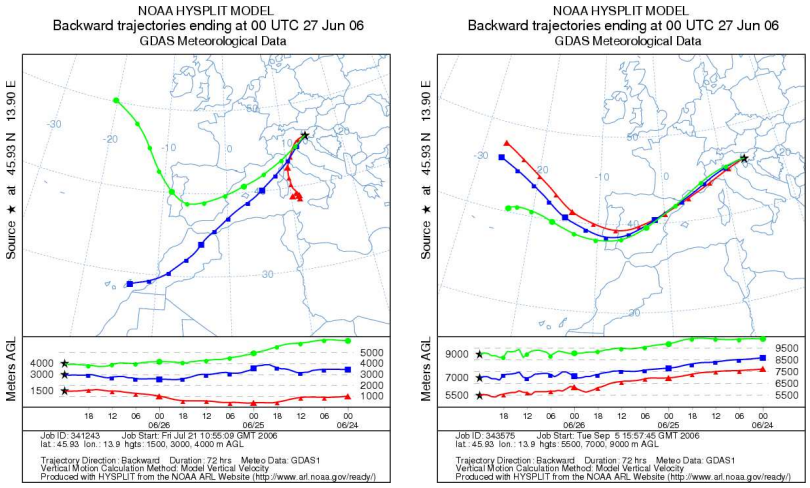


(a) (b)

**Figure 4.18:** Backward trajectories denoting the arrival of air at the Otlica on the $27^{th}$ of June 2006 at heights: (a) 1500 m, 3000 m and 4000 m and (b) 5500 m, 7000 m and 9000 m.

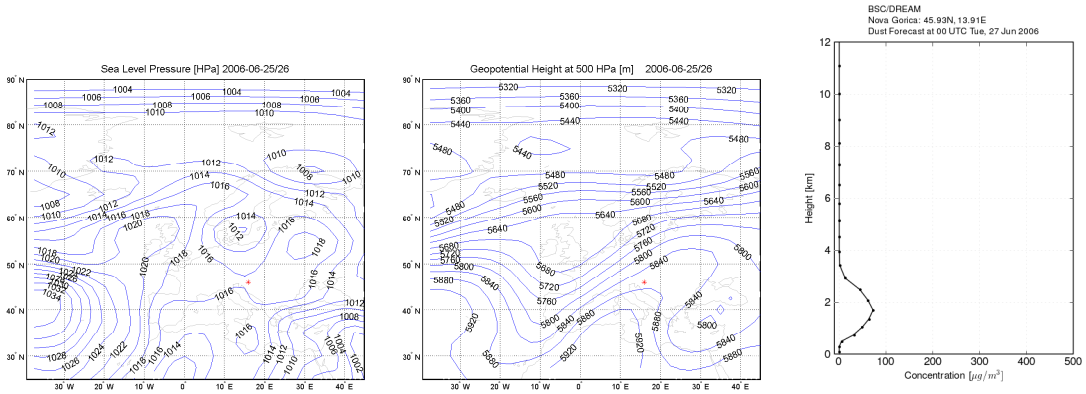


(a) (b) (c)

**Figure 4.19:** Average synoptic pattern of sea-level pressure (a) and 500 hPa geopotential height (b) for the $25^{th}$ and $26^{th}$ of June, 2006, together with Saharan dust concentration above Otlica (c) predicted by the DREAM model for June $27^{th}$, 2006.

Slovenia [68].

In Figure 4.19.a a map of SLP is presented. A constant high SLP field above Slovenia is visible indicating weak flows. At the Western part of the North Atlantic Ocean a high SLP field is present. The GPH500 map is presented in Figure 4.19.b. A strong GPH500 gradient field is present at Northwestern part of Atlantic Ocean, above the Iceland basin, Porcupine, and the Biscay plain. Above the United Kingdom the air splits and part of the air flows into the region North of Scandinavia and part flows to the Southwest. Later air flow circles over the Spain and reaches the Slovenia.

The DREAM model estimation for Saharan dust concentration above Otlica on the $27^{th}$ of June, 2006, is given in Figure 4.19.c. Presence of desert dust aerosols is predicted up to 3 km

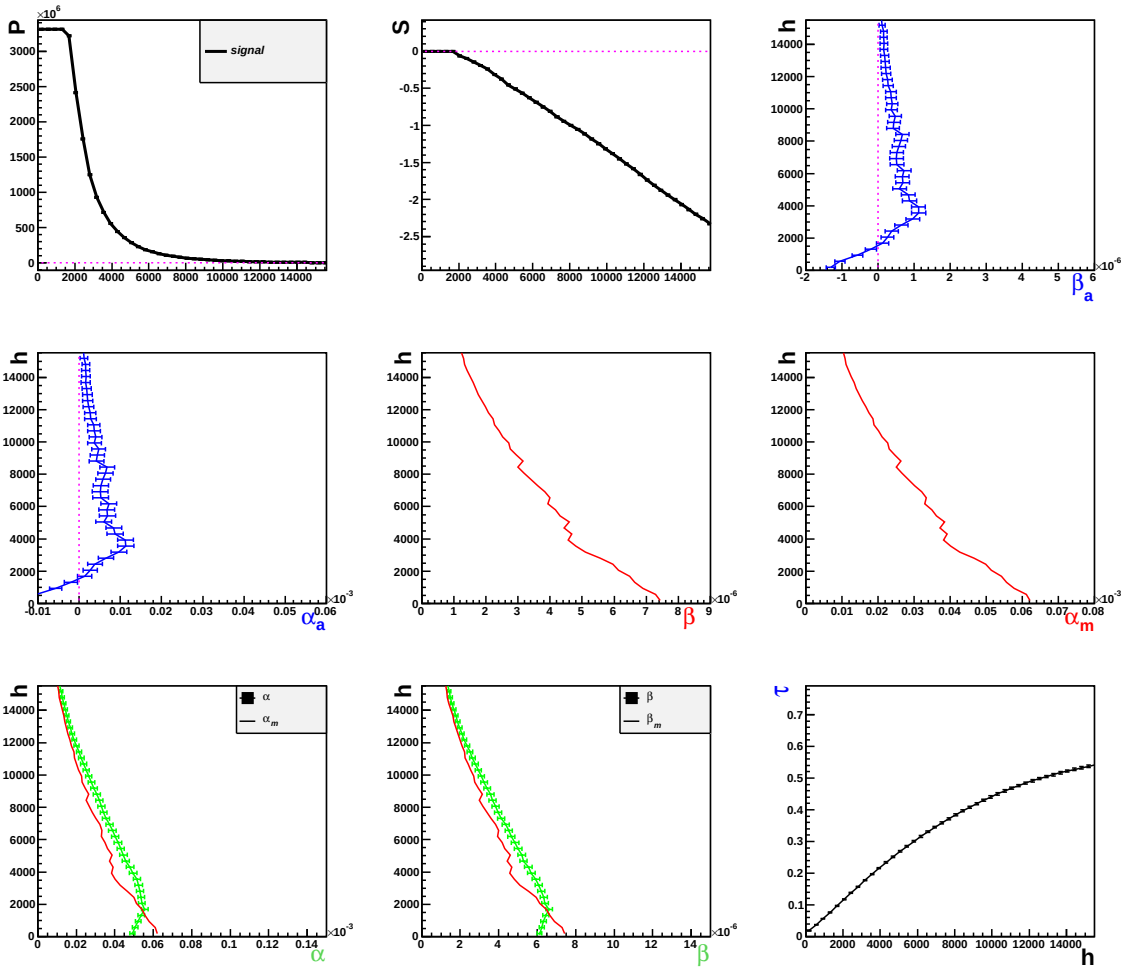


**Figure 4.20:** Vertical profiles of original LIDAR signal ($P$), $S$-function and different atmospheric optical properties $\beta_a$, $\alpha_a$, $\alpha_m$, $\beta_m$, $\alpha$, $\beta$ and $\tau$ based on Run 136, taken on June $27^{th}$ 2006.

above the sea level, with the highest concentration at about 1.8 km.
The LIDAR run consisted of 120 events (Figure 4.20). This day's measurements are taken with an increased PMT voltage. Aim was to probe atmosphere at higher altitudes. Due to saturation qualitative analysis up to 2 km is not possible. Although the DREAM model predicts the presence of Saharan dust aerosols around 2 km above the sea level, due to the state of the signal for this range this can not be confirmed. Extinction and back-scattering coefficients digress from zero above 2 km. The extinction to back-scattering ratio used in this analysis is $R = 20$. Although all the trajectories, except the lowest altitude one, are assigned to SW-W class, due to the LIDAR ratio and lower aerosol extinction and back-scattering values, than in previous cases containing desert aerosols, presence of Saharan dust is not so obvious. Since trajectories partially pass over Northern Atlantic and LIDAR ratio value is typical for maritime aerosols, we can assume presence of maritime aerosols 2 km above the ground. Optical depth values do not show any strong atmospheric opacity. The values are similar to the cases of clear sky day. Up to a height of of 15 km the cumulative value of

optical depth is about $0.55 \pm 0.1$. An optical depth of this value attenuates the laser beam by a factor of $e^{-0.55}$.

### 4.3.6 Case 6: July 14, 2006

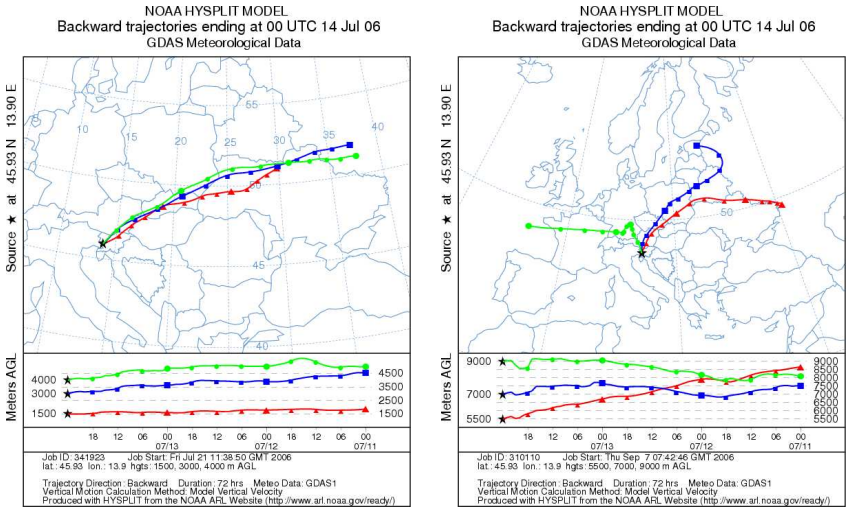


(a) (b)

**Figure 4.21:** Backward trajectories denoting the arrival of air at the Otlica on the $14^{th}$ of July, 2006, at heights: (a) 1500 m, 3000 m and 4000 m and (b) 5500 m, 7000 m and 9000 m.

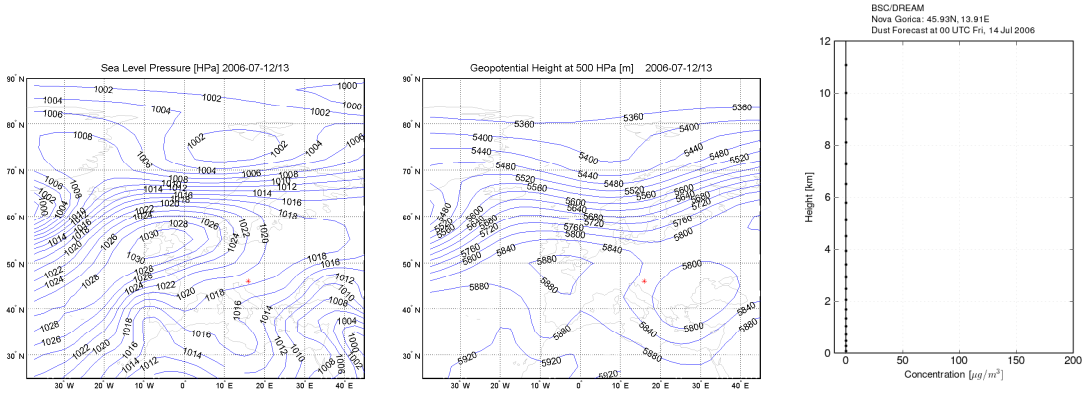


(a) (b) (c)

**Figure 4.22:** Average synoptic pattern of sea-level pressure (a) and 500 hPa geopotential height (b) for $12^{th}$ and $13^{th}$ of July 2006, together with Saharan dust concentration above Otlica (c) predicted by DREAM model for $14^{th}$ of July 2006.

Figure 4.21 shows air trajectories arriving above Trnovski gozd region at 0:00 UTC on July 14, 2006. Trajectories at the lower three altitudes (Figure 2.21.a) describe the path of air arriving from the East. Trajectories are very short indicating slow flow and stable weather. Trajectories at higher altitudes are presented in Figure 4.21.b. All trajectories, lower and

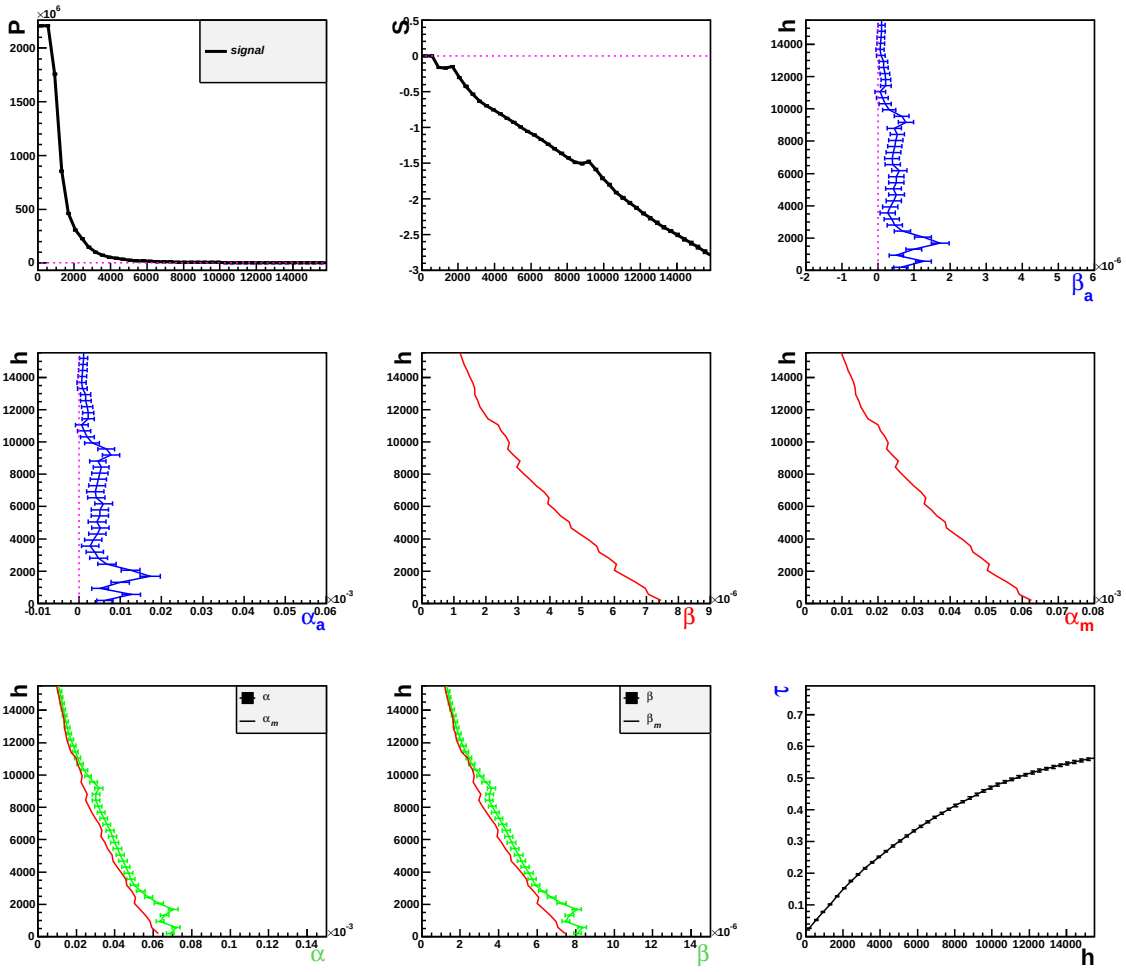


**Figure 4.23:** Vertical profiles of original LIDAR signal ($P$), $S$-function and different atmospheric optical properties $\beta_a$, $\alpha_a$, $\alpha_m$, $\beta_m$, $\alpha$, $\beta$ and $\tau$ based on Run 145, taken on $14^{th}$ of July 2006.

higher altitudes, are assigned to class C, except the air trajectory at height of 9 km above the sea level. Although, the 9 km trajectory looks like potential representative of NW-W class, clustering procedure assigned it to the SW-W class.

During the days up to and including the July $14^{th}$, above the region of West, middle, and partially Northern Europe was a high air pressure field present. In the Western part of Slovenia rare storms occurred while in the Southeast parts the weather was clear [68].

The SLP map is presented in Figure 4.22.a. There is a high SLP field above the United Kingdom and a low SLP field above Greece and Turkey. A strong SLP gradient field is visible at the Northwestern part of the North Atlantic Ocean, from Iceland South to Atores and East to Scandinavia. Air here flows from the Northwest to the Northeast. Above the Western part of the North Atlantic Ocean, from Atores Island to the Canary Islands, a weaker gradient field is visible. At Slovenia air arrives from the Northeast region. The GPH500 map is presented in Figure 4.22.b. A high GPH500 field is present above Slovenia. In addition, a strong GPH500 gradient field is visible at the Northwest part of the North Atlantic ($45^oN$-$80^oN$)

influencing the flow of air from the Northwest to the Northeast. Part of the air stream splits above Poland and air from North arrives to Slovenia. The high GPH500 field is visible above Southern part of the of the United Kingdom.
Since neither of these trajectories pass above Africa, the presence of Saharan dust aerosols above Slovenia is not expected (Figure 4.22.c). The DREAM model concentration profiles for the $14^{th}$ of July 2006, shown on Figure 4.22.c, predicts no presence of desert dust aerosols.
LIDAR run taken on Summer day of July $14^{th}$ has 120 events. The back-scattering to extinction ratio used in the Fernald method is 15. The signal $P$, $S$ function, extinction and back-scattering coefficients, and optical depth $\tau$ are presented in Figure 4.23. From the $S$ function small peaks, denoting a thin clouds, are visible around 2 km and 10 km above the ground. Since the air trajectory at 9 km above the sea level partially passes over the Atlantic Ocean, it is probable that the cloud formation is caused by the combination of warm and humid air brought from this direction. Aerosol coefficient profiles show digression from zero above 2 km up to 11 km, indicating aerosol presence. The LIDAR ratio suggests the presence of maritime aerosols, but due to the short trajectories passing only over continental region we have no other information to support this conclusion. From such short trajectories it is not possible to see if the air mass previously passed the maritime region which could result in the presence of maritime aerosols. Distribution of the optical depth values is similar to the previously measured cases that have the same extinction to back-scattering ratio. Up to a height of of 15 km above the ground the cumulative value of optical depth reaches approximately $0.6 \pm 0.1$ indicating the attenuation of laser light for a factor of $e^{-0.6}$ up to this height.

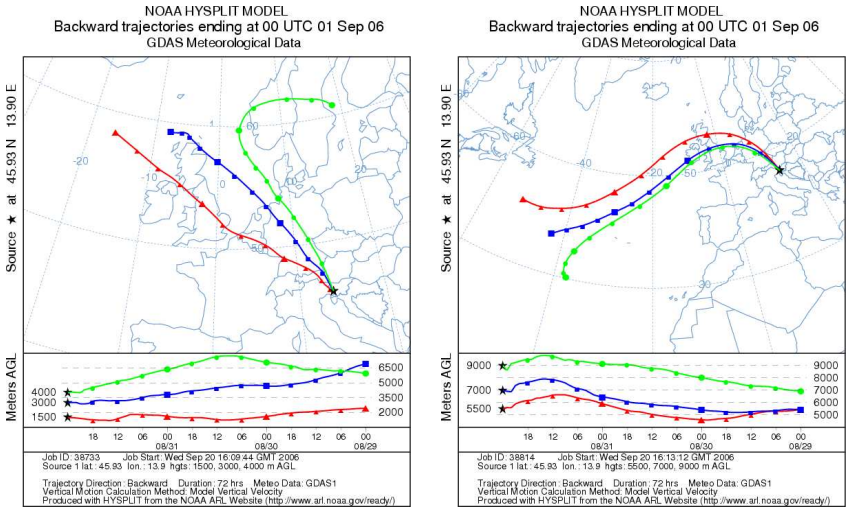


(a) (b)

**Figure 4.24:** Backward trajectories denoting the arrival of air at the Otlica on the $1^{st}$ of September 2006 at heights: (a) 1500 m, 3000 m and 4000 m and (b) 5500 m, 7000 m and 9000 m.

### 4.3.7 Case 7: September 1, 2006

Trajectories given in Figure 4.24 denote the air arriving above the Trnovski gozd region on the $1^{st}$ of September. All of the trajectories are passing over the Northwestern-Western part of the North Atlantic Ocean and are assigned to the NW-W class. Lower altitude air trajectories

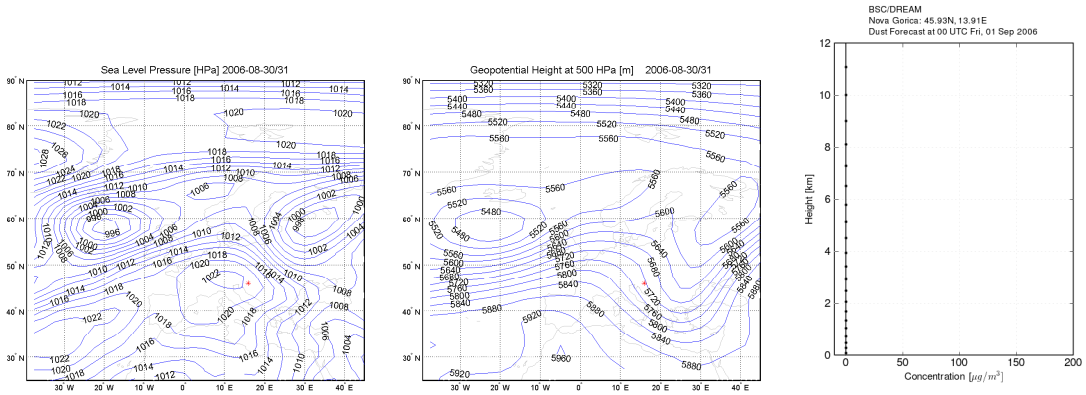


**Figure 4.25:** Average synoptic pattern of sea-level pressure (a) and 500 hPa geopotential height (b) for the $30^{th}$ and $31^{st}$ of August 2006, together with Saharan dust concentration above Otlica (c) predicted by the DREAM model for $1^{st}$ of September 2006.

are shorter than the higher ones, indicating slower winds.
Weather history showed the presence of high air pressure above the Alps. With Northwestern winds came dry air. During the day the weather was predominately clear [68].
A map of the two day average SLP is presented in Figure 4.25.a. The high SLP stated by [68] is visible. Also, high SLP fields above Slovenia and Greenland are visible. Two dominant gradient fields are visible. First one at North, above the Raykjanes basin and North of Scandinavia, denoting an air flow from the Northeast to the Northwest. The second one is visible at lower Northwestern latitudes, above Atores Island and up to Europe, with the air flow directed from the Southwest to the Northeast. A low SLP field is present between these two regions with strong gradients. Since the gradient filed in the region between $40^oN$ - $60^oN$ and $10^oE$ - $0^oE$, is very strong, it is possible that the air was arriving to Slovenia region parallel to the isobar lines. This would justify the air path given by the lower altitude trajectory obtained by HYSPLIT model. A two day average GPH500 map is given in Figure 4.25.b. Here the situation is a bit simpler. A strong GPH500 gradient field at Northwest ($40^oN$-$55^oN$) is present above all of Europe. Air flows from the Northwestern part of North Atlantic Ocean, over United Kingdom and France, reaching the Slovenia region.
The prediction of Saharan dust concentration above the Otlica region given in Figure 4.25.c shows zero concentration of desert aerosols for this day.
The LIDAR run taken on $1^{st}$ of September consists of 90 events (Figure 4.26). The signal $P$ and $S$ function indicate a clear atmosphere without clouds. The extinction to back-scattering ratio used is 15. The aerosol profiles ($\beta_a$ and $\alpha_a$) show digressions up to 13 km above the ground. Digression is more pronounced in the region between 2 km and 10 km above the ground. All trajectories denoting the arrival of air to Otlica, belong to class NW-W and pass over the North Atlantic ocean making it possible that the aerosols sensed by LIDAR are of maritime type. Also, LIDAR ratio used indicates this aerosol type. Total extinction and aerosol coefficients compared to the molecular ones, show small digressions in the region from 2 km to 10 km above the ground. Having clear sky conditions, the optical depth does not exhibit strong increases in atmospheric opacity. Up to a height of of 15 km the cumulative value of optical depth reaches about $0.6 \pm 0.1$, denoting attenuation of the laser beam for a

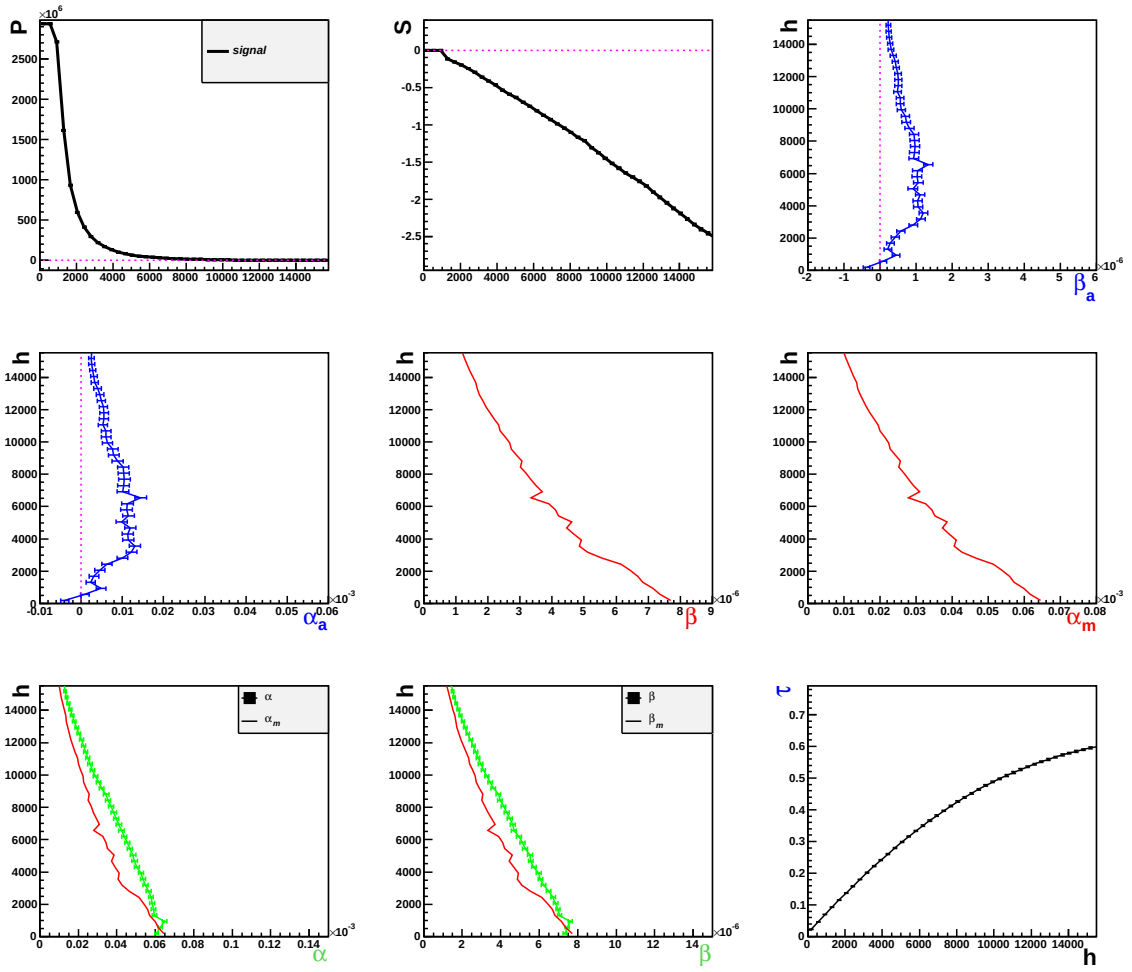


**Figure 4.26:** Vertical profiles of original LIDAR signal ($P$), $S$-function and different atmospheric optical properties $\beta_a$, $\alpha_a$, $\alpha_m$, $\beta_m$, $\alpha$, $\beta$ and $\tau$ based on Run 157, taken on $1^{st}$ of September 2006.

factor of $e^{-0.6}$.

### 4.3.8 Case 8: September 28, 2006

Air trajectories arriving to the Trnovski gozd region on the $28^{th}$ September at midnight are presented in Figure 4.27. At lower altitudes air is brought by the winds blowing from East. These winds are very slow and indicate stable weather conditions. Lower three trajectories are representatives of class C. Air trajectories at the higher three altitudes are typical representatives of the NW-W class and pass over Northwestern-Western part of the North Atlantic Ocean.
During the $27^{th}$ and $28^{th}$ of September a low SLP field was present at Southwest from Slovenia. Above the Southern parts of the Adriatic Sea at higher altitudes, on the morning of September $28^{th}$ cold air was present. During the day, Northwestern winds began to blow, bringing in less humid air [68].

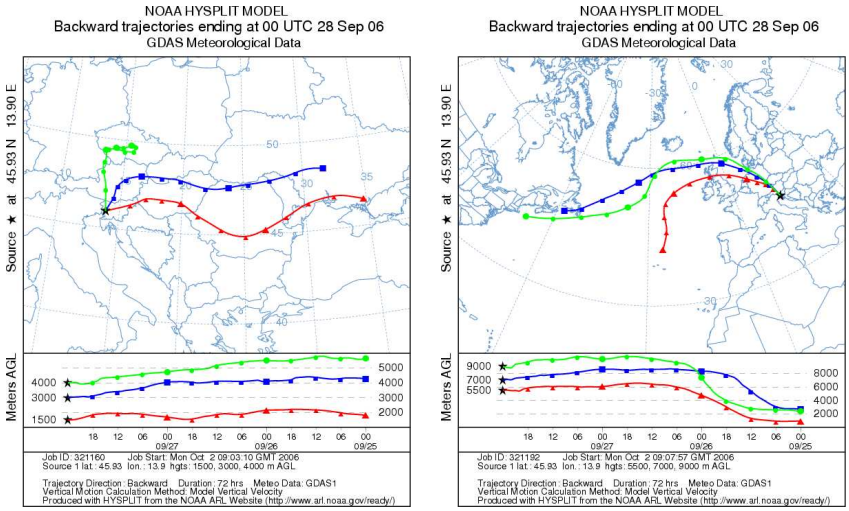


(a) (b)

**Figure 4.27:** Backward trajectories denoting the arrival of air at the Otlica on the $28^{th}$ of September 2006 at heights: (a) 1500 m, 3000 m and 4000 m and (b) 5500 m, 7000 m and 9000 m.

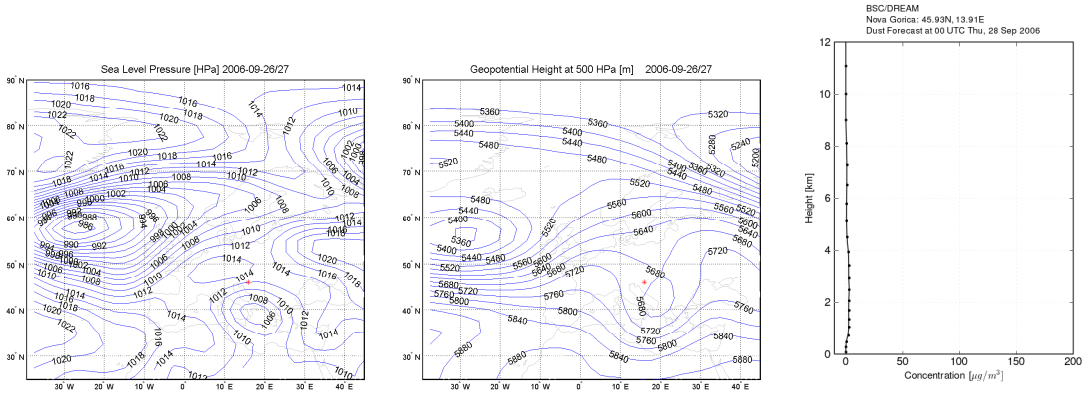


(a) (b) (c)

**Figure 4.28:** Average synoptic pattern of sea-level pressure (a) and 500 hPa geopotential height (b) for $26^{th}$ and $27^{th}$ September 2006, together with Saharan dust concentration above Otlica (c) predicted by DREAM model for $28^{th}$ of September 2006.

Maps of SLP and GPH500 are shown in Figure 4.28.a and 4.28.b. High SLP fields at Northern and Southern part of the North Atlantic ocean with a strong depression (low SLP) in the middle above the Iceland's basin are visible. Above Northern Italy and Slovenia, low SLP fields a is present. Also high SLP field on East, above Ukraine is visible. The weak winds blowing from the East, over Ukraine, Romania and Hungary, bring the air to Slovenia. A strong GPH500 gradient is present at the Western part of North Atlantic Ocean, above the Maxwell fracture zone. A low GPH500 field above the Iceland Basin and a high GPH500 field Southwest of the North Atlantic above the Madeira Islands are visible. From the Northwest, between these two SLP fields, the air arrives to the Slovenia region.

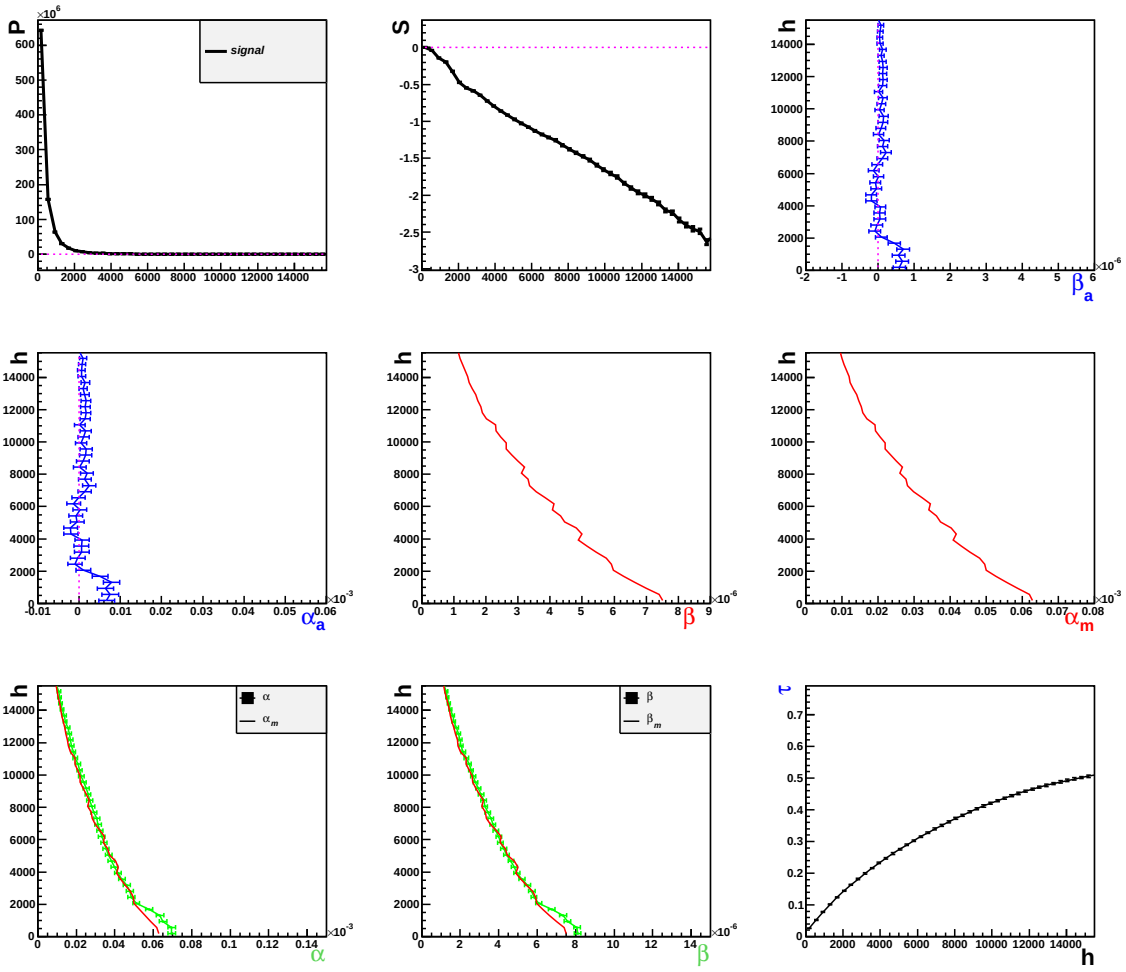


**Figure 4.29:** Vertical profiles of original LIDAR signal ($P$), $S$-function and different atmospheric optical properties $\beta_a$, $\alpha_a$, $\alpha_m$, $\beta_m$, $\alpha$, $\beta$ and $\tau$ based on Run 202, taken on $28^{st}$ of September 2006.

Figure 4.28.c shows the prediction of Sahara desert dust concentration. Traces of desert dust aerosols up to 4 km are visible.

This LIDAR run consisted of 150 events. The cloudless sky is visible from the distributions of signal $P$ and $S$ function in Figure 4.29. The extinction to back-scattering ratio used is 15. The aerosol extinction and back-scattering coefficients exhibit significant digressions up to 2 km. DREAM model predicts trace presence of desert aerosols, but used LIDAR ratio does not support this assumption. From the air paths, even the prediction given by DREAM model about the trace aerosol presence is not obvious. Also, although the lower air trajectories belonging to class C are short and pass over continental area indicating presence of continental aerosols, due to the LIDAR ratio and small coefficient values we can not confirm this. The air trajectories calculated for higher altitudes pass above the Northwestern part of the North Atlantic Ocean. Due to the air history and LIDAR ratio used, we can suppose presence of maritime aerosols at at heights from 5 km above the ground. Overall, above 2 km total extinction and scattering profiles are matching the molecular ones. This and extinction

to back-scattering ratio state that the atmosphere is very clean. It is possible that occasional summer storms have washed out the majority of the aerosols. Up to a height of of 15 km above the ground, the cumulative value of optical depth reaches about $0.5 \pm 0.1$. In most of the cases shown, cumulative value of $\tau$ at this height is the same.

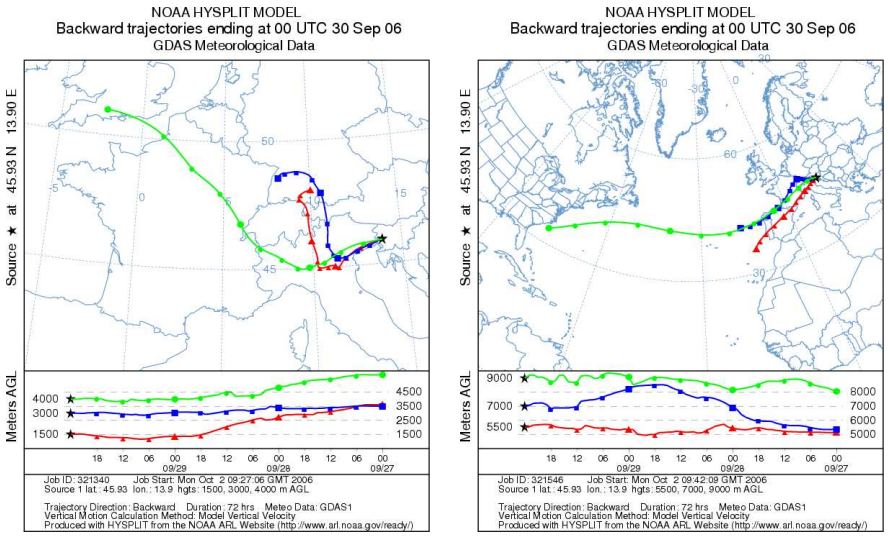


(a) (b)

**Figure 4.30:** Backward trajectories denoting the arrival of air at the Otlica on the $30^{th}$ of September, 2006, at heights: (a) 1500 m, 3000 m and 4000 m and (b) 5500 m, 7000 m and 9000 m

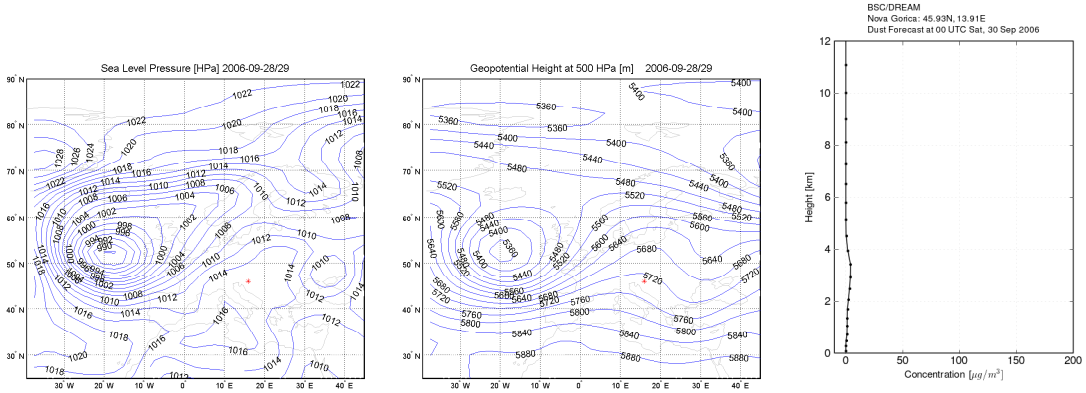


(a) (b) (c)

**Figure 4.31:** Average synoptic pattern of sea-level pressure (a) and 500 hPa geopotential height (b) for the $28^{th}$ and $29^{th}$ of September, 2006, together with Saharan dust concentration above Otlica (c) predicted by DREAM model for $30^{th}$ of September 2006.

### 4.3.9 Case 9: September 30, 2006.

Air trajectories (Figure 4.30) indicate the arrival of air at midnight on September 30, 2006, above the Trnovski gozd region. The lower three altitude trajectories are characterized by very slow and stable Western flow and are assigned to class C. Air trajectory at a height of 4 km is longer since winds blowing at this altitude are faster. The trajectory describes the path of air passing above the United Kingdom. The air trajectories at higher altitudes (Figure

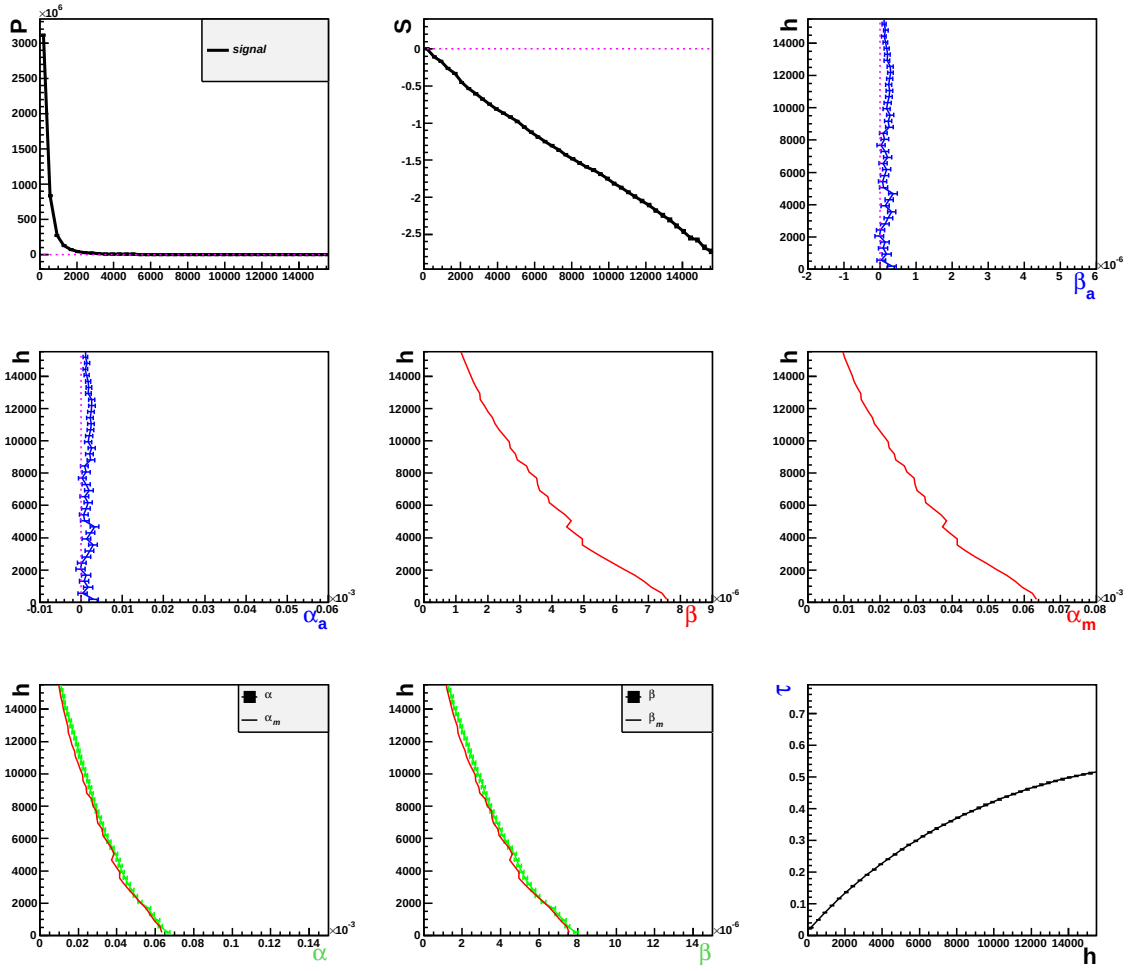


**Figure 4.32:** Vertical profiles of original LIDAR signal ($P$), $S$-function and different atmospheric optical properties $\beta_a$, $\alpha_a$, $\alpha_m$, $\beta_m$, $\alpha$, $\beta$ and $\tau$ based on Run 229, taken on $30^{th}$ of September 2006.

4.30.b) pass over the Western part of the North Atlantic Ocean. Winds blowing from this direction are very fast. Trajectory at 5.5 km is assigned to class SW-W. Other two higher altitude trajectories are assigned to class NW-W.
Above the Mediterranean, the Alps, and the Balkans a high pressure field was present. At higher altitudes from the West warm air was coming. It was partially clear with occasional clouds [68].
The map of SLP is shown in Figure 4.31.a. A constant high SLP field above the Mediterranean

and the Alps, and a low SLP field West of the United Kingdom, above the Iceland Basin and Faraday and Maxwell fracture zones, are visible. A strong SLP gradient is present in the Northwestern region ($40^o$N-$70^o$N). Due to the constant SLP field above Slovenia there are no strong wind streams. The GPH500 map is presented in Figure 4.31.b. Here a low GPH500 field Western of the United Kingdom is visible. The GPH500 gradient field is present in the Western part of the North Atlantic Ocean. The air flow from the West, represented by isolines corresponding to the GPH500 field in this region, arrives in Slovenia.
The Saharan dust estimations for September $30^{th}$ given by the DREAM model are similar to the one in previous case. From the profile given in Figure 4.31.c we can see the presence of traces of Saharan dust aerosols in the region up to 4 km above the sea level.
This LIDAR data consisted of 150 events. From the $S$ function given in Figure 4.32 the cloudless sky is visible. The extinction to back-scattering ratio taken in this case is 10. These aerosol coefficient profiles exhibit small digressions from zero. The coefficients obtained for this case are the smallest compared to the other cases considered. The DREAM model predicts desert aerosols at lower altitudes and air trajectory at 5.5 km belongs to SW-W class, but LIDAR ratio is one characteristic for clear atmosphere and we cannot state presence of Saharan dust aerosols. Since the air at higher altitudes arrives from Northwestern parts of the North Atlantic ocean, presence of maritime aerosols is possible. The optical depth values are lower than those in previously measured case. Due to this, the lower value of the extinction to back-scattering ratio, as well as the small coefficient values, the atmosphere here is less opaque to the propagating laser light. Up to a height of of 15 km the cumulative value of an optical depth reaches about $0.5 \pm 0.1$, attenuating the incident laser beam for a factor $e^{-0.5}$. Compared to the other presented cases, this measurement has the lowest optical depth values and exhibits the cleanest atmosphere.

## 4.4 Case study summary

The analysis of the LIDAR cases gave information about aerosol presence in the atmosphere. Study of LIDAR back-scattered signal, using the Fernald method provided the values of aerosol and molecular extinction and back-scattering coefficients, separately as well as the optical depth values. The estimation of the LIDAR ratio value is necessary for coefficient calculations. On the other hand the extinction to back-scattering ratio in each measured case is also used as information which indicates the probable type of detected aerosols. Since, at all altitudes, a constant value of this LIDAR ratio is used, determination of the aerosol types in this way is not very precise. Hence, additional information is pointed out analyzing the air mass history, since the type of aerosol is governed by the air mass origin. This study considered the relationship between detected aerosols and synoptic meteorology, providing information about aerosol presence and type, as a result. The main information obtained by the LIDAR analysis are presented in a Table 4.2. The statistical uncertainties on the retrieved aerosol coefficient values have been calculated from the law of error propagation by assuming a Poisson distribution on LIDAR signals (Section 3.3.2).

| LIDAR cases | Case 1 24-6-2005 | Case 2 25-6-2005 | Case 3 17-6-2006 | Case 4 20-6-2006 | Case 5 27-6-2006 | Case 6 14-7-2006 | Case 7 1-9-2006 | Case 8 28-9-2006 | Case 9 30-9-2006 |
|---|---|---|---|---|---|---|---|---|---|
| | Air trajectories assigned to the typical airflow classes | | | | | | | | |
| 1.5km | C | C | C | SW-W | C | C | NW-W | C | C |
| 3km | NW-W | C | SW-W | SW-W | SW-W | C | NW-W | C | C |
| 4km | NW-W | C | SW-W | SW-W | SW-W | C | NW-W | C | C |
| 5.5km | NW-W | C | SW-W | SW-W | SW-W | C | NW-W | NW-W | SW-W |
| 7km | NW-W | C | SW-W | SW-W | SW-W | C | NW-W | NW-W | NW-W |
| 9km | NW-W | SW-W | SW-W | SW-W | SW-W | SW-W | NW-W | NW-W | NW-W |
| | Aerosol coefficients, LIDAR ratio and optical depth | | | | | | | | |
| LIDAR ratio | 15 | 15 | 35 | 35 | 20 | 15 | 15 | 15 | 10 |
| $\beta_a$ $[10^{-6}\mathrm{m}^{-1}\,\mathrm{sr}^{-1}]$ | 0.5± 0.2* | 0.4±0.1* | 3.0±0.4* | 1.2±0.3 | 1.0±0.3 | 0.5±0.1* | 1.0± 0.3 | 0.5±0.1 | 0.3±0.1 |
| $\alpha_a$ $[10^{-5}\mathrm{m}^{-1}]$ | 0.5± 0.2 | 0.4±0.1 | 3.0±0.4 | 1.2±0.3 | 1.0±0.3 | 0.5±0.1 | 1.1±0.3 | 0.5±0.1 | 0.4±0.1 |
| $\tau$ | 0.6±0.1 | 0.8±0.2 | 0.8±0.2* | 0.6±0.1 | 0.55±0.1 | 0.6±0.1 | 0.6 ±0.1 | 0.5±0.1 | 0.5±0.1 |
| type of aerosols | maritime | not conclusive | Saharan dust | Saharan dust | Saharan dust maritime | not conclusive | maritime | maritime Saharan dust | maritime |

**Table 4.2:** LIDAR results for measurements taken on different days under different synoptic situations. Besides maximum aerosol back-scattering $\beta_a$ and extinction $\alpha_a$ coefficients for single cases, up to a height of 15 km the cumulative value of an optical depth $\tau$ is given. A mark $*$ denotes that clouds were present, but that maximal value of coefficients in the cloud is not considered.

# 5 Conclusions

This thesis presents the first measurements of Otlica LIDAR system, and is a part of the endeavor to establish LIDAR monitoring of the atmosphere above Slovenia. The research activities were oriented both in hardware - construction of the observatory site and mounting of the LIDAR system, and in the software, including the development of data acquisition and analysis software. The analysis is focused on the detection of tropospheric aerosols, estimation of their arrival paths and evaluation of aerosol impact on optical properties of the atmosphere. The aerosol extinction and back-scattering values, as well as optical depth values, can generally be used to correct the different air history models. Since the LIDAR does not yet operate full time, and since the LIDAR information on the aerosols in the atmosphere with the present setup is not complete, only separate cases under different atmospheric conditions were studied. The HYSPLIT model and K-means method are used to provide the information about typical directions of air flow arriving to the region of Slovenia. The information about the air mass properties arriving from different directions, is used to verify the type of aerosols by the LIDAR ratio obtained. The vertical profiling performed by means of LIDAR sensing inferred the presence of aerosols in the troposphere.

The air above Slovenia comes from different directions at different altitudes. Due to this, the air trajectories, at least 48 hours long, are computed for 6 different heights (1.5 km, 3, km, 4 km, 5.5 km, 7 km and 9 km). In order to determine typical directions of air arriving to Otlica, the clustering procedure and validation of the optimal clustering number, using the silhouette and RMSD methods was deployed. This resulted in recognition of four typical directions (classes) of air that arrives to Slovenia: Central class (C), Southwest-West class (SW-W), Northwest-West (NW-W) and Northern class (N).

The relative frequencies of occurrence, of trajectories assigned to each different class, compared to overall number of trajectories, showed that most of the air trajectories belongs to the SW-W class and class C. The frequency of trajectories belonging class SW-W compared to the total number of trajectories in total time period at different altitudes have values from 47% to 30%, while the frequencies for class C have values from 30% to 25%. This tendency is also present for each season separately. The relative trajectory frequencies for N an NW-W classes are similar when considering different heights of arrival and are characterized by lower relative frequencies ($\approx 20\%$).

The summary the LIDAR study results are shown in Table 4.2 given in Section 4.4. The air trajectories denoting the arrival of air to Otlica at different altitudes are assigned to typical directions of airflow. Type of the aerosols detected by LIDAR system assumed on the basis of the LIDAR ratio estimations and air mass history, are mostly maritime and desert.

Various type of aerosols influence the optical properties of the atmosphere producing the different values of back-scattering and extinction coefficients, as well as optical depth values.

Different altitude air trajectories for each case, denote the arrival of air from different direc-

tions. The air arriving from the SW-W direction, mostly brought the Saharan dust. The highest aerosol coefficient values are obtained in the case of Saharan dust presence where the LIDAR ratio had values of 35. Maximum values of coefficients, among all cases containing desert dust, are $\beta_a = (3.0 \pm 0.4)\,10^{-6}\mathrm{m}^{-1}\,\mathrm{sr}^{-1}$ and $\alpha_a = (3.0 \pm 0.3)10^{-5}\mathrm{m}^{-1}$. Up to a height of 15 km the cumulative value of an optical depth in this case reaches about $0.8 \pm 0.3$. The LIDAR ratio of 15 indicated maritime type of aerosols, usually brought by the air arriving from Northwestern directions. The aerosol coefficients in this case have lower values than in cases containing the desert dust aerosols. A maximum values among all cases containing the maritime aerosols are: $\beta_a = (1.0 \pm 0.3)\,10^{-6}\mathrm{m}^{-1}\,\mathrm{sr}^{-1}$ and $\alpha_a = (1.0 \pm 0.3)\,10^{-5}\mathrm{m}^{-1}$. Up to a height of 15 km the cumulative value of an optical depth reaches about $0.6 \pm 0.1$. The presented LIDAR data did not contain any representative of the class N. When the air was brought by slow and weak winds characteristic for class C, prevailing type of aerosols was not possible to specify. In general, the air trajectories denote the arrival of air from various directions and altitudes making it possible that type of aerosols present, varies with height. Due to this, to determine all types of detected aerosols, variation of LIDAR ratio with altitude need to be studied.

Based on results we can conclude that the air masses coming from North and Northwest-west directions are bringing mostly maritime aerosols that result in lower values of extinction and back-scattering coefficients as well as lower cumulative value of optical depth up to the top of the troposphere. On the contrary, air masses coming from Southwest-west direction commonly contain Saharan dust, which results in higher values of above mentioned optical properties. Due to the specific properties of trajectories in Central class, some general conclusion about the typical aerosols and values of optical properties is not possible. Unfortunately there were no representative of the class N, among the presented LIDAR cases.

The results presented in this thesis do establish certain correlations between the LIDAR measurements and air mass model results, thus offering possible explanations on the appearance of different aerosol types above Slovenia and their influence on the optical properties of the atmosphere. The combined LIDAR and air trajectory study can be a base for future research, when an upgraded LIDAR device will become available. The upgrade plans include enabling the daytime measurements, multiangle scanning and remote alignment. Upgrading the present system to a Raman LIDAR information about, for example micro-physical properties of aerosol, the size distribution, profiles of water vapor mixing ratio and ozone concentrations, can be obtained. Profiles of these atmospheric components as a function of altitude or location are necessary for weather forecasting, climate modeling, and environmental monitoring. Moreover, including the Otlica LIDAR into the European network and developing a mobile LIDAR can make the LIDAR based atmospheric studies an important future research field in Slovenia.

# Appendix A

## Standard Atmosphere calculation

The fundamental procedure for molecular profile determination is written in program subroutine that accepts altitude, temperature and pressure as an input argument and returns non-dimensional values of temperature, pressure, and density which are ratios of the quantity at altitude to the one at sea-level. The equations used in calculation are taken directly from the NASA publication [50]. The standard atmosphere is defined as a set of layers and the routine determines which layer contains the specified altitude. The desired layer is found by binary search.
Additional data is taken from the radiosonde readouts from Udine, Italy. Radiosonde data did not contain full information about the altitudes. We calculated them using the temperature and pressure data that was readout by radiosonde:

$$h_i = h_{i-1} - \frac{T_i + T_{i-1}}{2} \frac{287}{g} ln(\frac{p_i}{p_{i-1}}) \tag{A.1}$$

with the $T_i$ and $T_{i-1}$ as temperatures at missing height and heigh below it ($h_i$ and $h_{i-1}$), $p_i$ and $p_{i-1}$ as pressures and $g$ gravitational constant. In the case when the lower height was missing, we calculated average height regarding to the upper one $i + 1$:

$$h_i = h_{i+1} - \frac{T_i + T_{i+1}}{2} \frac{287}{g} ln(\frac{p_{i+1}}{p_i}) \tag{A.2}$$

In the case where we had information on both, lower and upper, heights aberagde height calculated from the values obtained by Equations (A.1) and (A.2), is used as missing height $h_i$.
All calculated heights, with coreesponding temperatures and pressures are used as additional input data, beside data taken for the standard atmosphere above $32\,km$. Since the definition of the international standard is given in SI units, the altitude is supplied in kilometers. Standard is defined as having a temperature of $288.15K$ at mean sea level ($0\,km$ geopotential height = $1013.25\,hPa$) with various lapse rates which change at seven specified geopotential heights. The temperature is given by:

$$T(h) = T_i + LR_i\,(h - h_i) \tag{A.3}$$

where $T_i$ is temperatures under standard condition at $i$-th height ($h_i$) and $LR_i$ is the lapse rate calculated from temperature change with height. Then $LR_i$ is also used as input value in our calculation of molecular profiles. The pressure profile is computed from the hydrostatic equation:

$$\frac{d}{dh}p(h) = -\rho(h)\, g \tag{A.4}$$

in equation, $p$ stands for pressure, $\rho$ for density and $H$ is height. This equation also can be used to derive expressions for converting between pressure and pressure altitude. For the density determination Ideal Gas Law is used:

$$p(h) = \rho(h)\, R\, T(h) \tag{A.5}$$

By combining last two equations we obtain:

$$\frac{d}{dh}p(h) = -\frac{p(h)\, g}{R\, T(h)} \text{i.e} \quad d(ln(p)) = -\frac{g}{R} \cdot \frac{dh}{T(h)} \tag{A.6}$$

which can be converted to the following integral equation:

$$\int_{p_{s_i}}^{p} d(ln(p)) = -\frac{g}{R} \int_{h_{S_i}}^{h} \frac{dh}{T_S(h)} \tag{A.7}$$

Here letter "$S$" denote the standard atmosphere values, and subscript $i$ denotes the altitude from which the integration is being initiated, $h_{S_i}$, $p_{s_i}$ and $T_S(h)$ denote the pressure altitude (km), pressure (hPa) and temperature (K) respectively; $R$ is the gas constant for dry air ($287.05307 J/kgK$), and $g$ is the acceleration of gravity at a latitude of $45.542^o$ ($= 9.80665 m/s2$). Integration of this equation to solve for the pressure ($p$) as a function of the pressure altitude ($h$) has two cases:

- If the lapse rate is not zero we calculate pressure as (converting from pressure altitude to pressure):

$$p(h) = p_{S_i} \left( \frac{T_S(h)}{T_{S_i}} \right)^{\frac{-1000\, g}{R\, LR_{S_i}}} \tag{A.8}$$

  where

$$T_S(h) = T_{S_i} + LR_{S_i}\, (h - h_{S_i}). \tag{A.9}$$

- If the lapse rate is zero pressure is calculated as:

$$p(h) = p_{S_i}\, exp\left[ \frac{-1000\, g\, (h - h_{S_i})}{R\, T_{S_i}} \right]. \tag{A.10}$$

# Bibliography


[1] Weitkamp, C., "Lidar - Range Resolved Optical Remote Sensing of the Atmosphere", Springer series in optical sciences, New York, (2005).

[2] Theopold, F.A. and Bosenberg, J., " Differential Absorption Lidar Measurements of Atmospheric Temperature Profiles: Theory and Experiment", Journal of Atmospheric and Oceanic Technology, 10, 165, (1993).

[3] Fujii, T. and Fukuchi, T., "Laser remote sensing", CRC Press - Taylor and Francis Group, (2005).

[4] Kovalev, V.A., Eichinger, W.E., "Elastic Lidar, Theory, Practice and Analysis Methods", John Wiley and Sons, Hoboken, New Jersey, (2004).

[5] Bosenberg, J., "EARLINET: A European Aerosol Research Lidar Network", Proceedings of the 20th International Laser Radar Conference, Vichy, (2000).

[6] Schneider, J., "A European aerosol research lidar network to establish an aerosol climatology (EARLINET)", Journal of Aerosol Science, 31, 1, 592-593, (2000).

[7] Houghton, J.T., Ding, Y., Griggs, D., Noguer, M., van der Linden, P.J., Dai, X., Maskell, K., C.A. Johnson., "Climate change 2001: The scientific basis", Cambridge University Press, Cambridge, (2001).

[8] Sasano, Y., "Tropospheric aerosol extinction coefficients profiles derived from scanning lidar measurements over Tskuba", Japan, from 1990 to 1993, Applied Optics, 35, 24, 4941-4952, (1996).

[9] Ansmann, A., Reibesell, M. and Weitkamp, C., "Measurement of the aerosol extinction profiles with a Raman LIDAR", Optics Letters, 15, 13, 746, (1999).

[10] Balis, D.S., Amiridisa, V., Zerefosa, C., Gerasopoulosa, E., Andreaeb, M., Zanise, P., Kazantzidisa, A., Kazadzisa, S. and Papayannisc, A., "Raman lidar and sunphotometric measurements of aerosol optical properties over Thessaloniki, Greece during a biomass burning episode", Atmospheric Environment, 37, 32, 4529-4538, (2003).

[11] Eixmann, R., Bockmannb, C., Fayc, B., Matthiasd, V., Mattise, I., Mullere, D., Kreiplf, S., Schneidera, J. and Stohl A., "Tropospheric aerosol layers after a cold front passage in January 2000 as observed at several stations of the German Lidar Network", Atmospheric Research, 63, 1-2, 39-58, (2002).

[12] Kolev, I., Savov, P., Kaprielov, B., Parvanov, O. and Simeonov, V., "Lidar observation of the nocturnal boundary layer formation over Sofia", Bulgaria, Atmospheric Environment, 34, 19, 3223-3235, (2000).

[13] Raj, P.E, Devara, P.C., Maheskumar, R.S., Pandithurai, G. and Dani, K.K., "Lidar measurements of aerosol column content in an urban nocturnal boundary layer", Atmospheric Research, 45, 3, 201-216, (1997).

[14] Matthias, V. and Bosenberg, J., "Aerosol climatology for the planetary boundary layer derived from regular lidar measurements", Atmospheric Research, 63, 3-4, 221-245, (2002).

[15] Kim, J., Yoon, S-C., Jefferson, A., Zahorowski, W. and Kang, C-H., "Air mass characterization and source region analysis for the Gosan super site, Korea, during the ACE-Asia 2001 field campaign", Atmospheric Environment, 39, 6513-6523, (2005).

[16] Mukai, H. and Suzuki, M., " Using air trajectories to analyze the seasonal variation of aerosols transported to the Oki Islands", Atmospheric Environment, 30, 23, 3917-3934, (1996).

[17] Witt, M., Bakera, A.R. and Jickellsa, T.D., "Atmospheric trace metals over the Atlantic and South Indian Oceans: Investigation of metal concentrations and lead isotope ratios in coastal and remote marine aerosols", Atmospheric Environment, 40, 28, 5435-5451, (2006).

[18] Tsaia, Y.I. and Chenb, C-L., "Atmospheric aerosol composition and source apportionments to aerosol in southern Taiwan", Atmospheric Environment, 40, 25, 4751-4763, (2006).

[19] Fernau, M.E. and Samson, P.J., "Use of cluster analysis to define periods of similar meteorology and precipitation chemistry in eastern North America. Part II: Precipitation patterns and Pollutant deposition", Journal of Applied Meteorology, 29, 751-761,

(1990).

[20] Eneroth, K., Kjellstrom, E. and Holmen, K., "A trajectory climatology for Svalbard; investigation how atmospheric flow patterns influence observed tracer concentrations", Physics of Chemistry of the Earth, 28, 119-1203, (2003).

[21] Dorling, S.R., Davies, T.D. and Pierce, C.E., "Cluster analysis: a technique for estimating the synoptic meteorological controls on air and precipitation chemistry - method and applications", Atmospheric Environment, 26A, 2575-2581, (1992).

[22] Filipčič, A., Horvat, M., Veberič, D., Zavrtanik, D. and Zavrtanik, M., "Scanning lidar based atmospheric monitoring for fluorescence detectors of cosmic showers", Astroparticle Physics, 18, 501-512, (2003).

[23] Saleh, B.E.A. and Teich, M.C., " Multiplied-Poisson noise in pulse, particle, and photon detection", Proceedings of Institute of Electrical and Electronics Engineers,70, 3, 229-245, (2005).

[24] Rakovec, J. and Vrhovec, T., "Osnove meteorologije - za naravoslovce in tehnike", Društvo matematikov, fizikov in astronomov Slovenije, Ljubljana, (2000).

[25] McCartney, E.J., "Optics of the atmosphere: Scattering by molecules and particles", John Wiley and Sons, New Jersey, (1976).

[26] Manahan, S.E., "Environmental Science and Technology", Lewis Publishers, Stockport, (1997).

[27] U.S. Environmental Protection Agency, "How air pollution affects the view, Emissions Monitoring and Analysis Division", Monitoring and Quality Assurance Group MD-14 Research Triangle Park, NC, (1999).

[28] Malm, C.W., "Introduction to Visibility", Cooperative Institute for Research in the Atmosphere (CIRA), Colorado State University, Fort Collins, (2000).

[29] Bergant, K., "Daljinsko zaznavanje lastnosti ozračja z lidarjem", Življenje in tehnika, 56, 5, 39-45, (2005).

[30] Hočevar, A., "Agrometeorologija", Tisk Krištoff, Ljubljana, (1992).

[31] Dutton, J. A., "An introduction to the theory of atmospheric motion", Dover, New York, (1986).

[32] Anderberg. M.R., "Cluster analysis for applications", Academic press, New York, (1973).

[33] Brilliant - Brilliant B, Instruction manual. Issue 5, Quantel SA, Les Ulis, (2002).

[34] Hamamatsu Photonics, "Photomultiplier Tubes, Basics and Applications", Second edition, (2005).

[35] Glass Filter Spectral Transmission Curves from Schott Catalog: http://www.schott.com/english/index.html.

[36] Argall, P. S. and Sica, R. J., "Imaging techniques and systems: LIDAR, Encyclopedia of Imaging Science and Technology", J. Hornak, New York, (2002).

[37] Baxter, R., "Laser safety training manual", University of Chicago Chemistry department, (1991): http://chemistry.uchicago.edu/safety/LaserSafety.pdf.

[38] Bergant, K., Kontić, B., Zavrtanik, M., "Lidar at Otlica above Ajdiovščina: description, performance, evaluation of impact of environment and health", Working report, PNG-DP-047, (2005).

[39] Savino, T.M., "Safety consideration for pulsed lasers", Curtis-Straus, LLC, (2002).

[40] ANSI, "American National Standard for the Safe Use of Lasers", American National Standards Institute, New York, (2000).

[41] Nackman, L.R. and Barton, J.J., "Scientific and Engineering C++", Addison-Wesley, New York, (1997).

[42] Acosta, D., "An object oriented data analysis framework", (2001): http://root.cern.ch.

[43] Measures, R. M., "Laser remote sensing: Fundamentals and Applications", John Wiley and Sons, New Jersey, (1984).

[44] Fernald, F. G., "Analysis of atmospheric lidar observations: some comments", Applied Optics, 23, 652, (1984).

[45] Cester, R., Mostafa, M. and Mussa, R., "LIDAR Telescopes for Atmospheric Monitoring", GAP Note 2001-052, (2001).

[46] Reagan, J. A., McCormic, M. P. and Spinhirne, J. D., "Lidar sensing of aerosols and clouds in the troposphere and stratosphere", Proceedings of the IEEE 77, 433-448, (1989).

[47] Takamura, T., Sasano, Y., Hayasaka, T., "Tropospheric aerosol optical properties derived from lidar, sun photometer and optical particle counter measurements", Applied Optics, 33, 7132-7140, (1994).

[48] Rocadenbosch, F., and Cameron, A., "Error analysis of the lidar back-scatter inversion algorithm", Applied Optics, 38, 4461, (1991).

[49] Genolini, B, Nguyen Trung, T., Pournas, J., Lhenry-Yvon, I., Parizot, E.and Soumijarvi, P., "Design of the photomultiplier basis for the surface detectors of the Pierre Auger Observatory", GAP Note 2001-021, (2001).

[50] United States Committee on Extension to the Standard Atmosphere, "U.S. Standard Atmosphere, 1976", National Oceanic and Atmospheric Administration, National Aeronautics and Space Administration, United States Air Force, Washington D.C, (1976).

[51] Burroughs, J., "Integrated Global Radiosonde Archive", (2006): http://www.ncdc.noaa.gov/oa/cab/igra/index.php

[52] Acosta, D., "How to perform a linear least-squares analysis, tutorial", (2001): http://root.cern.ch/root/html/examples/solveLinear.C.html

[53] Nickovic, S., Papadopoulos, A., Kakaliagou, O. and Kallos, G., "Model for prediction of desert dust cycle in the atmosphere", Journal of Geophysical Research, 106, 18,113 - 18, 129, (2001).

[54] Jacobson, M.Z., "Fundamentals of atmospheric modeling", United Kingdom University Press, Cambridge, (1998).

[55] Runca, E., "Basic Lagrangian and Eulerian modeling of atmospheric diffusion", Atmospheric Environment, 26A, 513-515, (1992).

[56] Pielke, R.A., McNider, R.T., Segal, M. and Mahrer, Y., "The use of a numerical mesoscale model for evaluations of pollutant transport and diffusion in coastal regions and over irregular terrain", American Meteorological Society, 64, 243-249, (1983).

[57] Stohl, A., "Computation, accuracy and applications of trajectories - a review and bibliography", Atmospheric Environment, 32 (6), 947-966, (1997).

[58] Draxler, R.R., "US National Oceanic and Atmospheric Administration (NOAA)", HYbrid Single-Particle Lagrangian Integrated Trajectory Model, (2006): http://www.arl.noaa.gov/ready/hysp_info.html

[59] US Environmental Protection Agency., "Technology Transfer Network Support Center for Regulatory Atmospheric Modeling", (2006): http://www.epa.gov/scram001/metmodel.htm

[60] Kistler, R., Kalnay, E., Collins, W., Saha, S., White, G., Wollen, J., Chelliah, M., Ebisuzaki, W., Kanamitzu, M., Kousky, V., van den Dool, H., Jenne, R., Fiorino, M., "The NCP/NCAP 50-year reanalysis", Bulletin of the American Meteorological Society, 2, 247-267, (2001).

[61] Press, W.H., Teukolosky, A.A., Vetterling, W.T., Flannery, B.F., "Numerical recipes in Fortran 77: The Art of scientific computing", second edition Cambridge University Press, Cambridge, (2001).

[62] Kaski, S., "Data exploration using self-organizing maps", Acta Polytechnica Scandinavica, Mathematics, Computing and Management in Engineering Series, 82, 57, (1997).

[63] Halkidi, M., Batistakis, Y. and Vazirgiannis, M., "On clustering validation techniques", Journal of Intelligent Information Systems, 17, 107-145, (2001).

[64] Kaufman, L. and Rousseeuw, P. J., "Finding groups in data: An introduction to cluster analysis", Wiley series in probability and mathematical statistics, John Wiley and Sons, New Jersey, (1989).

[65] Wilks, D. S., "Statistical methods in the atmospheric science", Academic press Limited, London, (1995).

[66] Mucha, H. J. and Sofyan, H., "Cluster Analysis", Springer, Heidelberg, (2000).

[67] MacQueen, J. B., "Some Methods for classification and Analysis of Multivariate Observations", Proceedings of 5-th Berkeley Symposium on Mathematical Statistics and Probability, Berkeley, University of California Press, (1967).

[68] Agencija Republike Slovenije - ARSO, "Mesečni bilten", Letnik XII, 6, (2005), Letnik XIII, 6, 7, 8, 9, (2006).

[69] Ackerman, J., "The extinction to back-scatter ratio of tropospheric aerosol: A numerical study", Journal of Atmospheric and Oceanic Technology, 15, 4, 1043-1050, (1997).